Doctoral theses at NTNU, 2021:324

Njål Kjærnes Tengesdal

Modelling and Simulation of Offshore Drilling Systems

Doctoral thesis

NTNU
Norwegian University of Science and Technology
Thesis for the Degree of Philosophiae Doctor
Faculty of Engineering
Department of Mechanical and Industrial Engineering

NTNU
Norwegian University of Science and Technology

Njål Kjærnes Tengesdal

Modelling and Simulation of Offshore Drilling Systems

Thesis for the Degree of Philosophiae Doctor

Trondheim, October 2021

Norwegian University of Science and Technology
Faculty of Engineering
Department of Mechanical and Industrial Engineering

NTNU
Norwegian University of
Science and Technology

NTNU
Norwegian University of Science and Technology

Thesis for the Degree of Philosophiae Doctor

Faculty of Engineering
Department of Mechanical and Industrial Engineering

ISBN 978-82-326-6900-4 (printed ver.)
ISBN 978-82-326-5593-9 (electronic ver.)
ISSN 1503-8181 (printed ver.)
ISSN 2703-8084 (online ver.)

Doctoral theses at NTNU, 2021:324

Printed by NTNU Grafisk senter

To Karoline and Åshild

Summary

This thesis presents the results of applying modelling theory, estimation, and control for the efficient formulation of drilling system models for real-time implementation and analysis. Together with modern sensor devices, efficient mathematical models for online estimation and closed-loop control during offshore drilling are becoming increasingly relevant. Therefore, the work in this thesis focuses on formulating models applicable to drilling performance optimization systems, where the models could act as virtual sensors to be used in a drilling control system. The thesis is organized as a collection of papers, including four journal papers, and a chapter containing theory for the purpose of exposition.

This thesis presents an unscented Kalman Filter combined with a nonlinear model predictive controller developed for predicting downhole fluid friction forces during tripping while keeping bottom-hole and upper well section pressures within their limits. The results of comparing three offset-error mitigation methods implemented in the controller are presented.

Two new lumped-parameter models of drill-string dynamics are proposed in this thesis. The first is derived by using Lagrangian mechanics and further structured into a component model with complete integral causality using the Bond Graph methodology. The assumed mode method is applied, reducing the dimension of the state-space while representing the distributed properties in terms of the number of modes included. The second proposed model is developed by using Kane's method, with its basis in the Newton-Euler formulation. The dynamics of the discrete model is a perturbation of a parametric curve in space representing the well path. Extensive simulation studies are performed to analyze the model transient response in a deviated well. A numerical solver convergence study for the Runge Kutta order 4 method and Generalized-α method is performed, and the real-time properties of the model have been investigated.

The thesis includes a stability analysis of a lumped-multi-element drill string model from previous work, described by axial and torsional dynamics. A nonlinear bit-rock model for predicting the dynamics of downhole drilling is included, and the stability margins of a decoupled axial system are presented for six common drill string configurations. Additionally, a simulation study is performed with a set of drill string configurations.

Preface

This thesis is submitted in partial fulfilment of the requirements for the degree of Philosophiae doctor (PhD) at the Department of Mechanical and Industrial Engineering (MTP) at the Norwegian University of Science and Technology (NTNU). The research presented in this thesis is the result of doctoral studies being funded by the Norwegian Research Council under SFI Offshore Mechatronics, grant number 237896. My supervisors have been Associate Professor Christian Holden (MTP, NTNU) and Professor Olav Egeland (MTP, NTNU).

Acknowledgements

In 2008, while starting out as an electrician apprentice, my only pursuit was to achieve the certification. I never considered it realistic to start, or even delivering a PhD.

I would like to thank Associate Professor Christian Holden for being my supervisor and admitting me as a PhD student. His guidance, feedback and support during these years have been instrumental for this work. I have appreciated his open-door policy, and his eagerness to share knowledge. I want to thank my co-supervisor Professor Olav Egeland for his support, and for granting me the opportunity to pursue a PhD in the SFI Offshore Mechatronics project. I would also like to thank Dr. Kristian Gjerstad for his guidance during 2017/2018 in defining possible research areas.

The research and written papers would not have been complete without the collaborators. I want to express my thanks to my co-authors, Professor Sigve Hovda, Associate Professor Bjørn Haugen, Gaute Fotland, Professor Eilif Pedersen, and Dr. Torstein Thode Kristoffersen. I have learned a great deal from all of them and enjoyed our collaboration. During my stay at MTP, I've also had the pleasure of being part of the Robotics and Automation group. I want to thank all members of the group for being great colleagues, for the good discussions, hiking, climbing, and skiing trips, and the shared friendship.

I want to thank my parents Eli and Morten, who have always supported me on my path in life. A big thanks to my brothers Stig and Trym for being there, and sharing mutual interests.

Finally, I want to express my warmest thanks to my wife Karoline. You have supported me throughout the good, and tough days, keeping me motivated for finishing this work. I am forever grateful for having you and our daughter, Åshild, by my side.

Contents

Chapter 1

Introduction

The offshore drilling industry has in recent years shifted towards automatic solutions on drilling rigs. The implication of this is larger attention to condition monitoring of system states and parameters, and prediction of the transient and steady-state behaviour of a system. Computationally efficient mathematical models comprising drilling system states and parameters are then considered vital in systems simulation to assist in safe decision-making and control for automated drilling.

The development of mathematical models and simulation procedures relevant for offshore operations is the core of Working Package (WP) 4 Modelling and Simulation in the SFI[1] Offshore Mechatronics (OM). The doctoral studies resulting in this thesis have been part of this project since fall 2017 under WP 4.2.

The purpose of SFI OM is to develop new concepts for the next generation of systems for autonomous operation and condition monitoring of topside drilling systems with land-based control, minimizing the need for manual intervention. The results will contribute to reducing the risk and cost related to the operation of offshore drilling systems, along with increasing operational efficiency in deeper waters and harsh weather. Joining together academic institutions, research institutes, along with industry partners, SFI OM contributes with both practical and theoretical research and development for the offshore industry.

1.1 Background

The offshore drilling industry is at the front line of establishing oil and gas production on the continental shelves, to meet the worldwide demand of energy. According to the forecast in [28], performed pre Covid-19 pandemic, a decline in the fossil fuel energy sources will occur after 2022 for oil and 2035 for natural gas. However, in the same report, fossil fuels have been predicted to be the dominant source of energy towards 2050, in addition to, e.g., wind, nuclear, and solar power generation.

[1] Senter for forskningsdrevet innovasjon (English: Centre for Research-based Innovation).

The uncertainty following the Covid-19 pandemic adds to the complexity for future activity of offshore operations. Measures such as the tax-reliefs for oil & gas exploration and development on the Norwegian Continental Shelf (NCS), given by the Norwegian government, have increased investment activity and startup of new projects [78]. With new offshore fields or new production wells on existing fields, offshore drilling will be required. Hence, it is important that continued drilling activities achieve increased operational efficiency to limit the impact on the environment. To reduce emissions, risk, and cost, together with increasing the performance related to drilling, digital solutions, such as the application of mathematical process models, and automation have been highlighted in [28]. These two topics are included as important tasks for research and development by Norway's technology strategy for the petroleum sector, OG21 [79].

Since the middle of the 20th century, mobile drilling rigs have been situated in open-ocean deep waters to explore potential oil and gas reserves and establish production wells. Facilities are then typically installed on fixed, large steel structures, or by floating production units often including a drilling unit to be able to extend the number of wells in the future. An overview of the systems connected to an offshore drilling rig and a production platform is provided in Figure 1.1.

Recent developments in offshore technology allow for tie-in of remote subsea production wells, or unmanned topside installations to the production facilities. These remote fields can be located in both arctic environments and at large depths, creating a challenging environment for

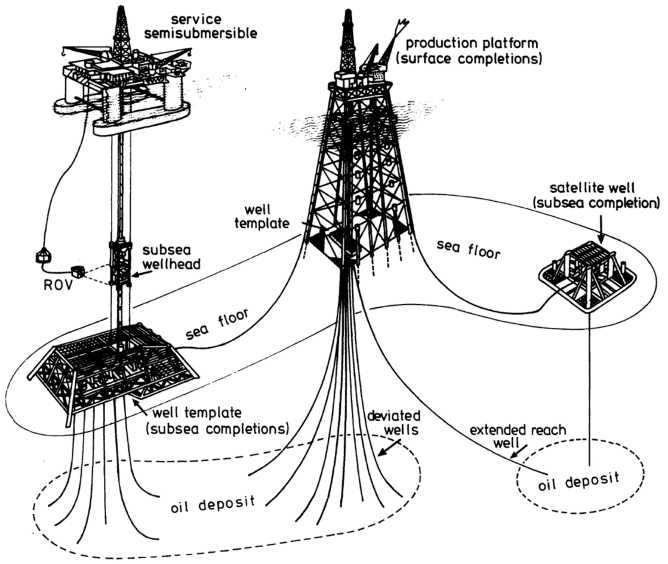

Figure 1.1: Drilling from stationary or floating facilities, and production from surface and subsea solutions, from [20]. A remotely operated underwater vehicle (ROV) is shown next to the subsea wellhead.

the operation of a drilling rig.

The drilling rigs can be categorised as *submersibles*, *jack-ups*, *semi-submersible* (as seen in Figure 1.1), or *drillships* where the latter two are floating units [22]. Rig configuration relates to the water depths it is supposed to operate in. The depths on the NCS reach about 1200 m, and overseas fields, such as the Gulf of Mexico or Brazil, drilling rigs are often required to be able to operate in depths of up to 3000 m [87]. Floating units are typically applied for drilling offshore wells in deep waters, with depths more than approximately 300 m [108]. This can involve challenges such as keeping the rig stationary in rough sea without the possibility of anchoring and heave motion compensation of a drilling riser fixed in position at the seabed [20].

1.1.1 Drilling systems

During field exploration and production preparation of a well, a drill string is used to excavate the rock formation on the path to the reservoir. The drill string is a complex structure ranging several kilometres long, comprising of steel pipes, stabilizers, tools for conditioning the borehole, instrumentation, and the drill bit for cutting rock. The drill bit is located at the end of the bottom-hole assembly (BHA), being the lowest section of the drill string. Figure 1.2a provides an overview of the components included in drilling a well.

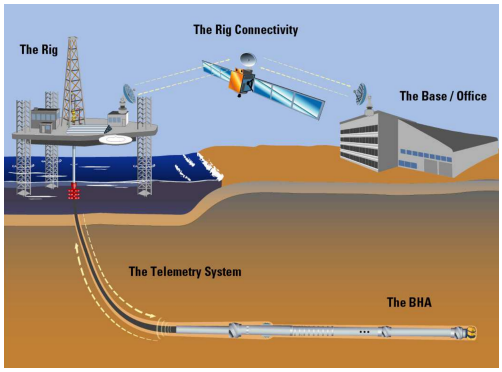

(a) Offshore drilling from a jack-up rig, and communication link to onshore facility [29].

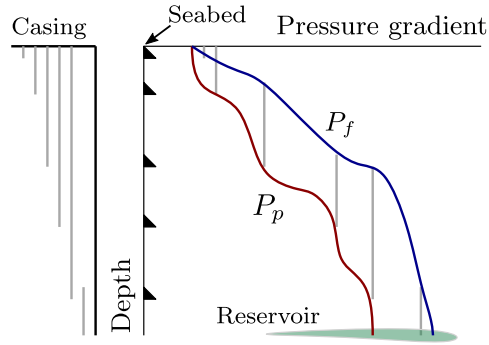

(b) Formation fracture P_f and pore P_p pressure margins, adapted with modifications [67, 97]. Note that it is common to replace the pressure gradient axis with equivalent mud weight, for estimating required fluid density to ensure stability.

Figure 1.2: Sketch of an offshore drilling rig and wellbore geopressure margins. Drilling a well, either offshore or onshore, requires installation of a casing (larger diameter pipes) being cemented into the drilled well to withstand the different pressure zones.

The drilling rig includes the machinery for rotating and hoisting the drill string in the well, as well as utility systems for conditioning of the well (fluid injection and retrieval) during drilling, and communication to shore. Measurements and actuating signals for monitoring and control

purposes of the drill string and formation are exchanged through the telemetry link to the BHA instrumentation [29, 86].

Towards the target reservoir, distinct pressure and temperature zones need to be analysed to plan and execute safe drilling procedures. During the first phases of drilling, a preliminary depth is reached before the drilling rig at the sea surface is connected with a seabed frame for installation of a blowout preventer (BOP) and riser. The BOP includes several safety valves for sealing off the well in case of dangerous well situations, and the riser acts as a guide for the drill string and return-path for the fluid called the drilling mud [20].

To drill a well within the margins of fracture (rock fracture resulting in fluid loss to formation), collapse (formation collapses into the well), and pore pressure (leakage of fluid trapped inside the formation into the wellbore) (Figure 1.2b), installed casings at specific depths and weighted mud are used while drilling further into the formation. The rig mud pump unit ensures the circulation of the mud from top-side through the drill string, and down to the drill bit. The mud is then forced to return through the annular section of the well back to the rig. During the return, rock cuttings are transported with the mud being filtered out topside before the mud is reused. If sudden uncontrolled pressure outbreaks in well occur, such that the drilling mud cannot counter-act the wellbore pressure, the BOP seals off the borehole and isolates the well from the surface installation.

Drilling operations related to pulling out or running a drill string into the well (tripping) and connecting stands while keeping the drill string fixed to the rig floor are subject to induced surge and swab pressures [42]. The drill string up- and downwards motion due to hoisting, and un-compensated rig motion creates a piston effect in the well. Ultimately instabilities due to pressure transients may jeopardize well integrity while drilling.

1.2 Motivation

Challenges faced while drilling for oil & gas offshore are such as accurate wellbore pressure control, minimizing drill string failure due to vibrations, compensation of heave due to waves, reducing friction and drag, and optimal transport of cuttings for hole-cleaning. Using automatic control to overcome these challenges relies on fast and accurate sensor measurements available topside and down-hole, together with a properly designed drilling control system.

Tools integrated into the drill string BHA for supplying measurements of down-hole conditions are called measurement-while-drilling (MWD), and logging-while-drilling (LWD) instruments. Rotational speed, position readings, force and torque measurements at the drill bit, and fluid and formation data are then measured by a sensor device, transmitting signals by the telemetry link. Traditionally, the telemetry link has been the fluid in the well (i.e., the mud), hence, signal pulses travel with the mud flow in the well up to a receiver at the rig surface [5]. Comparatively, wired drill pipes (WDP) capable of a higher signal transmission rate are now more commonly applied while drilling [36, 77]. An advantage of applying the WDP is bi-

directional information exchange between surface and downhole, for simultaneous transmission of measurements and commands [77].

Recent sensor developments together with the introduction of WDP have ensured real-time capabilities in the interchange of information and commands with the rig control system and the drill string devices [82]. These factors, together with machinery suitable for computer-based control, are further taken advantage of in the implementation of automated control and assisted monitoring on drilling rigs [54]. Recent progress has resulted in advanced field-tested systems for decision support and drilling performance optimization [35, 55]. Evidently, the implementation of such systems reduces cost related to downtime and increases safety in operations, being some of the main reasons for implementing automated process control [99].

Closely coupled with the sensors and high-speed data transfer available in drilling systems are mathematical models formulated for real-time simulation of closed-loop control and estimation. For a dynamic drilling model intended for estimation and control purposes, it is argued in [57] that the complexity should be kept low and parameters difficult to distinguish from measurements should be lumped together. Moreover, parameters in a model intended for real-time purposes can be calibrated online to sensor measurements, while drilling is ongoing [54]. This is mentioned to increase robustness of the model towards multiple scenarios [57]. Implementation aspects regarding the mathematical formulation and numerical solver robustness and efficiency are important. Furthermore, accurate definitions of model inputs and outputs used for actuator and sensor systems are required [35].

1.2.1 Automatic control

Automatic control of travelling block velocity, mud pumps, and the mud-return choke valve are measures being implemented to ensure reduced pressure transients during tripping. These control requirements are similar to managed pressure drilling (MPD), where the mud pumps and mud-return valve is applied to control the back-pressure of the wellbore annulus (see e.g., [30, 43]).

Multi-variable control design applies to automatic tripping due to critical constraints on pressure margins, actuator limits, and decision making on behalf of available measurements, sensor estimates, and required sequences. In Cayeux et al. [16], a system assisting the driller with manipulation of tripping speed and top drive rotation including safeguards was tested on an offshore drilling rig with positive results. Hydraulic models (see e.g., the work in Gjerstad et al. [41], Kaasa et al. [57]) to estimate downhole conditions, coupled with the mechanical model of top side rig and drill string dynamics, can be combined with model-predictive-control (MPC).

The MPC is a widely applied advanced process control method for both linear and nonlinear applications, using *receeding horizon control* where the measured output at a specific time instant, together with current and future constraints, are taken into account [34, 45]. Being an industry-standard in process control, where process constraints are important [83], the MPC has received large attention in the field of offshore MPD [11]. An automatic system applying this control law method, coupled with state estimation, has been proposed to use in tripping opera-

tions in this thesis. State estimates of unmeasured states are given by a nonlinear variant of the classical Kalman filter [58].

1.2.2 Modelling of drill string dynamics

Keeping the wellbore intact and ensuring stability is closely coupled to the motion of the drill string while longitudinal motion and rotation are ongoing. Being several kilometres long, large length-to-diameter ratios of the drill string are common, making it resemble a thin guitar string. The geometric complexity of the drill-string increases with the added stabilizers, reamers, and equipment down-hole. A challenge regarding increasing drill string length is decreased structural stiffness. The implication of this is complex vibration patterns, influencing the ability to achieve steady drilling velocities. Axial, lateral, and torsional vibrations are present.

In literature, a large range of models for drill string dynamics exists, depending on the application and desired accuracy towards realistic behavior. The type of drill string models can be divided into *distributed models*, *Finite Element Method (FEM) models*, and *lumped-parameter models*.

Distributed drill string models (see e.g., Aarrestad et al. [2], Aarsnes and Shor [3], Goicoechea et al. [44], Wang and Tucker [107]) can be described by partial differential equations (PDE) depending on spatial coordinates and time along the drill string length. PDE models are often complex, and according to [93] accuracy relies on the chosen boundary conditions. For linear PDEs, analytical solutions can be obtained; however, this is not always the case for nonlinear PDEs. Therefore, a numerical approximation can be obtained through, e.g., the FEM framework (FEM drill string models have been proposed in, e.g., Feng et al. [33], Germay et al. [38], Khulief and Al-Naser [63], Vromen et al. [106]). These types of models serve the purpose of accurate vibration analysis, but can become complex and create a larger state-space, which can be computationally heavy with increased simulation time. However, with the increased capabilities of the modern computer, FEM models applied to describe drill string dynamics become more relevant, also discussed in the implementation in Butlin and Langley [14].

For real-time applications, control design, and parameter identification, the dynamics of drill strings are often modelled based on the lumped-parameter method. The models developed on the basis of this method comprise a system described by ordinary differential equations (ODE), typically in a second-order form (see for example Besselink et al. [10], Cayeux [15], Hovda [51, 52], Zhao and Sangesland [109], where the two latter are rewritten on a semi-analytical form). The distributed properties are represented by finite lumps, where the elasticity and inertia characteristics depend on the number of chosen model elements. Furthermore, as the model state variables depend on time only, signal input and output mapping is simplified.

Well-defined signal flow in simulation models is important in terms of identifying how a subsystem interacts with its connected systems. In terms of drilling system simulators, this motivated the work of constructing a component formulation of a drill string in this thesis work. The Bond Graph (BG) methodology (see, e.g., Karnopp et al. [61], and a lumped mass BG formulation of a drill string in Sarker et al. [94]), has been shown to be efficient in establishing

component models. The BG method considers the exchange of power between the model components by transmitting an effort e signal and a flow f signal. The product ef then constitutes the transferred power. Systematic definition of *causality* is applied to describe the computational inputs and outputs of a model. Causality defines whether the state equations are formulated for integration or differentiation. Hence, for numerical simulation, a model with integral causality is preferred; however, assumptions applied in formulating the model can yield algebraic state dependencies giving differential causality [61]. It is worthwhile to mention the *acausal* modeling method, which in turn is unspecific regarding the input and outputs of a component model. Moreover, the component is specified by a system of equations instead of causal input and output assignments, and the context where the model is applied defines what are the necessary input-outputs [37]. The causality is then fixed when the corresponding equation system is solved. The *Modelica* language is utilizing this approach, and in Dadfar et al. [21], a Modelica library was proposed for use in wellbore construction with applications such as estimating friction during drilling. Hence, component models serve as building blocks in these libraries.

In recent years, simplified models to analyse the drill string dynamics in directional wells have been proposed, such as the work by Hovda [52], Zhao et al. [110]. These models are similar to the field of drill string torque- and drag analysis, where the focus is on optimizing top-side torque and hook loads to achieve minimal friction-induced forces and torques in directional wells. Separation of the models are mainly denoted soft- or stiff-string models in terms of taking into account the borehole stiffness and the point-wise contact with the wellbore [95]. It has been argued that soft-string models (see, e.g., Aadnøy et al. [1] in terms of an analytical approach) are computationally favourable, as existing stiff-string models are often requiring the use of FE analysis. However, work has been made to bridge the gap between accuracy and computational effort [15].

1.2.3 Analysing stability in drilling systems

The drill string models and their coupling to the environment form the basis of designing control laws to maintain optimal drilling velocities and avoiding excessive vibrations. As such, system stability is typically related to the drill string coupling with friction and contact behaviour arising from drilling a well. Special attention has been directed towards investigating drilling stability relating to axial vibrations when applying a type of drill bit denoted PDC or drag bits. These are equipped with fixed blades (as opposed to roller-cone bits with three rotating cones), and analysis has shown that this bit is prone to self-excited axial vibrations. According to [23], this phenomenon stems from the regenerative cutting process between the bit and formation. Moreover, an unstable equilibrium point of the system can trigger self-excited vibrations. This may eventually result in axial bit bouncing and torsional stick-slip cycles, due to coupled axial and torsional dynamics [39].

For vertical wellbores, under the assumption of limiting the drill string model to a two-degree-of-freedom system in axial and torsional motion, the part describing the process of cutting rock is commonly denoted the *bit-rock* interaction [9, 26]. Hence, the friction phenomena

in these models are often limited to the bit. For wellbores described by changes in inclination for the path towards the reservoir, friction cannot be neglected above the bit due to, e.g., contact with the borehole in bends [71].

A recent shift in dealing with the discontinuous effects of drilling came with the work in Richard et al. [88]. This work proposed a model coupling axial and torsional dynamics through a state-dependent delay for the force and torques of rock-cutting and contact due to friction, based on the work in [27]. An interesting work on characterizing the stability for a lumped single element system was also done in Besselink et al. [9, 10], where effort is made to analyse the decoupled influence of axial motion on the torsional dynamics, for the bit-rock model in [88]. Stability maps originating from a linear time-invariant time-delay equation were drawn for changing system parameters. Moreover, axial stick-slip limit cycles were described thoroughly in the paper. Coupled axial and torsional system stability was addressed in Nandakumar and Wiercigroch [73], which also performed an analysis on a lumped single element models.

Distributed stability analysis in form of analysing the stability of models described by PDEs has been performed previously, such as in the work by Aarsnes and van de Wouw [4]. The model in [4] yields a distributed parameter model where the coupled axial and torsional stability was analysed. In their work, it is argued that the low-order models (two-degree- of-freedom with one lumped element) are inadequate to analyse stability properties. Hence, motivated by the applicability of higher-order lumped models for real-time implementation, findings from the decoupled axial and torsional stability conditions for lumped-multi-element models are presented in this thesis.

1.3 List of publications

This thesis is structured as a collection of the published and submitted papers produced during the doctoral studies. The thesis is based on four peer-reviewed journal papers, where two are published, and two are submitted and under review in international journals. The publications are listed below:

Paper I [100] N. Tengesdal and C. Holden. Identification and optimal control for surge and swab pressure reduction while performing offshore drilling operations. *Modeling, Identification and Control*, 41(3):165–184, 2020

Paper II [104] N. K. Tengesdal, C. Holden, and E. Pedersen. Component-based modeling and simulation of nonlinear drill-string dynamics (submitted). *Journal of Offshore Mechanics and Arctic Engineering*, 2021

Paper III [103] N. K. Tengesdal, G. Fotland, C. Holden, and B. Haugen. Modeling of drill string dynamics in deviated wells for real-time simulation (submitted). *SIMULATION: Transactions of the Society for Modeling and Simulation International*, 2021.

Paper IV [105] N. K. Tengesdal, S. Hovda, and C. Holden. A discussion on the decoupling assumption of axial and torsional dynamics in bit-rock models. *Journal of Petroleum Science and Engineering*, 202, 2021.

The author has additionally written two peer-reviewed research papers which are not part of this thesis:

[101] N. Tengesdal, T. T. Kristoffersen, and C. Holden. Applied nonlinear compressor control with gain scheduling and state estimation. *IFAC-PapersOnLine*, 51:151–157, 2018

[102] N. Tengesdal, C. Holden, and E. Pedersen. Component-based modeling and simulation of nonlinear drill-string dynamics. In *ASME 2019 38th International Conference on Ocean, Offshore and Arctic Engineering*. American Society of Mechanical Engineers Digital Collection, 2019

The papers are included in Chapter I–IV.

1.4 Contributions

A summary of the contributions from the work in this thesis is given below. The reader is referred to Chapter 3 for more details regarding each contribution.

Paper I An automatic drill string tripping system based on an unscented Kalman filter and nonlinear-model predictive controller for reducing surge and swab pressures.

Paper II A dynamic drill string model formulated in component-form by Bond Graphs for large-scale system simulation studies.

Paper III A lumped-parameter drill string model for analysing coupled transient behaviour in arbitrary three-dimensional directional wells.

Paper IV A discussion on dynamic model coupling of axial stability and lumped-parameter elements for on-bottom analysis, including a lumped multi-element parameter model for on-bottom drilling analysis.

1.5 Thesis structure

The rest of the thesis is organized as follows. Chapter 2 includes relevant background theory for the material presented in the papers included in this thesis. The contributions from each work are summarised in Chapter 3, before the concluding remarks and proposed future work are presented in Chapter 4. In the second part of the thesis, Chapters I–IV includes the pre-print or published versions of the scientific papers written during the doctoral studies.

Chapter 2

Theory

"Everything should be made as simple as possible, but no simpler."

— Albert Einstein

This chapter includes theory relevant to the work presented in this thesis. Section 2.1 establishes some common notations. In Section 2.2, a classification of the distributed parameter models of vibrations is given. Motivated by the definitions made in this section, a lumped-element approximation of the distributed models is presented in Section 2.2.6. Section 2.3 includes fundamental friction models being important in implementation and analysis of drilling simulation systems. A brief discussion of stability for linear time-delay systems is given in Section 2.4. Finally, in Section 2.5 introductory numerical methods relevant to perform simulation studies with the developed models and systems are given.

2.1 Preliminaries

Simulation can be described as the practice of experimenting on a model. In this thesis work, the aspect of performing experiments on *mathematical* models is considered. Furthermore, the response or behaviour at specific operating conditions, and system stability are then investigated using numerical or analytical techniques, or a combination of the two.

System models for analysis and simulation can be represented as ODEs, which in the deterministic case are expressed as

$$\dot{\boldsymbol{x}}(t) = \boldsymbol{f}(\boldsymbol{x}(t), \boldsymbol{u}(t), t) \tag{2.1}$$

where $\boldsymbol{f}$ is the nonlinear *time-varying* model of an nonautonomous system [62], $\dot{\boldsymbol{x}} \in \mathbb{R}^{n_x \times 1}$ is the differential states of the system in vector form, $\boldsymbol{x} \in \mathbb{R}^{n_x \times 1}$ is the state vector, and $\boldsymbol{u} \in \mathbb{R}^{n_u \times 1}$ is the system input(s). A special case of (2.1) is the linear *time-invariant* system, expressed as

$$\dot{\boldsymbol{x}}(t) = \mathbf{A}\boldsymbol{x}(t) + \mathbf{B}\boldsymbol{u}(t) \tag{2.2}$$

where $\mathbf{A} \in \mathbb{R}^{n_x \times n_x}$ is the linear system matrix (the Jacobian of the system states), and $\mathbf{B} \in \mathbb{R}^{n_x \times n_u}$ is the input matrix (Jacobian of the inputs).

Stability analysis is in its most common form an investigating of the system *equilibrium point*, defined as the state of which the system do not change in time. For the time-invariant, unforced system in (2.1), i.e., $\boldsymbol{f}(\boldsymbol{x}, \boldsymbol{u}, t) = \boldsymbol{f}(\boldsymbol{x})$, the equilibrium point $\boldsymbol{x} = \boldsymbol{x}^\star$ is obtained by

$$\boldsymbol{f}(\boldsymbol{x}^\star) = \boldsymbol{0} \tag{2.3}$$

where the equilibrium point is then a solution for all t. Without loss of generality in assuming that the stability of every equilibrium point is studied at the origin, hence, $\boldsymbol{f}(\boldsymbol{x})$ satisfies $\boldsymbol{f}(\boldsymbol{0}) = \boldsymbol{0}$ and the stability of $\boldsymbol{x} = \boldsymbol{0}$ is investigated. For non-zero equilibrium points, a change of variables can be performed to shift the equilibrium to the origin. A definition of stability for $\boldsymbol{x} = \boldsymbol{0}$ is given as

Definition 2.1 (Khalil [62, Def. 4.1])**.** The equilibrium of $\boldsymbol{x} = \boldsymbol{0}$ of $\dot{\boldsymbol{x}} = \boldsymbol{f}(\boldsymbol{x})$ is

- Stable if, for each $\epsilon > 0$, there is $\delta = \delta(\epsilon) > 0$ such that

$$||\boldsymbol{x}(\boldsymbol{0})|| < \delta \implies ||\boldsymbol{x}(t)|| < \epsilon, \forall t \leq 0$$

- Unstable if it is not stable
- Asymptotically stable if it is stable and δ can be chosen such that

$$||\boldsymbol{x}(\boldsymbol{0})|| < \delta \implies \lim_{t\to\infty} \boldsymbol{x}(t) = \boldsymbol{0}$$

An asymptotically stable system then returns to $\boldsymbol{x}^\star$ if subject to small disturbances, and is bound to stay there for all future time [62]. For the linear system in (2.2), asymptotic stability is ensured if all eigenvalues λ_i of $\mathbf{A}$ has negative real part, i.e., $\text{Re}\lambda_i < 0$.

2.2 Vibrations in mechanical systems

Long, slender mechanical structures found in offshore drilling operations involve systems such as oil & gas drill strings, and long-reach crane arms for lightweight payloads. A common characteristic for these systems is a large length-to-diameter ratio and high elasticity, which can make these systems prone to large oscillations under abnormal operating conditions.

The continuum properties of large length-to-diameter structures can be described by a distributed parameter description, given by PDEs dependent on a spatial coordinate and time. Classical texts on mechanical vibrations are Meirovitch [69] and Rao [84]. These references give an excellent description of the topic, and we will in the following section include material relevant to the research done in this thesis work. A general form of the lumped-parameter model given in Section 2.2.6 will then be expressed from the spatially distributed finite lumps introduced in this section.

The purpose of this section is then to address the axial, transverse, and torsional vibration modes in distributed form as scalar PDEs, in their decoupled state defined in space by a position along the structure and time. Each vibration mode is treated separately and is then assumed to be decoupled when considering only the perturbation in elastic displacements.

2.2.1 Distributed descriptions

A long elastic structure with length L is described relative to a fixed based frame with unit vectors $\vec{e}_i$, $i = 1, 2, 3$, seen in Figure 2.1. The continuous variable z denotes the position along the longitudinal length of the elastic structure, with $z = L$ being the end of the structure. Moreover, the structure can be used to describe a drill string including a BHA, where the latter is illustrated as the section with a larger cross-section.

The motion of an infinitesimal segment of the drill string can be given by the spatial coordinates $\chi(z,t)$, $\zeta(z,t)$, and $\xi(z,t)$ along $\vec{e}_1$, $\vec{e}_2$, and $\vec{e}_3$, respectively, given position z and time t. Hence, the spatial variables $\chi(z,t)$, $\zeta(z,t)$, and $\xi(z,t)$ are then describing the motion in transverse normal, transverse bi-normal, and longitudinal direction, respectively, and the coordinate $\varphi(z,t)$ describes the segment twist. Note that the coordinate frame has a positive $\vec{e}_3$ pointing down along the straight vertical.

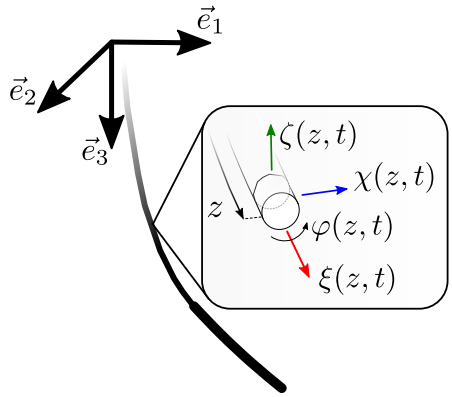

Figure 2.1: Spatial description of an infinitesimal drill string element.

To establish the dynamics of axial, transverse, and torsional motion of the drill string, the longitudinal axis is assumed to point along the length of the drill string. Following the notation of [61, Ch. 10], the force equilibrium of the spatially distributed finite lump of the drill string with length Δz will be presented. Furthermore, as this lump becomes infinitesimal in size, the distributed equations of motion are given.

Considering that the fixed base frame is an inertial frame of reference, the distributed axial and lateral equations of motion can be derived by the use of Newton's second law in terms of force equilibrium. As stated previously, the decoupled vibration states are presented such that the motion is assumed to take place in one plane [84]. A summation of all external forces and the element inertia force yields the force equilibrium given as

$$\sum_{i=1}^{k} \vec{F}_i = m\vec{a} \tag{2.4}$$

where $\vec{F}_i$ is ith external force acting on the system, m is the element mass, $\vec{a}$ is the linear acceleration and $-m\vec{a}$ denotes the inertia force[1]. As such, when the system undergoes positive acceleration (velocity increases), the inertia force acts in the opposite direction. We will further on assume that the drill string has a uniform cross-sectional area, simplifying the derivations [61].

2.2.2 Axial vibrations

The axial forces acting on the finite element of mass seen in Figure 2.2 is expressed from the normal stresses $\sigma(z)$ across the element, in the direction of $\vec{e}_3$. Additionally, we assume that gravitational forces and external forces are present.

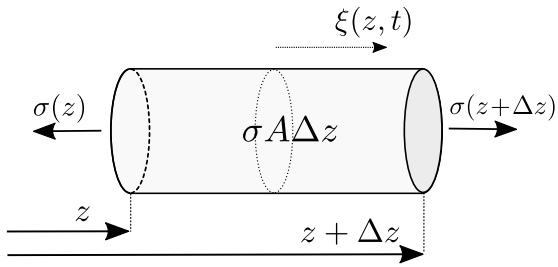

Figure 2.2: Axial finite element [61].

From (2.4), the equation of motion for the longitudinal spatial coordinate $\xi(z,t)$ can be expressed as

$$m\Delta z\frac{\partial^2\xi}{\partial t^2} = A\sigma(z+\Delta z) - A\sigma(z) + f(z,t)\Delta z + mg\Delta z \tag{2.5}$$

where $f(z,t)$ is an external force per unit length acting on the element, $m = \rho A$ is the mass per unit length, g is the acceleration of gravity, A is the cross-sectional area of the element. Note that the normal stress is related to the strain as $\sigma(z) = E\epsilon(z)$, where E is the Young's modulus characterizing the elasticity of the material and ϵ is the strain over the element. The strain is defined as the ratio of the deformation to the undeformed length of the element [108].

Suppose that we divide by Δz in (2.5) to obtain

$$m\frac{\partial^2\xi}{\partial t^2} = EA\frac{\epsilon(z+\Delta z) - \epsilon(z)}{\Delta z} + f + mg \tag{2.6}$$

where we have inserted for $\sigma = E\epsilon$. The distributed representation can be given by letting $\Delta z \to 0$ in (2.5). Furthermore, the infinitesimal strain is given as

$$\frac{\epsilon(z+\mathrm{d}z) - \epsilon(z)}{\mathrm{d}z} = \frac{\partial\xi(z,t)}{\partial z} \tag{2.7}$$

[1]Hence, $m\vec{a} = m\mathrm{d}\vec{v}/\mathrm{d}t$ is the rate-of-change of linear momentum of the system.

and the PDE of the longitudinal equation of motion for a uniform drill string can then be written as

$$m\frac{\partial^2\xi}{\partial t^2} = EA\frac{\partial^2\xi}{\partial z^2} + f + mg \tag{2.8}$$

being subject to external forces. The common one-dimensional wave equation is obtained by $f = 0$ and neglecting the gravitational forces.

2.2.3 Lateral vibrations

Consider the transverse motion of the spatially distributed finite element Δz in Figure 2.3, in the $\vec{e}_1$-$\vec{e}_3$ plane.

A neutral axis is defined as the axis along the centroid of the pipe. The arrow notation follows the convention of clockwise rotation defined by a positive shear force, generating a positive bending moment at the left boundary, about a local axis in the direction of $\vec{e}_2$. The shear force equilibrium of the finite element of mass undergoing transverse motion is given as

$$\rho A\Delta z\frac{\partial^2\chi}{\partial t^2} = V(z) - V(z+\Delta z) + f(z,t)\Delta z \tag{2.9}$$

where $V(z)$ is the shear force, $f(z,t)$ is a external transverse force per unit length acting perpendicular to the neutral axis of the element, and $\chi(z,t)$ is the spatial lateral coordinate defined along the element $\vec{e}_1$ direction.

From Figure 2.3, the moment balance about an axis passing through a, in the direction of $\vec{e}_2$, considering the rotational inertia of the element can be expressed according to [61] as

$$\Delta z I^c_{yy}\frac{\partial^2\phi}{\partial t^2} = M(z+\Delta z) - M(z) - V(z+\Delta z)\Delta z \tag{2.10}$$

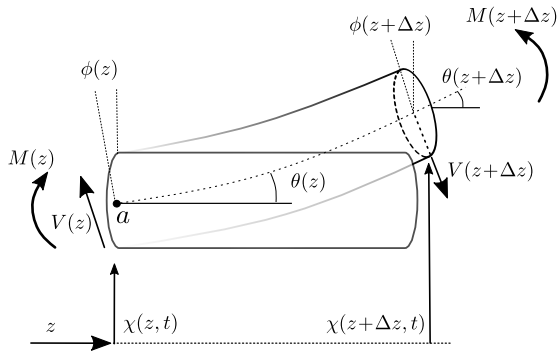

Figure 2.3: Transverse element in bending and shear [61].

where $M(z)$ is the moment, I^c_{yy} is the moment of inertia per unit length about the element principal axis y, in the direction of $\vec{e}_2$, with superscript denoting the centre of mass, and $\phi(z,t)$ is the angle between the cross-section and a vertical reference axis (along $\vec{e}_1$).

The angle between the neutral axis along the element and the horizontal reference axis $\vec{e}_3$ can be defined as

$$\theta(z) = \frac{\chi(z+\Delta z) - \chi(z)}{\Delta z} \tag{2.11}$$

such that the shear angle can be given according to [61]

$$\gamma = \theta - \phi. \tag{2.12}$$

The shear force at the location z along the element can then be expressed as

$$V = k_s G A \gamma \tag{2.13}$$

where k_s is the shearing coefficient, and G is the shear modulus of the element.

If we divide by Δz in (2.9) and (2.10), we get

$$\rho A \frac{\partial^2 \chi}{\partial t^2} = f(z,t) - \frac{V(z+\Delta z) - V(z)}{\Delta z} \tag{2.14}$$

$$I^c_{yy} \frac{\partial^2 \phi}{\partial t^2} = \frac{M(z+\Delta z) - M(z)}{\Delta z} - V(z+\Delta z) \tag{2.15}$$

and the distributed representation is obtained by taking the limit as $\Delta z \to 0$, yielding

$$\rho A \frac{\partial^2 \chi}{\partial t^2} = f(z,t) - \frac{\partial}{\partial z}(k_s G A \gamma) \tag{2.16}$$

$$I^c_{yy} \frac{\partial^2 \phi}{\partial t^2} = \frac{\partial M(z,t)}{\partial z} - k_s G A \gamma \tag{2.17}$$

where we have inserted for (2.13). Hence, (2.16) and (2.17) constitutes two PDEs with two unknowns in $\chi(z,t)$ and $\phi(z,t)$.

Using Euler-Bernoulli beam theory, the rotational inertia of the element is neglected by considering that the plane cross-sectional area do not change (infinite shear stiffness [61]). Hence, $\theta = \phi = \partial\chi/\partial z$ from (2.11). Furthermore, by assuming pure bending conditions, the moment can be given

$$M(z,t) = E I_y \frac{\partial \phi}{\partial z} = E I_y \frac{\partial^2 \chi}{\partial z^2} \tag{2.18}$$

where I_y is the second moment of area, the shear angles of the infinitesimal element is $\phi = \theta = \partial\zeta/\partial z$. Note that $I_y = I_x$ by assuming a symmetric cross-section. Using this assumption, and substituting (2.18) into (2.17), we get

$$E I_y \frac{\partial^3 \chi}{\partial z^3} = k_s G A \gamma \tag{2.19}$$

which in turn is inserted into (2.16) from which we obtain

$$EI_y \frac{\partial^4 \chi}{\partial z^4} + \rho A \frac{\partial^2 \chi}{\partial t^2} = f(z,t) \tag{2.20}$$

constituting the PDE of forced lateral vibration of a uniform drill string section.

2.2.4 Torsional vibrations

The Newton's second law of linear momentum can be further used to derive the dynamic equilibrium of angular momentum, by studying the rotational motion separately from the element translational motion. This will be done next.

The torque is defined as rate-of-change of angular momentum generated around the element centroid axis. Furthermore, considering the planar motion of an element, Newton's second law of motion for the net torque can be expressed as [84]

$$\sum_{i=1}^{k} T_i = I_{zz}^c \ddot{\varphi} \tag{2.21}$$

where T_i is the ith torque acting on the centroid axis of the system, I_{zz}^c is the moment of inertia of the element about its centroid axis, and $\ddot{\varphi}$ is the angular acceleration.

For the finite element Δz subject to torsion in Fig. 2.4, the net torque balance about the centroid axis can be given as

$$I_{zz}^c \Delta z \frac{\partial^2 \varphi}{\partial t^2} = T(z+\Delta z) - T(z) + T_a(z,t)\Delta z \tag{2.22}$$

where T_a is the external applied torque on the element, and $\varphi(z,t)$ is the angular displacement along the length of the element.

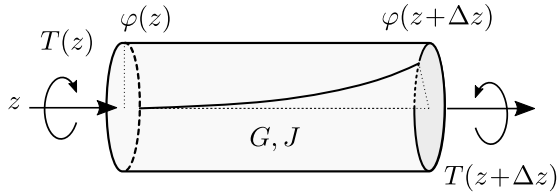

Figure 2.4: Spatially distributed finite element subject to torsion.

Dividing by Δz followed by letting $\Delta z \to 0$ in (2.22), we get

$$I_{zz}^c \frac{\partial^2 \varphi}{\partial t^2} = \frac{\partial T(z,t)}{\partial z} + T_a. \tag{2.23}$$

The uniform element is subject to torsional shear stress relating the angular displacement to the torque along the infinitesimal distributed element. The angular displacement, or twist, is then given as [108]

$$\frac{\partial \varphi(z,t)}{\partial z} = \frac{T(z,t)}{GJ} \tag{2.24}$$

where $J = I_z = I_x + I_y$ is the torsional constant being equal to the polar moment of area since symmetry for the cross-section was assumed. Furthermore, we can rewrite (2.23) yielding equation of motion

$$I_{zz}^{c} \frac{\partial^2 \varphi(z,t)}{\partial t^2} = \frac{\partial^2 \varphi(z,t)}{\partial z^2} GJ + T_a \tag{2.25}$$

which can be described as the PDE of a torsional wave, subject to an external torque.

2.2.5 Boundary conditions

As mentioned in the preliminaries of this section, the distributed equations of motion for axial, transverse and torsional domain are defined by the chosen boundary conditions. These will then depend on the modelling assumptions made, based on the physical interpretation of the system under study. Moreover, to analyse the response of (2.8), (2.20), and (2.25), specific boundary conditions must be applied to solve the equations of motion for $t \in [0, \infty)$.

2.2.6 Lumped element descriptions

The spatially distributed finite element descriptions for the axial, lateral and torsional dynamics in Section 2.2.2, 2.2.3 and 2.2.4 form the basis for the derivations in this section. The same assumption of an uniform drill string element with symmetric cross-section is made in this section, hence, we can simplify the mathematical modelling of the lumped model. Furthermore, the forces and torques are assumed to act on the mass centre of the element Δz.

2.2.6.1 Lumped axial and torsional systems

We will in this section derive a lumped element approximation of (2.8) and (2.25). Consider the equilibrium equation in (2.5). We define the time-dependent acceleration of mass element i as $\ddot{q}_i(t) = \partial^2 \xi / \partial t^2$. Furthermore, the finite element is assumed to be subjected to uniform load distribution as shown in Figure 2.5a. This is further used to define the uniaxial strain.

The strain due to compression or elongation can be given according to [61] as

$$\epsilon(z) = \frac{\xi(z) - \xi(z - \Delta z)}{\Delta z} \tag{2.26}$$

and the force from normal stress can be given as

$$F = A\sigma = EA\epsilon \tag{2.27}$$

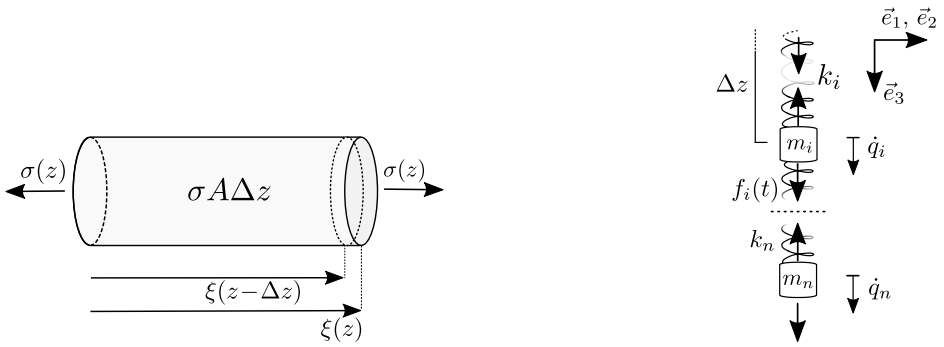

(a) Uniaxial loading.

(b) Lumped model representation.

Figure 2.5: Axial finite element and lumped-parameter model.

which reflects the ability of the structure to restore its original state. The relative displacement between the ith and $i-1$ element can be given by $q_i - q_{i-1}$, where $q_i = \xi_i$. This can be used to obtain the force acting on the mass point i from $i-1$ as

$$F_i = \frac{EA_i}{\Delta z}(q_i - q_{i-1}) \tag{2.28}$$

where Δz is the distance between each lumped mass. By defining the lumped coefficient of stiffness $k_i = EA_i/\Delta z$, we use (2.28) to rewrite (2.5) as

$$m_i\ddot{q}_i + k_i(q_i - q_{i-1}) - k_{i+1}(q_{i+1} - q_i) = f_i + m_i g \tag{2.29}$$

where $m_i = \rho A_i h$, and f_i is an externally applied force on the lumped element.

A lumped-parameter axial model with multiple elements from (2.29) is illustrated in Figure 2.5b, where mass-less springs attached between the elements represent the distributed elasticity. The stiffness of the spring then characterises its ability to compress or extend, which relates to the restoring properties the structure. If $f_i = 0$, (2.29) comprises of a linear second-order ordinary differential equation of a harmonic oscillator with attached massless springs to the mass points.

Similarly for (2.22), we can define the angular acceleration as $\ddot{\theta} = \partial^2\varphi(z,t)/\partial t^2$, and the torsional stiffness from the applied torque over dz as

$$T(z) = GJ\frac{\varphi(z) - \varphi(z - \Delta z)}{\Delta z} \tag{2.30}$$

which is used to define the torque acting on i from i–1, given by the relative angular displacement as

$$T_i = \frac{GJ_i}{\Delta z}(\theta_i - \theta_{i-1}). \tag{2.31}$$

From this, we obtain the same second-order ODE in terms of the angular displacement, or twist, given as

$$I_i^c\ddot{\theta} + \kappa_i(\theta_i - \theta_{i-1}) - \kappa_{i+1}(\theta_{i+1} - \theta_i) = T_{a,i} \tag{2.32}$$

where $I_i^c = \rho J_i \Delta z$ (note that the subscript for I_{zz}^c is dropped), and $\kappa_i = GJ_i/\Delta z$. A lumped multi-element torsional pendulum model divided into n elements can be written from (2.32), in coordinate form as

$$\boldsymbol{\mathcal{I}}\ddot{\boldsymbol{\theta}}(t) + \boldsymbol{\mathcal{K}}\boldsymbol{\theta}(t) = \boldsymbol{t}(t) \tag{2.33}$$

where $\boldsymbol{\mathcal{I}} \in \mathbb{R}^{n\times n} = \text{diag}([I_1^c, \ldots, I_n^c])$ is the moment of inertia matrix, $\boldsymbol{\mathcal{K}} \in \mathbb{R}^{n\times n}$ is the torsional stiffness matrix, $\boldsymbol{\theta} \in \mathbb{R}^{n\times 1}$ is the angular displacements for each element, $\boldsymbol{t} \in \mathbb{R}^{n\times 1}$ is the vector of input and external torques. Note that velocity proportional viscous damping can be included by adding $\mathbf{D}\dot{\boldsymbol{\theta}}(t)$ to the left-hand side of (2.33). The torsional stiffness matrix is defined as a tri-diagonal matrix given by

$$\boldsymbol{\mathcal{K}} = \begin{bmatrix} (\kappa_1 + \kappa_2) & -\kappa_2 & 0 & \ldots & 0 & 0 \\ -\kappa_2 & (\kappa_2 + \kappa_3) & -\kappa_3 & \ldots & 0 & 0 \\ \vdots & \vdots & \ddots & & \vdots & \vdots \\ 0 & \ldots & 0 & -\kappa_{n-1} & (\kappa_{n-1} + \kappa_n) & -\kappa_n \\ 0 & \ldots & 0 & & -\kappa_n & \kappa_n \end{bmatrix}.$$

The system in (2.33) can be defined by its the input-output mapping of each lumped element. The input at $i = 1$ yields the angular velocity $\dot{\theta}_0(t)$, and the output is the torque $T_0(t) = \kappa_1(\theta_1 - \theta_0)$. However, note that the input torque is given as $T_{a,1} = \kappa_1\theta_0(t)$. The input-output for each lumped element is then given by $T_i(t)$, $\dot{\theta}_i(t)$, respectively. Such configuration describes a lumped hybrid two-port system of a fixed-free drill string [31].

The lumped models presented in this section are formulated for simplicity, being derived from a distributed finite lump description. Hence, only the conservative forces such as inertia forces, restoring forces due to elasticity (not including permanent deformation) and gravity was included. In Tengesdal et al. [105] a generalization of (2.32), and (2.29) including forces and torques for a drilling system has been developed. The lumped-parameter approach to describe a drill string model for directional wells was given in Tengesdal et al. [103].

2.2.7 Assumed mode methods for torsional vibrations

An efficient solution procedure for linear PDEs in vibration analysis is the separation of variables (SV) technique. A description of this procedure can be found in Rao [84, Chapter 6.3], and an example from this reference is presented with minor modifications in this section for completeness. Besides directly imposing the lumped conditions of a finite element, by dividing into a finite set of segments, we will in this section introduce the assumed modes method, yielding a decoupled set of equations which can be used to characterize the vibrations in structures.

Consider the linear PDE of a torsional shear wave in (2.25), and its analytical solution by SV given as

$$\varphi(z,t) = \psi(z)\nu(t) \tag{2.34}$$

where $\psi(z)$ is the *mode shape* function required to satisfy the boundary conditions, and $\nu(t)$ is a time-dependent function to satisfy initial conditions. In SV the unforced response is analysed, yielding $T_a(z,t) = 0$. By substituting (2.34) into (2.25) we get

$$\frac{\partial^2 \nu(t)}{\partial t^2}\frac{1}{\nu(t)} = \frac{\partial^2 \psi(z)}{\partial z^2}\frac{GJ}{I_z^c \psi(z)} \tag{2.35}$$

where we have divided by $\psi(z)\nu(t)I_z^c$. For (2.35) to be valid in the sense of SV, both the left-hand and right-hand side must be equal to some constant, yielding

$$\frac{\partial^2 \nu(t)}{\partial t^2}\frac{1}{\nu(t)} = -\omega^2, \; \frac{\partial^2 \nu(t)}{\partial t^2} + \nu(t)\omega^2 = 0 \tag{2.36}$$

$$\frac{\partial^2 \psi(z)}{\partial z^2}\frac{GJ}{I_z^c \psi(z)} = -\omega^2, \; \frac{\partial^2 \psi(z)}{\partial z^2} + \frac{\omega^2}{c_s^2}\psi(z) = 0 \tag{2.37}$$

where $c_s^2 = G/\rho$ is the speed of sound of a shear wave in the material, and $I_z^c = \rho J$ due to symmetry. Hence, the solutions of (2.36) and (2.37) can be substituted into (2.34) yielding the free vibration response of a bar. What is of interest is to investigate the solution of (2.37), as it describes the torsional vibration pattern over the length of the structure. Its solution yields

$$\psi(z) = a_1 \cos(\kappa z) + a_2 \sin(\kappa z) \tag{2.38}$$

where $\kappa = \omega/c_t$. This implies that we have to determine the boundary conditions applying for our model, as mentioned in Section 2.2.5. We assume that the bar is fixed in one end, and free to vibrate in the other end[2]. This gives the following constraints on $\psi(z)$,

$$\begin{aligned} \varphi(0,t) = 0 \implies \psi(0) = 0 \\ GJ\frac{\partial \varphi}{\partial z}(L,t) = 0 \implies \frac{\partial \psi}{\partial z}(L) = 0 \end{aligned} \tag{2.39}$$

where the first states that no angular displacement is occurring at $z = 0$, and the external torque at $z = L$ is zero. Applying the conditions in (2.39) to (2.38), we obtain the *frequency* equation of the bar yielding

$$\cos(\kappa L) = 0 \tag{2.40}$$

[2]This end-boundary can in the simple case resemble rotation of a drill string in an off-bottom setting, for a vertical wellbore.

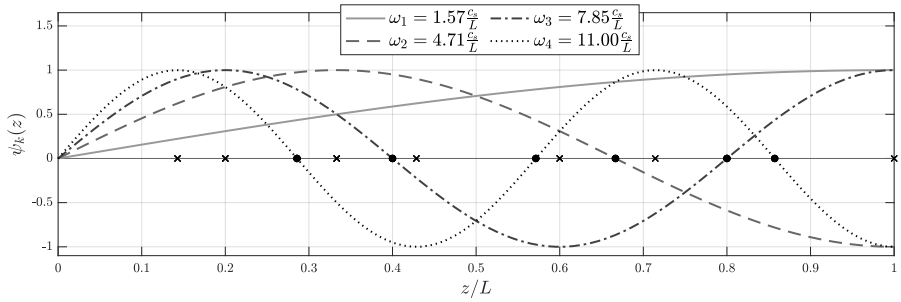

Figure 2.6: First four $\phi_k(z)$ for a bar fixed in $z = 0$ and free at $z = L$. The cross denotes the *antinodes*, and the circle denotes the *nodes*.

where $a_1 = 0$ and $a_2 = 1$ is assumed. The solution yields

$$\kappa_k L = \frac{(2k-1)\pi}{2},\ k = 1, \ldots, \infty \tag{2.41}$$

hence the associated natural frequencies are obtained from $\kappa_k^2 = \omega_k^2/c_s^2$ as

$$\omega_k = \sqrt{\frac{G}{\rho}}\frac{(2k-1)\pi}{2L},\ k = 1, \ldots, \infty \tag{2.42}$$

and its associated mode shape is then obtained from (2.38)

$$\psi_k(z) = \sin\left(\frac{\omega_k z}{c_s}\right) \tag{2.43}$$

The physical interpretation of the mode shape of angular deformation in (2.43) is that this is the twist along z described by ψ_k when the bar is vibrating at the natural frequency ω_k. A graph showing the first four mode shapes and their respective natural frequencies are presented in Figure 2.6.

The decoupled system of equations is derived next. Now we have defined how the model boundary conditions affect the deformation along z, and we will use this result in obtaining a representation of the velocities and accelerations along z. In the assumed mode formulation, the linear combination of the mode shapes, $\psi_k(z)$, represents the motion during time from any given initial condition. Hence,

$$\varphi(z,t) = \sum_{k=1}^{\infty} \psi_k(z)\eta_k(t) \tag{2.44}$$

where $\eta_k(t)$ is a generalized coordinate associated with the specific mode shape. These coordinates can then be structured into the total number of system generalized coordinates to describe

the configuration in time. Furthermore, by inserting (2.44) into (2.25), we get

$$I_z^c \sum_k^\infty \psi_k(z)\ddot{\eta}_k(t) - GJ \sum_k^\infty \psi_k''\eta_k(t) = T_a(z,t) \tag{2.45}$$

where $\psi_k''(z) = \partial^2\psi_k(z)/\partial z^2$. Inserting for (2.37) in the second term of (2.45), multiplying with the mode shape ψ_i, and integrating over the length, yields

$$\sum_k^\infty \left(I_z^c \int_0^L \psi_k\psi_i \mathrm{d}z\ddot{\eta}_k(t) + I_z^c\omega_k^2 \int_0^L \psi_k\psi_i \mathrm{d}z\eta_k(t) \right) = \int_0^L T_a(z,t)\psi_i \mathrm{d}z \tag{2.46}$$

where $I_z^c = \rho J$. By performing the summation, we get

$$I_z^c \int_0^L \psi_i^2 \mathrm{d}z\ddot{\eta}_k(t) + I_z^c\omega_i^2 \int_0^L \psi_i^2 \mathrm{d}z\eta_k(t) = \int_0^L T_a(z,t)\psi_i \mathrm{d}z \tag{2.47}$$

where the orthogonality of the mode shapes [61] has been used, given by

$$\int_0^L \psi_k\psi_i = 0, k \neq i. \tag{2.48}$$

Replacing the integrated term on the right-hand side of (2.47) with $T_a(t)\delta(z - z_i)\psi_i(z)\mathrm{d}z$, where δ is the Dirac-delta function. This ensures that $T_a(t)$ is applied at z_i, a point along z which the torque is directed to. This yields $T_a(t)\psi_i(z_i)$ on the right-hand side of (2.46). The simplified linear second-order modal decoupled equations of motion is then written as

$$I_i^c\ddot{\eta}_i(t) + \kappa_i\eta_i(t) = T_a(t)\psi_i(z_i) \tag{2.49}$$

where $I_i^c = I_z^c L/2$ is the modal moment of inertia, $\kappa_i = I_z^c\omega_i^2$ is the modal stiffness.

The assumed mode method was applied to describe the coupled torsional-lateral vibrations of a drill string segment, presented in Tengesdal et al. [104]. The mode shapes in (2.43) are then incorporated in the formulation of the inertia and stiffness matrices of the model. From a computational perspective, the number of included modes for representation of wanted system frequencies resulted in a smaller model state-space, compared to dividing the structure into a large number of lumped elements. Using the assumed mode method with a finite number of modes in combination with the Bond Graph methodology (see, e.g., Karnopp et al. [61, Chapter 10] and Margolis and Karnopp [68])), can provide useful lumped-parameter models being easily coupled to other systems.

2.2.8 Natural frequencies

An undamped torsional pendulum is obtained by setting $n = 1$ in (2.32), assuming a symmetric cross-section, and that $\theta_0(t) = 0$, the equation of motion is given as

$$\rho JL\ddot{\theta}(t) + \frac{GJ}{L}\theta(t) = 0 \tag{2.50}$$

where $\rho J = I_z^c$, and $L = \Delta z$. From (2.50), the fundamental frequency is given by $\omega = \sqrt{(G/\rho)}/L$. From (2.42), the exact fundamental frequency ($k = 1$) is

$$\omega_1 = \frac{\pi}{2L}\sqrt{\frac{G}{\rho}} = \frac{\pi}{2L}c_s. \tag{2.51}$$

Suppose that $I_{z,1}^c = \ldots = I_{z,n}^c = I_z^c$, and that for $\kappa_1 = \ldots = \kappa_n = \kappa$. Consider n discrete elements with distance $l = L/n$ between each lumped element. Using modal analysis, we can obtain the lumped system natural frequencies by assuming that $\boldsymbol{\theta} = \tilde{\boldsymbol{v}}\cos(\omega t - \Phi)$, i.e., that the masses oscillates with the same frequency ω. The lumped system natural frequencies from the eigenvalue decomposition are obtained by

$$\boldsymbol{\mathcal{I}}^{-1}\boldsymbol{\mathcal{K}}\tilde{\boldsymbol{v}} = \lambda\tilde{\boldsymbol{v}} \tag{2.52}$$

where $\tilde{\boldsymbol{v}}$ is the amplitude of the oscillations for each mode, and $\lambda = \omega_i^2$. For increasing n, using $J = 1\ \mathrm{m}^4$, $L = 1000\ \mathrm{m}$, $G = 8000\ \mathrm{MPa}$ and $\rho = 8000\ \mathrm{kg\,m}^{-3}$, the natural frequencies are displayed in Table 2.1.

Table 2.1: Natural frequencies of an idealized undamped lumped torsional model.

	(2.42)	(2.52)		
	-	$n = 2$	$n = 10$	$n = 100$
$\omega_1\ [\mathrm{rad\,s}^{-1}]$	4.97	3.91	4.73	4.94

From the values in Table 2.1, it is clear that the natural frequencies of the lumped system are under estimating the fundamental frequency if n is small. However, larger n will bring the discretized system closer to its true continuum solution, with the cost of a larger state-space for the model.

2.3 Friction modelling

In the modelling of drilling systems, the most immediate part of the system to characterizing the uncertain nature by cutting rock is the friction forces and torques generated at the boundary between the drill string and the borehole. Extensive progress has been made in the recent years on empirical models representing the phenomena observed both in the field and by experiments, and a good overview is given in [93].

Friction occurs as a counter-acting force or torque from the imposed movement of two surfaces in contact. In material sciences, the term *asperities* are used to characterize the rugged surface on a microscopic scale.

Friction interaction can roughly be divided into a *stiction*, a *break-away* and a *slip* phase. In the first phase, the friction given by the relative motion is larger than the object applied force.

As soon as the external forces reaches the break-away force, the object starts to slip. This effect is denoted *stick-slip* motion. Simulations of systems modelled with strong friction interaction such as stick-slip, can be challenging in terms of stability in numerical solvers, correct physical interpretation, and input-output mapping [60].

2.3.1 Static models

Static friction models represent the friction being dependent on the relative velocity of the surfaces. Static in the sense that the model form an input-output map with no internal history of the applied inputs, state variables, and its output. In its most common form, the friction of two dry sliding surfaces is a force proportional to the direction of the velocity, given as

$$F_f = F_{\text{co}}\text{sign}(v_r) \tag{2.53}$$

where F_{co} denotes the Coulomb friction force – a friction shear force from the asperities between the surfaces, $v_r = v - v_s$ is the relative velocity of the surfaces, v is the velocity of the moving object, v_s is the surface velocity, and $\text{sign}(v_r)$ is the set-valued *signum* function defined as

$$\text{sign}(x) = \begin{cases} 1 & x > 0 \\ 0 & x = 0 \\ -1 & x < 0 \end{cases}. \tag{2.54}$$

The Coulomb friction force in (2.53) is given by the load F_n of the object perpendicular to the sliding surface, and a coefficient of friction μ_k denoted the *kinetic friction factor* (subscript k). Hence (2.53) is rewritten

$$F_f = \mu_k F_n \text{sign}(v_r) \tag{2.55}$$

where $F_{\text{co}} = \mu_k F_n$. Note that stiction applies when the relative velocity is zero, and $|F_f| < F_{\text{s}}$ where F_s is the static friction force. The static friction force is limited to $|F_s| \leq \mu_s |F_n|$, hence, it will oppose the objects ability to move as long as the external forces from the system are below its threshold. Note that the static and Coulomb friction are separated by $\mu_k < \mu_s$ where subscript k indicate *kinetic* while s denote *static*.

The friction force in (2.55) is for dry friction, while in the domain of oil & gas drilling, most of the surfaces in contact are lubricated by a fluid film. As such, including a viscous effect is beneficial to improve the model. Viscous friction are typically modelled proportional to the magnitude and direction of the relative velocity, and in combination with (2.55), gives the force

$$F_{\text{cv}} = F_f + c_v v_r \tag{2.56}$$

where c_v is a coefficient of viscous friction typically dependent on the surface lubricant, geometry of the surfaces in contact, etc. (In the case of drilling, this coefficient represent effects such

as lumped drag forces due to pipe motion in mud). An observation that friction decreased to a low point when $v_r \neq 0$, as the dry contact between the object and surface were fully lubricated, is denoted the *Stribeck effect* first described by Stribeck in 1902 [56]. One approach to model this nonlinear effect is given as [6]

$$F_{\text{cv}} = F_f + (F_s - F_{\text{co}})e^{-(v_r/\tilde{v})^2}\text{sign}(v_r) + c_v v_r \tag{2.57}$$

where F_s is the static friction force, and $\tilde{v}$ is the characteristic Stribeck-velocity defining the slope of the friction force decay. Note that for $v_r \to 0$, $|F_{\text{cv}}|$ approaches $|F_s|$.

For implementation in simulation and use in control systems, the condition for zero velocity needs to be addressed. For the static models implemented with the *sign* function the friction forces is zero in the instant of $v_r = 0$. In a simulation model, the external and inertia forces in the system will then start to accelerate the object. The implication of this is an oscillatory system state for v_r in the neighbourhood of the origin, which has nothing to do with the physics of the system. Hence, this means that the object should, in the moment of zero velocity, be at rest as the friction counteracts the entire motion of the object.

A simplified modification of the friction force to overcome the challenges of system implementation was presented by Karnopp [60]. In this approach, a zone around v_r close to zero defined by δ_v was included to capture frictional stiction at zero velocity.

The applied forces in the system are taken into account. In terms of (2.57) and noting that the system applied force must overcome the static friction F_s to move, we have

$$F_{\text{K}} = \begin{cases} F_{\sum}, & |v_r| \leq \delta_v,\ |F_{\sum}| \leq F_s \\ F_s\text{sign}(F_{\sum}), & |v_r| \leq \delta_v,\ |F_{\sum}| > F_s \\ F_{\text{cv}}\ (2.57), & |v_r| > \delta_v \end{cases} \tag{2.58}$$

where $F_{\sum}$ is the sum of all of the external forces from the system computed when $|v_r| \leq \delta_v$, which is approximated by the zone δ_v. The first condition yields stiction, where the external forces are too small to overcome the static friction. The second condition yields a stick-slip transition, since at this moment the static force exceeds the break-away force and the friction force is characterized by the magnitude of the F_s and the direction of the sum of forces. After break-away, the object starts to slide (condition three), and Coulomb friction, viscous friction and the Stribeck effect describes the friction force. The three static friction models discussed until this point are sketched in Figure 2.7a.

In [65], a switch model was proposed. Instead of generating the friction force based on a conditional statement, the system state $\boldsymbol{x} = [x,\, v]^\top$ where x, v is the object position and velocity, was given by three conditions in the case of stick, transition stick-to-slip, and in the slip phase. It was argued that this approach was numerically more stable. Two interesting models was also proposed in [64], applying the parameters of the system model and the fixed time-step to determine the friction force such that the velocity reaches zero in finite time.

Continuous representations of the discontinuous curve in Figure 2.7a, have been proposed in literature (see, e.g., [18, 65, 72]). Hence, the Coulomb friction curve can be approximated by

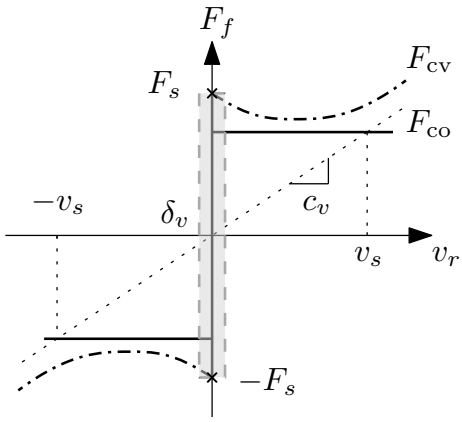

(a) Coulomb (solid line), viscous plus Stribeck (dash-dotted) in (2.57), and the zero-velocity zone in the Karnopp model (dashed-grey area marks δ_v, with F_{cv} as the slip friction force) from (2.58). The upper limit given by the static friction is marked with a cross.

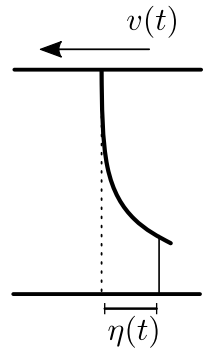

(b) The definition of bristle displacement in dynamic friction models. Adapted with modifications from [81].

Figure 2.7: Friction force curves, and the bristle displacement.

a smooth function, such as

$$\tilde{F}_{\text{co}} = \mu_k F_n \frac{2\arctan(\gamma_1 v_r)}{\pi(1+\gamma_2|v_r|)} \tag{2.59}$$

where γ_1 and γ_2 represent the steepness and exponential decay of the Stribeck effect for the continuous friction force. In the simplest case, $\tilde{F}_{\text{co}} = \mu_k F_n \arctan(v_r/v_0)$ where v_0 is a velocity tolerance [81].

As a final note to this section, typically modern numerical solvers include zero-crossing detection for v_r, with adaptive time-step algorithms. Hence, static friction models such as (2.55) can be utilized. When using constant time-step in numerical integration, commonly applied in explicit solvers such as the *Forward Euler* and *Runge-Kutta* (see Section 2.5), the time step is often required to be very small due to the discontinuity of the friction model. Hence, lower time-steps are used to capture the stiction effects when the relative velocity approaches zero. In those cases, the Karnopp model can be more efficient. However, it serves as an approximation due to the zero-velocity zone.

2.3.2 Dynamic models

A disadvantage with the use of static friction models is the switching required at zero velocity. Additionally, dynamic effects reported in experiments such as variations in displacement

(referred to as pre-sliding) during stiction, friction lag, and hysteresis are not present in static models [80]. Dynamic models have been argued to be more accurate than static models, provided that the parameters representing the dynamic effects are adequately given [64].

The Dahl model was one of the earliest dynamic models, including the static Coulomb friction and an approximation of the pre-sliding effect. This model created the basis for further dynamic model development. The physical interpretation of the model is drawn towards the stiffness of asperities represented by elastic bristles, shown in Figure 2.7b. Further on, we assume that one surface is stationary such that $v_r(t) = v(t)$, which is typically the case when material is being cut. The Dahl model can be expressed as a first-order low-pass filter given as [80]

$$\dot{F}_{\mathrm{D}} = -\sigma_0 \frac{|v(t)|}{F_{\mathrm{co}}} F_{\mathrm{D}} + \sigma_0 \mathrm{sign}(v(t)) \tag{2.60}$$

where σ_0 is described as the stiffness of the bristle, and it is noted that the model time-constant $T_{\mathrm{D}} = F_{\mathrm{co}}/\sigma_0|v| \to \infty$ as velocity approaches zero.

Let $\bar{F}_{\mathrm{D}}$ denote the steady-state friction force, and for $\dot{F}_{\mathrm{D}} = 0$ we get

$$0 = -\sigma_0 \frac{|v(t)|}{F_{\mathrm{co}}} F_{\mathrm{D}} + \sigma_0 \mathrm{sign}(v(t)) \implies \bar{F}_{\mathrm{D}} = F_{\mathrm{co}} \frac{v}{|v|} \tag{2.61}$$

which is the Coulomb friction given in (2.53). The Dahl model can be considered efficient both in terms of implementation and simulation. However, this model does not include stiction and the Stribeck effect as described in [47, 80]. In [98], they propose a model building on the smooth approximations of the static laws from Section 2.3.1, and additionally model the hysteresis effect and memory by including a first-order low-pass filter similar to (2.60).

A generalization of the Dahl model in (2.60), was developed by de Wit et al. [24] and named the *Lund-Grenoble* (LuGre) model. The same physical interpretation that the bristles acts as springs, deforming during an increase in internal loading, is applied. The bristle deflection is introduced as a model state, and the governing equations are given as

$$F_{\mathrm{lg}} = \sigma_0 \eta + \sigma_1 \dot{\eta} + \sigma_2 v \tag{2.62}$$

$$\dot{\eta} = v - \sigma_0 \frac{|v|}{h_{\mathrm{lg}}(v)} \eta \tag{2.63}$$

$$h_{\mathrm{lg}}(v) = (F_{\mathrm{co}} + (F_s - F_{\mathrm{co}}) e^{-|v/v_s|^2}) \tag{2.64}$$

where η is the internal friction state representing the mean deflection between the surfaces in contact, σ_0 is the spring stiffness coefficient of the bristle, σ_1 is the corresponding damping coefficient, σ_2 is the viscous frictional damping coefficient, and $h_{\mathrm{lg}}(v) > 0$ is a nonlinear function typically representing the Stribeck effect.

In steady-state, when $\dot{\eta} = 0$, the bristle deflection $\bar{\eta}$ is given as

$$\bar{\eta} = \frac{v}{\sigma_0 |v|} h_{\mathrm{lg}} \tag{2.65}$$

which gives the steady-state friction force from (2.62) as

$$\bar{F}_{\text{lg}} = \sigma_0 \bar{\eta} = h_{\text{lg}}(v)\text{sign}(v) + \sigma_2 v \tag{2.66}$$

which combines Coulomb friction and the Stribeck effects together with viscous friction as in (2.57).

Dynamic friction models have the advantage of being accurate in describing hysteresis and friction lag, and are well-defined for $v_r = 0$. In terms of simulation, in large-scale simulations where friction is influencing the equations of motion of many states, the dynamic model will increase the state-space of the overall system. As such, implementations of static friction models has received larger attention in systems with an already large state-space experiencing stick-slip [81].

A Bond graph approach of the LuGre model was formulated in Tengesdal et al. [104], to be included in the component-simulation study. Hence, the bristle velocity and relative surface velocity was rearranged as

$$\dot{\phi} - \dot{\varphi}(L,t) = -\sigma_0 h_{\text{lg}}(\dot{\varphi}(L,t), F_n) \tag{2.67}$$

where $\dot{\phi}$ is the angular velocity of the bristle deflection, $\dot{\varphi}(L,t)$ is the angular velocity of the drill string bit, and F_n represents the normal force, i.e., the weight-on-bit. Furthermore, the BG element *zero junction*, an element for summing up the velocities of adjacent inertias, could be applied.

2.4 Linear time-delay systems

In literature, the bit-rock models are often represented by a variant of Coulomb friction with viscous effects due to the lubrication effect of the mud flow in the wellbore (see, e.g., de Wit et al. [25] for proposing a control law using a dynamic friction model, Navarro-Lopez and Suarez [74] for an application of the Karnopp zero-velocity model [60], and Real et al. [85] proposing a regularization of a friction model). A friction model being discontinuous, which is commonly the case for static models, will then yield a system with a *set* of equilibrium points.

The process of drilling rock is closely related to the dynamics of material cutting, where the volume of material being cut by the tool, is typically dependent on the rotational speed of the work-piece. Time-delays in the system dynamics appear due to the cutting tool being stuck on the material for a period of time [46]. The effect of time-delays to describe the stability in axial and torsional drilling systems has previously been addressed [23, 32, 88].

In the presence of a time-delay, the linear system in (2.2) can be written as

$$\dot{\boldsymbol{x}} = \mathbf{A}\boldsymbol{x} + \mathbf{A}_\tau \boldsymbol{x}(t-\tau) \tag{2.68}$$

where $\mathbf{A}_\tau \in \mathbb{R}^{n_x \times n_x}$ is the state delay matrix, and τ is the delay in the time unit of the system. As described in Sipahi [96], $t = 0$ is assumed to be the common reference point in time.

Compared to (2.2), where a finite set of initial conditions applies, the explicit nature of the introduced time-delay yields an infinite-dimensional solution space, requiring definition of an initial condition function [96]. Moreover, for the solution of (2.68) to be uniquely defined, an initial continuous history function given by $w_i(t) \in \{[-\tau, 0), \mathbb{R}\}$ is needed, in which $x_i(t) = w_i(t)$ for $t \in [-\tau, 0)$ and x_i is a vector component of $\boldsymbol{x}$.

Methods of characterizing stability in linear time-invariant systems are well known, and commonly confined to investigating the characteristic polynomial obtained from (2.68). This equation determines behaviour of the system.

Using the Laplace transform of $\dot{\boldsymbol{x}}(t)$ given as

$$\mathcal{L}(\dot{\boldsymbol{x}}(t)) = s\mathbf{X}(s) - \boldsymbol{x}(0) \tag{2.69}$$

where $\mathcal{L}$ is the Laplace operator, and noting that $\mathcal{L}(\boldsymbol{x}(t-\tau)) = \mathbf{X}(s)e^{-s\tau}$, the characteristic equation of (2.68) is given by

$$f(s, \tau) \triangleq \det(s\mathbf{I} - \mathbf{A} - \mathbf{A}_\tau e^{-\tau s}) \tag{2.70}$$

where s is the Laplace variable, and $\boldsymbol{x}(0) = \mathbf{0}$ is assumed for the time-domain system dynamics. This equation is commonly referred to as a quasi-characteristic polynomial due to the exponential term [96]. The polynomial in (2.70) generates an infinite number of roots due to the exponential function [46]. In order to investigate the stability of this system, with $\tau \geq 0$, the critical roots and time-delays generating crossings are investigated. These are defined by the frequency ω at the imaginary axis for $s = j\omega$, where j is the imaginary unit defined by $j^2 = -1$.

Building on the material from previous work, a discussion of the stability for a drilling system related to nominal critical speed margins for second-order lumped-multi-element models was given in Tengesdal et al. [105]. The nominal critical speed margins were then inversely proportional to the time-delay τ.

2.5 Numerical methods

A model consisting of ODEs developed from first principles or by empirical methods is either solved analytically or by numerical integration to examine the model behaviour in time. The first approach is often based on the application of the Laplace transform, hence, the model is linear and can be structured as (2.2). For nonlinear models, exact solutions by analytical derivation might be challenging or even impossible to obtain. For these models, numerical integration methods are more convenient. Moreover, methods for solving (2.1) forward in time, with initial value $\boldsymbol{x}(t_0)$.

The mth-order Taylor expansion of $\dot{\boldsymbol{x}}(t_k + h)$ around t_k being a discrete time-sample with h being a defined time-step is expressed as

$$\boldsymbol{x}(t_k + h) = \boldsymbol{x}(t_k) + h\dot{\boldsymbol{x}}(t_k) + \frac{1}{2}h^2\ddot{\boldsymbol{x}}(t_k) + \ldots + \frac{1}{(m)!}h^{(m)}\boldsymbol{x}^{(m)} \tag{2.71}$$

where $\boldsymbol{x}^{(m)}$ denotes the mth time-derivative of $\boldsymbol{x}$. Inserting for the unforced function in (2.1) for $\dot{\boldsymbol{x}}$, and only including the linear terms, a numerical approximation of the solution can be given as

$$\boldsymbol{x}_{k+1} = \boldsymbol{x}_k + h\boldsymbol{f}(\boldsymbol{x}_k, t_k) \tag{2.72}$$

where $\boldsymbol{x}_{k+1}$ is the states of the system at $t_k + h$, t_k is the time for the sampled states, and $h = t_{k+1} - t_k$ can be defined as the time-step. Equation (2.72) is the one-step Forward Euler method.

The *local error* is defined as the error between the numerical solution and the exact solution for t_k to $t_k + h$, i.e., one time step. For the Euler method, the local error can be given as

$$\boldsymbol{e}_{k+1} = \boldsymbol{x}(t_k + h) - \boldsymbol{x}_{k+1}. \tag{2.73}$$

Assuming that at least the second derivative of $\boldsymbol{x}$ can be obtained, (2.71) can be expressed as

$$\boldsymbol{x}(t_k + h) = \boldsymbol{x}(t_k) + h\dot{\boldsymbol{x}}(t_k) + \frac{1}{2}h^2\ddot{\boldsymbol{x}}(t_k) + \dots \tag{2.74}$$

$$= \boldsymbol{x}_k + h\boldsymbol{f}(\boldsymbol{x}(t_k), t_k) + \mathcal{O}(h^2) \tag{2.75}$$

where $\boldsymbol{x}_k = \boldsymbol{x}(t_k)$, and the notation $\mathcal{O}(h^m)$ denotes the higher-order terms. The order notation is given as

Definition 2.2 ([62, Def. 10.1])**.** $\delta_1(\epsilon) = \mathcal{O}(\delta_2(\epsilon))$, if there exist positive constants k and c such that

$$|\delta_1(\epsilon)| \leq k|\delta_2(\epsilon)|, \; |\epsilon| \leq c$$

Moreover, if the error is of order $\mathcal{O}(\epsilon)$ the norm of the error is less than $k|\epsilon|$.

To obtain the local error of the Euler method, (2.72) and (2.75) are substituted into (2.73), yielding

$$\boldsymbol{e}_{k+1} = \mathcal{O}(h^2) \tag{2.76}$$

stating that the local error is of order $\mathcal{O}(h^2)$, and according to [31], $\boldsymbol{e}_{k+1} = \mathcal{O}(h^{\sigma+1})$ where σ is the order of the method. Hence, the Euler method in (2.72) is of first order.

The *global error* can be defined by the difference of the numerical and exact solution from t_0 to $t_k + h$, which according to [13] is of order $\mathcal{O}(h)$ for the Euler method, meaning that h is proportional to the order of accuracy desired.

Numerical stability for integrators can be studied under the assumption of a linear *test* system, formally known as the *Dahlquist test equation* $\dot{x}(t) = \lambda x(t)$ [48]. Applying this equation to a scalar version of the Euler method in (2.72), we get

$$x_{k+1} = x_k + h\lambda x_k = (1 + h\lambda)x_k \tag{2.77}$$

and its *stability function* is then defined according to [31] as

$$R = 1 + h\lambda. \tag{2.78}$$

A set characterizing the stability domain of the numerical method is given as [48]

$$S = \{\lambda h \in \mathcal{C}; |R(\lambda h)| \leq 1\} \tag{2.79}$$

and for the Euler method, the stability domain is then obtained as

$$|R| = |1 + h\lambda| \leq 1 \tag{2.80}$$

which is a circle of radius 1, with centre in -1. Moreover, the time-step is required to be $h \leq -2/\lambda_i$ for real eigenvalues of the system, to ensure numerical stability.

A robust numerical method can be referred to as *A-stable*, if the method is stable in the entire left-half plane for $\mathrm{R_e}(\lambda h) < 0$, denoting the real part, i.e., no restrictions on the Dahlquist test system [48]. For an extensive discussion on the topic of numerical integrator stability, including stability regions for several methods, the interested reader is referred to, e.g., Hairer and Wanner [48] and Egeland and Gravdahl [31, Ch. 14].

2.5.1 Runge-Kutta methods

A Runge-Kutta method computes the function values of (2.1) for points on the interval $t_k + h$. As such, the method is of higher-order given the number of *stages* being computed, and a final calculation is a linear approximation of all the stages for $\boldsymbol{x}_{k+1}$. The stage computations and state vector solutions for the next time-step are given as

$$\begin{aligned} \boldsymbol{k}_i &= \boldsymbol{f}(\boldsymbol{x}_k + h\sum_{j=1}^{\sigma} a_{ij}\boldsymbol{k}_j, t_k + c_i h) \\ \boldsymbol{x}_{k+1} &= \boldsymbol{x}_k + h\sum_{i=1}^{\sigma} b_i \boldsymbol{k}_i \end{aligned} \tag{2.81}$$

where a_{ij} is the weighting parameters for stage computations, b_j weights the individual contributions in the total solution, c_j denotes the interpolation parameters. Note that $\sum_i^{\sigma} b_i = 1$ is required for consistency, and necessary fo the RK method to be convergent [13].

The Runge-Kutta coefficients are collected in a Butcher array with dimensions depending on the order σ, given on the form

$$\begin{array}{c|ccc} c_1 & a_{11} & \dots & a_{1\sigma} \\ \vdots & \vdots & \ddots & \vdots \\ c_\sigma & a_{\sigma,1} & \dots & a_{\sigma,\sigma} \\ \hline & b_1 & \dots & b_\sigma \end{array} = \begin{array}{c|c} \boldsymbol{c} & \mathbf{A} \\ \hline & \boldsymbol{b}^\top \end{array} \tag{2.82}$$

where $0 \leq c_1 \leq \ldots \leq c_\sigma \leq 1$, $\boldsymbol{c} = \mathbf{A}\boldsymbol{l}$, where $\mathbf{A} = \{a_{ij}\}$, $\boldsymbol{l} = [1, \ldots, 1]^\top$, and an explicit RK method is achieved by $a_{ij} = 0$ for $i \leq j$, i.e., the elements a_{ij} in (2.82) are zero in the upper triangle.

A common RK configuration is the order four explicit method with $\sigma = 4$. The matrix of a_{ij} coefficients, c_i and b_i are given as

$$\mathbf{A} = \begin{bmatrix} 0 & 0 & 0 & 0 \\ \frac{1}{2} & 0 & 0 & 0 \\ 0 & \frac{1}{2} & 0 & 0 \\ 0 & 0 & 1 & 0 \end{bmatrix}, \boldsymbol{c} = \begin{bmatrix} 0 & \frac{1}{2} & \frac{1}{2} & 1 \end{bmatrix}, \boldsymbol{b} = \begin{bmatrix} \frac{1}{6} & \frac{1}{3} & \frac{1}{3} & \frac{1}{6} \end{bmatrix} \tag{2.83}$$

By applying the method in (2.72) and (2.81) to obtain a solution forward in time for second order systems, the state vector needs to be rewritten in first-order form.

2.5.2 Variations of Euler and Runge-Kutta methods for stochastic systems

In cases where the effects of uncertainty in the system is important, models described by Stochastic Differential Equations (SDE) are relevant. This section includes two variations of the Euler and RK method for SDEs. The general form of an unforced system described by an SDE is given as

$$\mathrm{d}\boldsymbol{x}(t) = \boldsymbol{f}(\boldsymbol{x}, t)\mathrm{d}t + \boldsymbol{g}(\boldsymbol{x}, t)\mathrm{d}\boldsymbol{v}(t) \tag{2.84}$$

where $\boldsymbol{f}$ is the deterministic part (equal to (2.1)) of the SDE denoted the *drift* function, $\boldsymbol{g} \in \mathbb{R}^{n_x \times n_v}$ is a matrix of diffusion terms, $\boldsymbol{v} \in \mathbb{R}^{n_v \times 1}$ is a vector of standard Wiener processes, given on the time interval $t \in [t_0, t_f]$. Moreover, if $\boldsymbol{g}$ depend linearly on $\boldsymbol{x}$ the noise is multiplicative, and if $\boldsymbol{g}$ is a matrix of constant values, the noise is additive.

The standard Wiener process $\boldsymbol{v}(t)$, or Brownian motion, is defined by its increments $\boldsymbol{v}(t) - \boldsymbol{v}(s)$, where $s, t \in \mathbb{R}$, being normally distributed with zero mean and variance $\boldsymbol{\sigma}^2 = \mathbf{I}(t - s)$ [12].

It is convenient to express discretized Brownian motion $\boldsymbol{v}(t)$[3] for t_k to be evaluated by numerical integration methods. The discretized Brownian motion with individual discrete increments is given as

$$\Delta\boldsymbol{v}_k = \boldsymbol{v}_k - \boldsymbol{v}_{k-1}, \ \boldsymbol{v}_0 = \mathbf{0}, \ k = 1, \ldots, N \tag{2.85}$$

[3]Note that in [100], the $\mathrm{d}\boldsymbol{v}_k$ notation was used on the discrete Brownian motion, hence, the separation of the continuous counterpart was indicated by the subscript k.

where $\Delta \boldsymbol{v}_k \sim \mathcal{N}(0, \mathbf{I}\sqrt{h})$, $t_k = kh$, and $N = t_f/h$ is the number of increments from t_0 to t_f.

The numerical integration of an SDE in (2.84) have been based on approximating the integrand of the diffusion term. An approximation of the stochastic part of (2.84) and its integral is necessary due to the nondifferentiable state of d$\boldsymbol{v}$ (the variable is not related to any past or present values). The stochastic integral is expressed according to [49]

$$\int_0^{t_f} \boldsymbol{g}(\boldsymbol{x}, t)\mathrm{d}\boldsymbol{v} = \lim_{h\to 0} \sum_{k=0}^{N-1} \boldsymbol{g}(\boldsymbol{x}_k, t_k)\Big(\boldsymbol{v}(t_{k+1}) - \boldsymbol{v}(t_k)\Big) \tag{2.86}$$

where $t_k = kh$, and the right-hand side is the Riemann Sum. Note that (2.86) evaluates the integral at t_k, i.e., the left-hand points on the interval, denoted the Itô form, and a mid-point evaluation of the integral is denoted the Stratonovich form [17]. Consequently, the methods of approximating (2.84) are based on one of the two. A mapping is possible between the two, and the choice depend on the analysis [13]. In this section we consider the Itô form, as this form is the basis for the RK method applied in Tengesdal and Holden [100].

The Euler-Maruyama method can be applied for numerical integration of (2.84), being easy to implement, and is given as

$$\boldsymbol{x}_{k+1} = \boldsymbol{x}_k + h\boldsymbol{f}(\boldsymbol{x}_k, t) + \boldsymbol{g}(\boldsymbol{x}_k, t)\Delta \boldsymbol{v}_k \tag{2.87}$$

where the $\Delta \boldsymbol{v}_k$ noise increments can be computed by a random number generator for $\mathcal{N}(0, 1)$ scaled with $\sqrt{h}$. The Euler-Maruyama method has convergence[4] of order 1/2 and reduces to (2.72) for $\boldsymbol{g} = \mathbf{0}$.

For increased accuracy of approximating the stochastic integral, stochastic methods of the Runge-Kutta integrators have been developed ([91] for convergence to the Itô solution, [13] for the Stratonovich solution, and [92] for both). A stochastic Runge-Kutta (SRK) method of order 3 was developed by Rößler [91], given as

$$\boldsymbol{x}_{k+1} = \boldsymbol{x}_k + \sum_{i=1}^{\sigma} h\alpha_i \boldsymbol{f}(\bar{\boldsymbol{k}}_{i,0}, t_{i,0}) + \gamma_{i,1}\boldsymbol{g}(t_{i,1}, \bar{\boldsymbol{k}}_{i,1})\Delta \boldsymbol{v}_k + \gamma_{i,2}\boldsymbol{g}(\bar{\boldsymbol{k}}_{i,1}, t_{i,1})\frac{1}{2\sqrt{h}}\hat{\boldsymbol{v}}_k \tag{2.88}$$

where $t_{i,p} = t_k + c_{i,p}h$ for $p = 0,\ 1$, $\boldsymbol{c}_p = \mathbf{A}_s^{[p]}\boldsymbol{l}$ is the weights, with $\mathbf{A}_s^{[p]} = \{a_{ij}^{[p]}\}$, and the elements of the vector $\hat{\boldsymbol{v}}_k$ are given by $\Delta v_{\cdot,k}^2 - h$, and the stage computations are given as

$$\bar{\boldsymbol{k}}_{i,0} = \boldsymbol{x}_k + \sum_{j=1}^{\sigma} ha_{ij}^{[0]}\boldsymbol{f}(\bar{\boldsymbol{k}}_{j,0}, t_{j,0}) + \sum_{j=1}^{\sigma} b_{ij}^{[1][0]}\boldsymbol{g}(\bar{\boldsymbol{k}}_{j,1}, t_{j,1})\Delta \boldsymbol{v}_k \tag{2.89}$$

$$\bar{\boldsymbol{k}}_{i,1} = \boldsymbol{x}_k + \sum_{j=1}^{\sigma} ha_{ij}^{[1]}\boldsymbol{f}(\bar{\boldsymbol{k}}_{j,0}, t_{j,0}) + \sum_{j=1}^{\sigma} b_{ij}^{[3][1]}\boldsymbol{g}(\bar{\boldsymbol{k}}_{j,1}, t_{j,1})\bar{\boldsymbol{h}} \tag{2.90}$$

[4]The order of convergence is defined as *strong*. See e.g., [13], for the definitions related to *strong* or *weak* order of convergence for the SDEs. This is not further elaborated in this thesis.

where the elements of the vector $\bar{\boldsymbol{h}} = [\sqrt{h}, \ldots, \sqrt{h}]^\top$. Note that if $\boldsymbol{g} = \boldsymbol{0}$ the scheme reduces to the RK methods presented in Section 2.5.1. The modified Butcher table for the SRK in Rößler [91] is given as

$$\begin{array}{c|ccc|ccc|ccc}
c_{10} & a_{11}^{[0]} & & a_{1\sigma}^{[0]} & b_{11}^{[1][0]} & & b_{1\sigma}^{[1][0]} & & & \\
\vdots & \vdots & \ddots & \vdots & \vdots & \ddots & \vdots & & & \\
c_{\sigma 0} & a_{\sigma 1}^{[0]} & & a_{\sigma\sigma}^{[0]} & b_{\sigma 1}^{[1][0]} & & b_{\sigma\sigma}^{[1][0]} & & & \\
\hline
c_{11} & a_{11}^{[1]} & & a_{1\sigma}^{[1]} & b_{11}^{[3][1]} & & b_{1\sigma}^{[3][1]} & & & \\
\vdots & \vdots & \ddots & \vdots & \vdots & \ddots & \vdots & & & \\
c_{\sigma 1} & a_{\sigma 1}^{[1]} & & a_{\sigma\sigma}^{[1]} & b_{\sigma 1}^{[3][1]} & & b_{\sigma\sigma}^{[3][1]} & & & \\
\hline
 & \alpha_1 & \ldots & \alpha_\sigma & \gamma_{11} & \ldots & \gamma_{\sigma 1} & \gamma_{12} & \ldots & \gamma_{\sigma 2}
\end{array} \tag{2.91}$$

where an explicit method is given by $a_{ij}^{[0]} = a_{ij}^{[1]} = b_{ij}^{[1][0]} = b_{ij}^{[3][1]} = 0$ for $i \leq j$. Suppose $\sigma = 1$, $a_{11}^{[0]} = a_{11}^{[1]} = 0$, $b_{11}^{[1][0]} = b_{11}^{[3][1]} = 0$, $\alpha_1 = \gamma_{11} = 1$ and $\gamma_{12} = 0$, then, (2.87) is obtained.

An explicit SRK method RI1W1 of deterministic order 3 and SRK order of 2 [91], is given by

$$\begin{array}{c|ccc|ccc|ccc}
0 & 0 & 0 & 0 & 0 & 0 & 0 & & & \\
\frac{2}{3} & \frac{2}{3} & 0 & 0 & 1 & 0 & 0 & & & \\
\frac{2}{3} & -\frac{1}{3} & 1 & 0 & 0 & 0 & 0 & & & \\
\hline
0 & 0 & 0 & 0 & 0 & 0 & 0 & & & \\
1 & 1 & 0 & 0 & 1 & 0 & 0 & & & \\
1 & 1 & 0 & 0 & -1 & 0 & 0 & & & \\
\hline
 & \frac{1}{4} & \frac{1}{2} & \frac{1}{4} & \frac{1}{2} & \frac{1}{4} & \frac{1}{4} & 0 & \frac{1}{2} & -\frac{1}{2}
\end{array} \tag{2.92}$$

Useful toolboxes have been developed including the two methods and methods of higher-order convergence involving implicit methods. The reader is referred to [40], for the `SDELab` package for `MATLAB`.

2.5.3 Numerical integration of second-order systems

One of the earlier numerical algorithms for solving structural systems described by second-order ODEs was proposed by Newmark [75]. Instead of formulating the second-order system into a state-space vector as (2.1), the matrices derived in Section 2.2.6 are used directly in the integration method. This is favourable in terms of not increasing the dimension of the simulated system.

The second-order system given in (2.29) from Section 2.2.6 is rewritten in a general matrix form including proportional damping as

$$\mathbf{M}\ddot{\boldsymbol{q}}(t) + \mathbf{D}\dot{\boldsymbol{q}}(t) + \mathbf{K}\boldsymbol{q}(t) = \boldsymbol{\tau}(t) \tag{2.93}$$

where $\ddot{\boldsymbol{q}} \in \mathbb{R}^{n\times 1}$ is the vector linear accelerations, $\boldsymbol{q} \in \mathbb{R}^{n\times 1}$ is the vector of linear displacements, $\mathbf{M} \in \mathbb{R}^{n\times n}$ is inertia matrix, $\mathbf{K} \in \mathbb{R}^{n\times n}$ is the system stiffness matrix, $\mathbf{D} \in \mathbb{R}^{n\times n}$ is the proportional damping matrix, and $\boldsymbol{\tau} \in \mathbb{R}^{n\times 1}$ is the vector of external forces, and n is the number of lumped masses. Equation (2.93) represents an undamped mechanical system, and will be used further on in this section.

An implicit method forms the Newmark accelerations, velocities and displacements of (2.93), given as

$$\begin{aligned} \boldsymbol{q}_{k+1} &= \boldsymbol{q}_k + h\dot{\boldsymbol{q}}_k + \left(\frac{1}{2} - \beta_N\right) h^2\ddot{\boldsymbol{q}}_k + \beta_N h^2 \ddot{\boldsymbol{q}}_{k+1} \\ \dot{\boldsymbol{q}}_{k+1} &= \dot{\boldsymbol{q}}_k + (1-\gamma_N)h\ddot{\boldsymbol{q}}_k + \gamma_N h\ddot{\boldsymbol{q}}_{k+1} \end{aligned} \tag{2.94}$$

where the initial position $\boldsymbol{q}_k$, velocity $\dot{\boldsymbol{q}}_k$ and acceleration $\boldsymbol{q}_k$ at t_k are approximations of $\boldsymbol{q}(t_k)$, $\dot{\boldsymbol{q}}(t_k)$, and $\ddot{\boldsymbol{q}}(t_k)$, and β_N and γ_N are the Newmark algorithm parameters. Furthermore, the equations of motion of (2.93) are solved for the $t_k + h$ step

$$\mathbf{M}\ddot{\boldsymbol{q}}_{k+1} + \mathbf{D}\dot{\boldsymbol{q}}_{k+1} + \mathbf{K}\boldsymbol{q}_{k+1} = \boldsymbol{\tau}_{k+1} \tag{2.95}$$

and by inserting (2.94) into the above, we obtain the implicit equation for the accelerations as

$$\begin{aligned} &(\mathbf{M} + \gamma_N h\mathbf{D} + \beta_N h^2\mathbf{K})\ddot{\boldsymbol{q}}_{k+1} = \boldsymbol{\tau}_{k+1} \\ &-\mathbf{K}\left(\boldsymbol{q}_k + h\dot{\boldsymbol{q}}_k + \left(\frac{1}{2} - \beta_N\right)h^2\ddot{\boldsymbol{q}}_k\right) - \mathbf{D}\left(\dot{\boldsymbol{q}}_k + (1-\gamma_N)h\ddot{\boldsymbol{q}}_k\right) \end{aligned} \tag{2.96}$$

where the two right-most term on the right-hand side in the brackets are denoted the *predictor*, hence, the *corrector* equations are given as

$$\boldsymbol{q}_{k+1} = \boldsymbol{q}_k + \beta_N h^2 \ddot{\boldsymbol{q}}_{k+1} \tag{2.97}$$

$$\dot{\boldsymbol{q}}_{k+1} = \dot{\boldsymbol{q}}_k + \gamma_N h\ddot{\boldsymbol{q}}_{k+1}. \tag{2.98}$$

For a linear second-order system, the Newmark method is described as A-stable, or unconditionally stable[5] provided that the coefficients are given as [76]

$$\gamma_N \geq \frac{1}{2}, \;\; \beta_N \geq (\gamma_N + 1/2)^2/4 \tag{2.99}$$

where second-order accuracy in terms of an Trapezoidal rule [66] (which can be deduced by an implicit two-stage Runge-Kutta method [31]) is obtained by choosing and $\gamma_N = \frac{1}{2}$ and $\beta_N = \frac{1}{4}$.

The displacements, velocities and accelerations can be expressed in an incremental form as

$$\boldsymbol{q}_{k+1} = \boldsymbol{q}_k + \Delta\boldsymbol{q}_k, \;\; \dot{\boldsymbol{q}}_{k+1} = \dot{\boldsymbol{q}}_k + \Delta\dot{\boldsymbol{q}}_k, \;\; \ddot{\boldsymbol{q}}_{k+1} = \ddot{\boldsymbol{q}}_k + \Delta\ddot{\boldsymbol{q}}_k \tag{2.100}$$

[5] See for example the analysis on a second-order linear test system in Chung and Hulbert [19], where unconditional stability relates to investigating the spectral radius $\rho(\mathbf{A}) = \max(|\lambda_1|, \ldots, |\lambda_n|)$, where λ_i are the eigenvalues of the *amplification matrix* $\mathbf{A}$.

where the increment in the forces are obtained in a similar manner, such that the incremental equations of motion are given as

$$\mathbf{M}\Delta\ddot{\boldsymbol{q}}_k + \mathbf{D}\Delta\dot{\boldsymbol{q}}_k + \mathbf{K}\Delta\boldsymbol{q}_k = \Delta\boldsymbol{\tau}_k \tag{2.101}$$

A further rewrite of (2.100) using (2.94) yields the updated displacements and velocities given as

$$\Delta\boldsymbol{q}_k = h\dot{\boldsymbol{q}}_k + \frac{1}{2}h^2\ddot{\boldsymbol{q}}_k + \beta_N h^2\Delta\ddot{\boldsymbol{q}}_k \tag{2.102}$$

$$\Delta\dot{\boldsymbol{q}}_k = h\ddot{\boldsymbol{q}}_k + h\gamma_N\Delta\ddot{\boldsymbol{q}}_k. \tag{2.103}$$

Using (2.102), the incremental accelerations are given as

$$\Delta\ddot{\boldsymbol{q}}_k = \frac{1}{\beta h^2}\Delta\boldsymbol{q}_k - \frac{1}{h\beta_N}\dot{\boldsymbol{q}}_k - \frac{1}{2\beta_N}\ddot{\boldsymbol{q}}_k \tag{2.104}$$

where the solution of the unknown incremental displacement $\Delta\boldsymbol{q}_k$ are to be obtained next. Furthermore, the incremental form of the velocities can be given by inserting (2.104) into (2.103), yielding

$$\Delta\dot{\boldsymbol{q}}_k = \frac{\gamma_N}{\beta_N h}\Delta\boldsymbol{q}_k - \frac{\gamma_N}{\beta_N}\dot{\boldsymbol{q}}_k + h\left(1 - \frac{\gamma_N}{2\beta_N}\right)\ddot{\boldsymbol{q}}_k. \tag{2.105}$$

To solve for the unknown incremental discplacement, necessary for updating the next iteration displacement, velocities and accelerations, we insert (2.104) together with (2.105) into (2.101) yielding

$$\begin{aligned}\mathbf{M}\left(\frac{1}{\beta h^2}\Delta\boldsymbol{q}_k - \frac{1}{h\beta_N}\dot{\boldsymbol{q}}_k - \frac{1}{2\beta_N}\ddot{\boldsymbol{q}}_k\right) + \\ \mathbf{D}\left(\frac{\gamma_N}{\beta_N h}\Delta\boldsymbol{q}_k - \frac{\gamma_N}{\beta_N}\dot{\boldsymbol{q}}_k + h(1 - \frac{\gamma_N}{2\beta_N})\ddot{\boldsymbol{q}}_k\right) + \mathbf{K}\Delta\boldsymbol{q}_k = \Delta\boldsymbol{\tau}_k\end{aligned} \tag{2.106}$$

and re-arranging the latter yields the set of linear weighted equations to be solved for $\Delta\boldsymbol{q}_k$, expressed as

$$\mathbf{S}_t\Delta\boldsymbol{q}_k = \Delta\tilde{\boldsymbol{\tau}}_k \tag{2.107}$$

$$\mathbf{S}_t = \frac{1}{\beta h^2}\mathbf{M} + \frac{\gamma_N}{\beta_N h}\mathbf{D} + \mathbf{K} \tag{2.108}$$

$$\Delta\tilde{\boldsymbol{\tau}}_k = \Delta\boldsymbol{\tau}_k + \left(\frac{1}{h\beta_N}\mathbf{M} + \frac{\gamma_N}{\beta_N}\mathbf{D}\right)\dot{\boldsymbol{q}}_k + \left(h(1 - \frac{\gamma_N}{2\beta_N})\mathbf{D} + \frac{1}{2\beta_N}\mathbf{M}\right)\ddot{\boldsymbol{q}}_k$$

where $\mathbf{S}_t$ denotes the iteration matrix, and after obtaining $\Delta\boldsymbol{q}_k$ the accelerations are computed from (2.104), the velocities are computed according to (2.103), and finally the states are updated to $t_k + h$ for the ith iteration by (2.100). Moreover, user defined tolerance criteria can be implemented to stop the iteration when the residual of the iteration is satisfactory.

2.5.4 The generalized-α method

Variations with a basis in the method proposed by Newmark [75] have been made to allow for controlling the numerical damping of the high-frequency modes in the systems. As such, the interest is to achieve optimal numerical dissipation effects for a vibratory system without losing accuracy. A method providing these features was proposed in Hilber et al. [50], and further generalized in Chung and Hulbert [19] where the latter method was named the Generalized-α. The α parameters are reformulations of the β_N, γ_N to control the numerical damping in the algorithm. According to Chung and Hulbert [19], the method is second-order accurate for an unconstrained system.

Two α_f and α_m parameters are introduced, and we distinguish between the Newmark parameters γ_N and β_N from Section 2.5.3 and γ_α, and β_α presented in this section. The $t_k + h$ time-step displacement and velocities from [19] are equal to (2.94), whereas the $t_k + h$ equations of motion yields

$$\mathbf{M}\ddot{\boldsymbol{q}}_{k+1}^{\alpha_m} + \mathbf{D}\dot{\boldsymbol{q}}_{k+1}^{\alpha_f} + \mathbf{K}\boldsymbol{q}_{k+1}^{\alpha_f} = \boldsymbol{\tau}(t_{k+1}^{\alpha_f}) \tag{2.109}$$

and the modified displacements, velocities and accelerations are given as

$$\ddot{\boldsymbol{q}}_{k+1}^{\alpha_m} = (1-\alpha_m)\ddot{\boldsymbol{q}}_{k+1} + \alpha_m \ddot{\boldsymbol{q}}_k \tag{2.110a}$$
$$\dot{\boldsymbol{q}}_{k+1}^{\alpha_f} = (1-\alpha_f)\ddot{\boldsymbol{q}}_{k+1} + \alpha_f \dot{\boldsymbol{q}}_k \tag{2.110b}$$
$$\boldsymbol{q}_{k+1}^{\alpha_f} = (1-\alpha_f)\boldsymbol{q}_{k+1} + \alpha_f \boldsymbol{q}_k \tag{2.110c}$$
$$t_{k+1}^{\alpha_f} = (1-\alpha_f)t_{k+1} + \alpha_f t_k \tag{2.110d}$$

and note that if choosing $\alpha_f = 0$, only the $t_k + h$ time step is accounted for; α_m is used for the inertia forces, and α_f is used for restoring, damping and external forces.

The second-order accuracy of the method is provided by setting γ_α as [19]

$$\gamma_\alpha = \frac{1}{2} - \alpha_m + \alpha_f \tag{2.111}$$

whereas unconditional linear stability for the method is achieved by [66]

$$\alpha_m \leq \alpha_f \leq \frac{1}{2} \tag{2.112}$$
$$\beta_\alpha \geq \frac{1}{4} + \frac{1}{2}(\alpha_f - \alpha_m) \tag{2.113}$$

hence, $\alpha_f = \alpha_m = 0$ reduces the Generalized-α method to the trapezoidal rule, equal to the Newmark method.

For second-order ODEs, the proposed algorithmic parameters for optimal combination of low-frequency and high-frequency dissipation in the Generalized-α method are given as

$$\alpha_m = \frac{2\rho_\infty - 1}{\rho_\infty + 1},\ \alpha_f = \frac{\rho_\infty}{\rho_\infty + 1},\ \beta_\alpha = \frac{1}{4}\left(\gamma_\alpha + \frac{1}{2}\right)^2 \tag{2.114}$$

where $\rho_\infty \in [0, 1]$ is a parameter for adjusting the amount of high-frequency dissipation [19], and γ_α is calculated according to (2.111).

A modification to the method by Chung and Hulbert [19] was proposed by Arnold and Brüls [7] for a generalized class of structural systems with non-constant mass matrices, including constrained systems. Instead of computing the weighted formulation in (2.107), the residual of (2.95) is iterated until a user-defined tolerance is met. Furthermore, this implies that dynamic equilibrium is enforced at every time-step.

An auxiliary variable $\hat{\boldsymbol{a}}$ used as an acceleration-estimate, in constrast to $\ddot{\boldsymbol{q}}_{k+1}^{\alpha_m}$, given as

$$(1 - \alpha_m)\hat{\boldsymbol{a}}_{k+1} + \alpha_m \hat{\boldsymbol{a}}_k = (1 - \alpha_f)\ddot{\boldsymbol{q}}_{k+1} + \alpha_f \ddot{\boldsymbol{q}}_k \tag{2.115}$$

which is used to update the Newmark equations in (2.94). Moreover, at the first iteration of each $t_k + h$ iteration procedure, $\ddot{\boldsymbol{q}}_{k+1} = \boldsymbol{0}$ and $\hat{\boldsymbol{a}}_k$ is given by the previous time-step iteration. Otherwise $\hat{\boldsymbol{a}}_k = \alpha_f \ddot{\boldsymbol{q}}_0$. The Newmark equations are then rewritten yielding

$$\boldsymbol{q}_{k+1} = \boldsymbol{q}_k + h\dot{\boldsymbol{q}}_{kn} + \left(\frac{1}{2} - \beta_\alpha\right) h^2 \hat{\boldsymbol{a}}_k + \beta_\alpha h^2 \hat{\boldsymbol{a}}_{k+1} \tag{2.116}$$

$$\dot{\boldsymbol{q}}_{k+1} = \dot{\boldsymbol{q}}_k + (1 - \gamma_\alpha) h\hat{\boldsymbol{a}}_k + \gamma_\alpha h \hat{\boldsymbol{a}}_{k+1} \tag{2.117}$$

Suppose that the residual of a second-order system in its general form is expressed as

$$\tilde{\boldsymbol{\tau}}(t) = \mathbf{M}(\boldsymbol{q})\ddot{\boldsymbol{q}}(t) - \boldsymbol{\tau}(\dot{\boldsymbol{q}}, \boldsymbol{q}, t) \tag{2.118}$$

where $\boldsymbol{\tau}$ can be a vector of forces and torques acting upon a system, including restoring, damping and external forces and torques. For the algorithm presented in [7], the iteration matrix S_t takes the form of

$$\mathbf{S}_t = \mathbf{M}\beta'_\alpha + \mathbf{D}_t\gamma'_\alpha + \mathbf{K}_t \tag{2.119}$$

where β' and γ' are defined as

$$\beta'_\alpha = \frac{1 - \alpha_m}{\beta_\alpha h^2 (1 - \alpha_f)}, \; \gamma'_\alpha = \frac{\gamma_\alpha}{\beta_\alpha h} \tag{2.120}$$

where it is noted that $\mathbf{S}_t$ is similar to (2.108), with the corresponding Generalized-α scaling. The iteration matrix in the Generalized-α algorithm [7] is given by the partial differentiations of the residual, yielding

$$\mathbf{D}_t = \frac{\partial \tilde{\boldsymbol{\tau}}}{\partial \dot{\boldsymbol{q}}}, \; \mathbf{K}_t = \frac{\partial \tilde{\boldsymbol{\tau}}}{\partial \boldsymbol{q}} \tag{2.121}$$

where $\mathbf{D}_t$ and $\mathbf{K}_t$ denotes the tangent damping and stiffness matrices, respectively. Again, for $\alpha_m = \alpha_f = 0$, and if (2.118) comprise of a second-order linear system, $\mathbf{S}_t$ reduces to (2.108).

2.5.5 Remarks on the presented methods

Four existing methods for numerical integration of ODEs have been presented, along with two for integration of SDEs. The first two, forward Euler and Runge-Kutta, are introductory methods commonly applied to linear and non-stiff nonlinear systems (Stiff in the sense of large magnitude difference for the system eigenvalues). These methods are implementation friendly in the sense of low complexity and additionally being derivative-free, as opposed to implicit methods. The forward Euler and Runge-Kutta method have been applied to systems such as drill string models in [38, 110], and [70] (RK4 with variable time-step). For real-time applications, fixed step methods are required as the real-time system simulation is performed in discrete time. The CPU time it takes to calculate the system states and produce the output is required to be within the time step of the simulation, hence, shorter than the wall-clock duration of a time-step [8]. Hence, if it's the case that the Euler or the RK method is numerically stable for the system, these are computationally favourable methods for real-time simulation.

To maintain the state-space dimension, the Newmark and Generalized-α methods are formulated to integrate the second-order systems directly. This is convenient, considering the structure of the drill string models can be described as second-order ODEs on the form of a scalar harmonic oscillator given as $\ddot{x}(t) + \omega_n^2 x(t) = 0$. Recall the stability definitions in Section 2.5; the harmonic oscillator eigenvalues are $\pm j\omega_n$, evidently leading to an amplification of the numerical solution using an Euler method. The Newmark and Generalized-α methods are implicit methods, requiring solving of the displacement increments at every time-step. Additionally, the Generalized-α method requires derivation of the iteration matrix, $\mathbf{S}_t$, by partial differentiation of the residual forces and torques of the system, in the worst case performed online. For a nonlinear system, this not always a trivial case. If approximations are used the equilibrium conditions during the internal iteration by balancing the forces might not be met. However, in the aspect of drilling systems, the Generalized-α showed to be comparable in terms of computational speed with a fixed-step RK4 method in [103].

Chapter 3

Contributions

The work in this thesis has presented new applications targeted for simulation & control of drilling systems. Three dynamic drill string models have been developed, and additionally, a system for automating tripping while ensuring stable wellbore parameters is proposed. The main contributions in this thesis are summarized in the following sections.

3.1 Identification and Optimal Control for Surge and Swab Pressure Reduction While Performing Offshore Drilling Operations

In this paper, an automatic drill string tripping system is proposed based on an unscented Kalman filter and nonlinear-model predictive controller (NMPC) for reducing surge and swab pressure. A stochastic differential equation (SDE) system is used to formulate the simulation model, being a discrete hybrid mechanical and hydraulic model. The hydraulic model is drawn from [41]. The frictional pressure forces in the wellbore and inside the drill-string are inherently coupled with the drill string velocity in the applied friction model.

To effectively compensate for pressure transients and achieving desired wellbore pressure profile, a supervisory control system was developed in terms of an NMPC, with state and parameter estimates supplied by an UKF. The SDE formulation is used to derive the estimator model. The estimated parameters are coupled to the nonlinear pressure forces due to friction in the annulus, hence, the UKF only assumes a quadratic flow velocity friction model. Performance of the suggested control system is shown by extensive simulations comparing three implementations for offset-free tracking of bottom-hole pressure.

3.2 Component-based Modeling and Simulation of Nonlinear Drill-String Dynamics

This work proposes a dynamic drill string model formulated in component form by Bond Graphs. Furthermore, the lumped parameter model comprises the dynamics for coupled torsional and lateral motion. The Bond Graph methodology provides a systematic method of interfacing submodels in larger system simulation applications. Compared to previous related work, the presented work yields a model comprising of assumed modes. As such, the accuracy is dictated by the number of modes included. Hence, the state-space is reduced compared to using the lumped-mass formulation for vibration analysis, and relevant system frequencies are better estimated from the input of the subsystems.

The mode shape functions are derived by solving the eigenvalue problem for a fixed-free Euler Bernoulli beam, longitudinal bar, and shaft. The paper also includes a formulation of the Lund-Grenoble friction model in terms of Bond Graph elements, coupled with the drill string component model. The drill string model presented in this work can be included in system simulation case studies.

3.3 Modeling of Drill String Dynamics in Deviated Wells for Real-time Simulation

In this work, a lumped-parameter drill string model was developed for analysing coupled transient behaviour in arbitrary three-dimensional wellbores. The wellbore is effectively a parametric curve, and the dynamics are modelled as a perturbation from the nominal wellbore configuration. Previous work and models for three-dimensional analysis and simulation tend to be complex and in many cases require Finite Element analysis to be solved numerically. The proposed model is developed by applying Kane's method based on the Newton-Euler formulation, shown to be sufficient for real-time simulation and control in robotics.

By comparing the Generalized-α method and the Runge Kutta method of order 4 (RK4), a perspective of solver accuracy and error propagation when increasing the time-step is discussed. Using RK4 as the base case, it was shown that Generalized-α is an attractive solver both in terms of simulation speed and robustness to larger time-steps. The benefit of introducing a methodology related to robotics is in the application of tools to analyse stability and establish control laws for directional drilling, as an example. Furthermore, a feature of this work is relating the topic of drill string modelling with robotic manipulators.

3.4 A Discussion on the Decoupling Assumption of Axial and Torsional Dynamics in Bit-rock Models

This paper presents a discussion on the model coupling of axial stability and lumped-parameter elements and a two-degree of freedom lumped-multi-element model for on-bottom drill string analysis. The proposed model is a generalization of the previous lumped single element drill string models being coupled with the bit-rock model from [88]. For previous lumped-parameter models, such as [9, 10], the axial stability is a special case with a single lumped element. An extension was analysed in Nandakumar and Wiercigroch [73], for the coupled axial and torsional stability with a single lumped element. The stability in these works is also discussed in terms of changing system parameters such as damping and eigenfrequency.

The work presented in [105] is a generalization of these models including coupling to the number of model elements. As such, the stability conditions downhole for higher-order models are shown to be dependent on the included number of lumped elements, together with the system parameters. The purpose of the paper is to extend the analysis of single element stability of two-degree of freedom models towards the higher-order lumped element models.

The higher-order lumped models are relevant in implementing real-time drilling models in either semi-analytical form or as ordinary differential equation systems. As such, towards the new digital field of drilling with computer assistance and control, the work in this paper contributes with a discussion of the stability of lumped element models.

3.5 Comparison of the proposed models

The work in this thesis comprises of four models being modified or extended (Paper I and IV) and two new models (Paper II and III). To compare relevant performance measures for these models, Table 3.1 gives an overview of the proposed models concerning the measures of real-time applicability, control, and implementation complexity.

Table 3.1: Overview of the evaluated characteristics for the proposed models.

Model	RTA	Control	Complexity
Paper I	Intermediate	High	Intermediate
Paper II	Low	Intermediate	High
Paper III	High	Intermediate	Intermediate
Paper IV	Intermediate	High	Low

The measures evaluated as low, intermediate or high being shown in columns two to four in Table 3.1 correspond to the following explanations:

Real-time Applicability (RTA)	here the measure of model ability to approach real-time characteristics for implementation in control systems or for parameter estimation purposes.
Control Applicability	here the measure of model applicability towards control system design and implementation.
Complexity (Implementation)	here the level of model complexity for implementation in computer simulation environment (MATLAB, Modelica, Python etc.)

Chapter 4

Concluding remarks and outlook

Each section in this chapter summarizes the conclusions for each field of study and provides suggestions for future work regarding the material presented in the four included papers.

4.1 Wellbore integrity and control

The work in [100] presented an automated tripping and wellbore pressure attenuation system based on combining an unscented Kalman filter (UKF) with a nonlinear model-predictive controller (NMPC). The longitudinal drill string motion was modeled by a lumped parameter model with one element, as input to a hydraulic model drawn from [41] modified to include choke flow. To include the uncertain nature of the wellbore dynamics and facilitate state- and parameter estimation, the dynamics were represented as a set of stochastic differential equations. Hence, average fluctuations which can be interpreted as modelling errors, or process noise are implemented. To investigate the behaviour of the stochastic system, a stochastic RK method detailed in [91] was applied.

Since the estimator was proposed to predict the nonlinear frictional pressure forces arising from fluid shear stresses, system observability was shown to be limited when mud circulation was shut off. The simulator with NMPC control for automatic tripping was analysed through three simulation studies, comparing three methods of handling offset-free tracking of pressure set-points and drill string trajectory. Including the integrated error directly into the cost function for the NMPC, as compared to using a disturbance model, showed the best results in terms of tracking. Additionally, the results of tracking pressure set-points at two locations in the wellbore were presented.

The estimator-controller system proposed in [100] applied a field-data-validated hydraulic model. However, computer experiments were only provided in this work and the cases were not replicating any realistic field data from tripping in an offshore well. This is considered future work, hence, the result and discussions provided in the paper may provide insight into optimal control design and applicability of SDEs for drilling simulators.

4.2 Dynamic modelling of drill strings

Lagrangian mechanics were used to expressing the dynamics for a drill string in a vertical wellbore in Tengesdal et al. [104]. Furthermore, this work was an extension of [102]. The equations of motion were developed by considering a spatial disc-element under torsion and using the method of assumed modes to describe the elastic deformation over the entire drill string length. Within the Bond Graph (BG) framework, the equations of motion were structured using vector BG elements to form a component model of the drill string. The BG elements were defined from the Lagrangian, comprising momentum and generalized velocities as state variables. Hence, the model is reformulated to a first-order form particularly useful for numerical simulation.

The model included dynamics governed by lateral bending, longitudinal motion, and torsional deformation. Features considering coupled torsional and lateral vibrations were analysed by model reduction and in terms of simulator performance. The results from [102] were revised and extended to also include a study on applied friction at the bit by including the LuGre friction model. It was assumed that the cross-section was uniform along the length of the drill string. The implication of this is that isolated studies on configurations only including drill pipes or a BHA are available in this model.

Further work regarding this model should allow for at least the coupling of two different sections on the shaft, to be able to include BHA in analyzing realistic drill string configurations. It is also suggested to include a realistic friction model illustrating the on-bottom drilling process. Hence, further studies can be based on the work in Detournay et al. [27] for the deterministic case. Moreover, it can be interesting to expand the model into a stochastic system due to the uncertainty of the drilling process (see, e.g., the work by Ritto et al. [89, 90]). It is worthwhile to mention that the work in [104] may not be limited to oil & gas drilling, hence, implementation to study the twisting of shafts in machinery system can be a relevant application.

4.2.1 Dynamics in directional wells

Based on both the formulation of a rigid and elastic body in space used in [104] and the lumped-multi-element model presented in [105], the last paper introduced a link between the robotic framework of describing manipulator systems and drill strings. In Tengesdal et al. [103], Kane's method was used to propose a lumped multi-element drill string model suitable for directional well configurations confined to parametric curves. Moreover, having established the desired trajectory of an offshore or onshore well, the dynamics of the drill string being "placed" onto it is readily formulated.

Unlike formulating the system energy to derive the equation of motion, Kane's method is based on the Newton-Euler formulation. The forces of constraint are eliminated by using the principle of virtual work, which is formulated by the quantities known as partial velocities. These are in turn used to direct the inertia and external forces and torques in the direction of the generalized speeds selected for the system, which have no direction and only a magnitude. The generalized speeds can be a linear combination of, or just selected equal to, the system

generalized velocities, as was done for the drill string system [103]. In the latter, the model equations could have equally been obtained by the Lagrangian, as was done in [104]. However, the number of coupling terms for multiple-element systems being interconnected can increase by deriving the equations of motion using the system energy and partial differential equations in the Lagrangian. In some cases, the magnitude of these are small, and could only lead to increased computational demand [59].

The real-time characteristics of the model and numerical solver were compared with a Generalized-α method and an RK4 method, investigating the error of the Euclidean norm of the bit trajectory. Numerical stability was shown to be dictated by the contact stiffness in the model. From the applied input sequence at the rig-block, it was seen that the Generalized-α solver was robust to larger time-steps, and in a similar range for simulation time as the RK4. The RK4 diverged for time-steps larger than 10^{-2}, exceeding its numerical stability limit.

Due to space limitations in the paper (and time limitations for the doctoral studies), future work should be performed to expand the wellbore curve while performing a numerical simulation. This could provide an interesting feature during online simulation of the model in parallel with drilling operations, to predict behaviour in new well segments in future time. An extended simulator study could also bring to evidence an optimal model-solver configuration suitable for implementation in practical scenarios.

4.3 Stability for lumped multi-element drill string models

The work in Tengesdal et al. [105] provided a formulation and stability analysis of a higher-order lumped-parameter drill string model coupled with a bit-rock interaction model. Properties of the off-bottom models presented in Hovda [52, 53] were used and extended to the on-bottom case described by ODEs. The drill string was modelled as a series of alternating springs and point masses. The analysis has its basis in the bit-rock model from the work in Richard et al. [88] and relates to previous work in Besselink et al. [9], and [26, 73] using single lumped-element models. As such, [105] extends this to lumped-multi-element models, and stability on behalf of decoupling the axial and torsional model is discussed.

By incorporating the bit-rock model from [88], the system described in brought to a state-dependent delay differential equation form with a time-delay term, dictating the stability of the system. It is proposed in [105] that the decoupled generalized system stability indicates that the stable region is reduced with an increased number of lumped model elements, and trends towards zero. Furthermore, it was concluded from the analysis on the model that including the nonlinear coupling in axial and torsional dynamics when discussing the stability of operating points would be advisable. Finally, a simulation of two wellbore configurations is presented with a stability map when including a BHA.

Validation of model stability boundary towards vibration measurements during drilling should be performed. Isolating the field data from axial and torsional motion may be one approach for comparison. However, as the vibrations are coupled, extending the analysis to a three-

dimensional model with lateral motion (as discussed in [105]) might be a better option before experimental validation is performed. Furthermore, future work can be to extend the stability analysis to the model proposed in [103] included in this thesis.

4.4 General outlook

The work presented in this thesis is mainly based on simulation to analyse system behaviour. The largest part of the thesis work has been devoted to establishing the modelling framework and development of the models. Applicable to all the work in this thesis is model verification, in the sense of efficient implementation in software such as MATLAB, Python or Modelica based tools, benchmarking with acknowledged models in the literature, and validation of the model behaviour compared to what is observed in the field. These topics should be of main concern in future work on the subject.

A final note is on the topic of control for the proposed drill string models. Except for the model predictive controller proposed for the combined hydraulic and mechanical model in [100], the models have been analysed with the proportional-integral-derivative (PID) controller, in form of supplying the torque input to the drill string. It would be interesting to proceed with control law design, specifically for [105] and [103], including designing laws with increased capabilities of damping excessive vibrations during drilling.

References

[1] B. S. Aadnøy, M. Fazaelizadeh, and G. Hareland. A 3D analytical model for wellbore friction. *Journal of Canadian Petroleum Technology*, 49:25–36, 2010.

[2] T. Aarrestad, H. Tønnesen, and Å. Kyllingstad. Drillstring Vibrations: Comparison Between Theory and Experiments on a Full-Scale Research Drilling Rig. In *SPE/IADC Drilling Conference and Exhibition*, 02 1986. SPE-14760-MS.

[3] U. J. F. Aarsnes and R. J. Shor. Torsional vibrations with bit off bottom: Modeling, characterization and field data validation. *Journal of Petroleum Science and Engineering*, 163:712–721, 2017.

[4] U. J. F. Aarsnes and N. van de Wouw. Dynamics of a distributed drill string system: Characteristic parameters and stability maps. *Journal of Sound and Vibration*, 417:376–412, 2018.

[5] O. Akimov, A. Hohl, H. Oueslati, H. Reckmann, and B. Hughes. Evolution of drilling dynamics measurement systems. *Proceedings of the SPE/IADC Middle East Drilling Technology Conference and Exhibition*, pages 29–31, 2018.

[6] B. Armstrong-Helouvry. Stick-slip arising from stribeck friction. In *Proceedings., IEEE International Conference on Robotics and Automation*, pages 1377–1382. IEEE, 1990.

[7] M. Arnold and O. Brüls. Convergence of the generalized-α scheme for constrained mechanical systems. *Multibody System Dynamics*, 18:185–202, 2007.

[8] J. Bélanger, P. Venne, and J.-N. Paquin. The what, where and why of real-time simulation. *Planet Rt*, 1(1):25–29, 2010.

[9] B. Besselink, N. van de Wouw, and H. Nijmeijer. A semi-analytical study of stick-slip oscillations in drilling systems. *Journal of Computational and Nonlinear Dynamics*, 6, 2011. ISSN 1.

[10] B. Besselink, T. Vromen, N. Kremers, and N. van de Wouw. Analysis and control of stick-slip oscillations in drilling systems. *IEEE Transactions on Control Systems Technology*, 24:1582–1593, 2016.

[11] Ø. Breyholtz, G. Nygaard, H. Siahaan, and M. Nikolaou. Spe 128151 managed pressure drilling : A multi-level control approach. *SPE Intelligent Energy Conference and Exhibition*, 2010.

[12] R. G. Brown and P. Y. C. Hwang. *Introduction to Random signals and Applied Kalman Filtering with MATLAB exercises*. Wiley, 4th edition, 2012. ISBN 978-0470609699.

[13] P. M. Burrage. Runge-kutta methods for stochastic differential equations. 1999.

[14] T. Butlin and R. S. Langley. An efficient model of drillstring dynamics. *Journal of Sound and Vibration*, 356:100–123, 2015.

[15] E. Cayeux. On the importance of boundary conditions for real-time transient drill-string mechanical estimations. *IADC/SPE Drilling Conference and Exhibition*, 2018.

[16] E. Cayeux, B. Daireaux, and E. W. Dvergsnes. Automation of drawworks and topdrive management to minimize swab/surge and poor-downhole-condition effects. *IADC/SPE Drilling Conference and Exhibition*, 26:557–568, 2010.

[17] G. S. Chirikjian. *Stochastic Models Information Theory and Lie Groups, Volume 1: Classical Results and Geometric Methods*. Springer Science & Business Media, 2009. ISBN 978-0-8176-4943-2.

[18] A. P. Christoforou and A. S. Yigit. Fully coupled vibrations of actively controlled drillstrings. *Journal of Sound and Vibration*, 267:1029–1045, 2003.

[19] J. Chung and G. M. Hulbert. A time integration algorithm for structural dynamics with improved numerical dissipation: The generalized-α method. *Journal of Applied Mechanics, Transactions ASME*, 60:371–375, 1993.

[20] G. Clauss, E. Lehmann, and C. Östergaard. Features of offshore structures. In *Offshore Structures*, pages 25–143. Springer, 1992.

[21] R. Dadfar, S. Velut, P.-O. Larsson, M. Strandberg, H. Runvik, J. Wíndahl, P. Kittilsen, J.-M. Godhavn, and Å. Hjulstad. Drilling library: A modelica library for the simulation of well construction. *Proceedings of The American Modelica Conference 2018, October 9-10, Somberg Conference Center, Cambridge MA, USA*, 154:246–253, 2019.

[22] L. J. Danforth. Environmental constraints on drill rig configurations. *Marine Technology and SNAME News*, 14(3):244–264, 1997.

[23] D. Dareing, J. Tlusty, and C. Zamudio. Self-excited vibrations induced by drag bits. *Journal of Energy Resources Technology, Transactions of the ASME*, 112:54–61, 1990.

[24] C. C. de Wit, H. Olsson, K. Astrom, and P. Lischinsky. A new model for control of systems with friction. *IEEE Transactions on Automatic Control*, 40:419–425, 1995.

[25] C. C. de Wit, F. R. Rubio, and M. A. Corchero. D-oskil: A new mechanism for controlling stick-slip oscillations in oil well drillstrings. *IEEE Transactions on Control Systems Technology*, 16:1177–1191, 2008.

[26] A. Depouhon and E. Detournay. Instability regimes and self-excited vibrations in deep drilling systems. *Journal of Sound and Vibration*, 333:2019–2039, 2014.

[27] E. Detournay, T. Richard, and M. Shepherd. Drilling response of drag bits: Theory and experiment. *International Journal of Rock Mechanics and Mining Sciences*, 45:1347–1360, 2008.

[28] DNV-GL. Oil and gas forecast to 2050: Energy transition outlook. Technical report, DNV GL - Oil & gas, 2017.

[29] G. C. Downton. Challenges of modeling drilling systems for the purposes of automation and control. *IFAC Proceedings Volumes (IFAC-PapersOnline)*, 1:201–210, 2012. 1st IFAC Workshop on Automatic Control in Offshore Oil and Gas Production.

[30] A. N. Eaton, L. D. R. Beal, S. D. Thorpe, E. H. Janis, C. Hubbell, J. D. Hedengren, R. Nybø, M. Aghito, K. Bjørkevoll, R. E. Boubsi, J. Braaksma, and G. van Og. Ensemble model predictive control for robust automated managed pressure drilling. *SPE Annual Technical Conference and Exhibition*, pages 1–16, 2015.

[31] O. Egeland and J. T. Gravdahl. *Modeling and Simulation for Automatic Control*, volume 76. Marine Cybernetics Trondheim, Norway, 2002. ISBN 9788292356012.

[32] M. A. Elsayed, D. W. Dareing, and C. A. Dupuy. Effect of downhole assembly and polycrystalline diamond compact (pdc) bit geometry on stability of drillstrings. *Journal of Energy Resources Technology*, 119:159, 1997.

[33] T. Feng, M. Vadali, Z. Ma, D. Chen, and J. Dykstra. A finite element method with full bit-force modeling to analyze drillstring vibration. *Journal of Dynamic Systems, Measurement, and Control*, 139:1–10, 9 2017.

[34] R. Findeisen and F. Allgoewer. An introduction to nonlinear model predictive control. *Control, 21st Benelux Meeting on Systems and Control*, pages 1–23, 2002.

[35] F. Florence and F. Iversen. Real-time models for drilling process automation: Equations and applications. *SPE/IADC Drilling Conference, Proceedings*, 2:1218–1233, 2010.

[36] R. Foster and R. Macmillan. High speed telemetry on wired drill pipe, history, and impact on drilling process. In *Offshore Technology Conference*, OTC-28735-MS, 2018.

[37] P. Fritzson. *Principles of object-oriented modeling and simulation with Modelica 3.3: a cyber-physical approach*. John Wiley & Sons, 2014.

[38] C. Germay, V. Denoël, and E. Detournay. Multiple mode analysis of the self-excited vibrations of rotary drilling systems. *Journal of Sound and Vibration*, 325:362–381, 2009.

[39] A. Ghasemloonia, D. G. Rideout, and S. D. Butt. A review of drillstring vibration modeling and suppression methods. *Journal of Petroleum Science and Engineering*, 131: 150–164, 2015.

[40] H. Gilsing and T. Shardlow. Sdelab: A package for solving stochastic differential equations in matlab. *Journal of Computational and Applied Mathematics*, 205:1002–1018, 2007. ISSN 03770427. doi: 10.1016/j.cam.2006.05.037.

[41] K. Gjerstad, R. W. Time, and K. S. Bjorkevoll. A medium-order flow model for dynamic pressure surges in tripping operations. *SPE/IADC Drilling Conference*, 2013.

[42] K. Gjerstad, R. W. Time, et al. Simplified explicit flow equations for herschel-bulkley fluids in couette-poiseuille flow — for real-time surge and swab modeling in drilling. *SPE Journal*, 20(03), 2015.

[43] J.-M. Godhavn. Control requirements for high-end automatic mpd operations. *SPE/IADC Drilling Conference and Exhibition*, 25:336–345, 2009.

[44] H. E. Goicoechea, F. S. Buezas, and M. B. Rosales. A non-linear cosserat rod model for drill-string dynamics in arbitrary borehole geometries with contact and friction. *International Journal of Mechanical Sciences*, 157-158:98–110, 2019.

[45] L. Grune and J. Pannek. *Nonlinear Model Predictive Control: Theory and Algorithms*. Springer, 2011. ISBN 9780857295002.

[46] K. Gu, L. V. Kharitonov, and J. Chen. *Stability of Time-Delay Systems*. Springer Science & Business Media, 2003. ISBN 9781461265849.

[47] D. A. Haessig and B. Friedland. On the modeling and simulation of friction. *Journal of Dynamic Systems, Measurement and Control, Transactions of the ASME*, 113:354–362, 1991.

[48] E. Hairer and G. Wanner. *Solving Ordinary Differential Equations II Stiff and Differential-Algebraic Problems*. Springer, 2nd edition, 2002. ISBN 9783642052200.

[49] D. J. Higham. An algorithmic introduction to numerical simulation of stochastic differential equations. *SIAM Review*, 43:525–546, 2005. ISSN 0036-1445. doi: 10.1137/s0036144500378302.

[50] H. M. Hilber, T. J. Hughes, and R. L. Taylor. Improved numerical dissipation for time integration algorithms in structural dynamics. *Earthquake Engineering & Structural Dynamics*, 5(3):283–292, 1977.

[51] S. Hovda. Semi-analytical model of the axial movements of an oil-well drillstring in vertical wellbores. *Journal of Sound and Vibration*, 433:287–298, 2018.

[52] S. Hovda. Semi-analytical model of the axial movements of an oil-well drillstring in deviated wellbores. *Journal of Sound and Vibration*, 433:287–298, 2018.

[53] S. Hovda. Automatic detection of abnormal torque while reaming. *Journal of Petroleum Science and Engineering*, 166:13–24, 2018.

[54] F. Iversen, E. Cayeux, E. W. Dvergsnes, J. Gravdal, E. H. Vefring, B. Mykletun, A. Torsvoll, S. Omdal, and A. Merlo. Monitoring and Control of Drilling Utilizing Continuously Updated Process Models. In *IADC/SPE Drilling Conference*. OnePetro, 2006. SPE-99207-MS.

[55] F. Iversen, E. Cayeux, E. W. Dvergsnes, R. Ervik, M. Welmer, and M. K. Balov. Offshore field test of a new system for model integrated closed-loop drilling control. *SPE Drilling and Completion*, 24:518–530, 2009.

[56] B. Jacobson. The stribeck memorial lecture. *Tribology International*, 36:781–789, 2003.

[57] G.-O. Kaasa, Ø. N. Stamnes, O. M. Aamo, and L. Imsland. Simplified hydraulics model used for intelligent estimation of downhole pressure for a managed-pressure-drilling control system. *SPE Drilling & Completion*, 27, 2012.

[58] R. E. Kalman. A new approach to linear filtering and prediction problems. *Transactions of the ASME. Journal of Basic Engineering*, 82:35–45, 1960.

[59] T. R. Kane and D. A. Levinson. Formulation of equations of motion for complex spacecraft. *Journal of Guidance and control*, 3(2):99–112, 1980.

[60] D. C. Karnopp. Computer simulation of stick-slip friction in mechanical dynamic systems. *Transactions of the ASME. Journal of Dynamic Systems, Measurement and Control*, 107:100–103, 1985.

[61] D. C. Karnopp, D. L. Margolis, and R. C. Rosenberg. *System dynamics: modeling, simulation, and control of mechatronic systems*. John Wiley & Sons, 2012.

[62] H. K. Khalil. Nonlinear systems. *Prentice-Hall, New Jersey*, 2:1–5, 1996.

[63] Y. A. Khulief and H. Al-Naser. Finite element dynamic analysis of drillstrings. *Finite Elements in Analysis and Design*, 41:1270–1288, 2005.

[64] R. Kikuuwe, N. Takesue, A. Sano, H. Mochiyama, and H. Fujimoto. Fixed-step friction simulation: from classical coulomb model to modern continuous models. In *2005 IEEE/RSJ International Conference on Intelligent Robots and Systems*, pages 1009–1016, 2005.

[65] R. I. Leine, D. H. V. Campen, A. D. Kraker, and L. V. D. Steen. Stick-slip vibrations induced by alternate friction models. *Nonlinear Dynamics*, 16:41–54, 1998.

[66] C. Lunk and B. Simeon. Solving constrained mechanical systems by the family of newmark and α-methods. *ZAMM - Journal of Applied Mathematics and Mechanics / Zeitschrift für Angewandte Mathematik und Mechanik*, 86(10):772–784, 2006.

[67] W. Lyons, G. B. P. J, and M. Lorenz. *Standard Handbook of Petroleum e Natural Gas Engineering*. Gulf Professional Publishing, 3rd edition, 2015. ISBN 978-0123838469.

[68] D. L. Margolis and D. C. Karnopp. Bond graphs for flexible multibody systems. *Journal of Dynamic Systems, Measurement, and Control*, 101:50, 1979.

[69] L. Meirovitch. *Analytical Methods In Vibrations*. Mecmillan Company London, 1967.

[70] H. Melakhessou, A. Berlioz, and G. Ferraris. A nonlinear well-drillstring interaction model. *Journal of Vibration and Acoustics*, 125:46, 2003. ISSN 07393717.

[71] S. A. Mirhaj, E. Kaarstad, and B. S. Aadnøy. Torque and drag modeling; soft-string versus stiff-string models. *Proceedings of the SPE/IADC Middle East Drilling Technology Conference and Exhibition*, pages 26–28, 2016.

[72] N. Mostaghel and T. Davis. Representations of coulomb friction for dynamic analysis. *Earthquake Engineering and Structural Dynamics*, 26:541–548, 1997.

[73] K. Nandakumar and M. Wiercigroch. Stability analysis of a state dependent delayed, coupled two dof model of drill-stringvibration. *Journal of Sound and Vibration*, 332: 2575–2592, 2013.

[74] E. Navarro-Lopez and R. Suarez. Practical approach to modelling and controlling stick-slip oscillations in oilwell drillstrings. *Proceedings of the 2004 IEEE International Conference on Control Applications, 2004.*, 2:1454–1460, 2004.

[75] M. N. Newmark. A method of computation for structural dynamics. *Journal of the Engineering Mechanics Division*, 85:64–94, 1959.

[76] G. Noh and K.-J. Bathe. For direct time integrations: A comparison of the Newmark and ρ_∞-Bathe schemes. *Computers and Structures*, 225, 2019.

[77] V. Nygaard, M. Jahangir, T. Gravem, E. Nathan, J. G. Evans, M. Reeves, H. Wolter, S. Hovda, et al. A step change in total system approach through wired drillpipe technology. In *IADC/SPE Drilling Conference*. Society of Petroleum Engineers, 2008.

[78] Offshore Technology. Turning on the taps: inside Norway's new oil and gas taxes, 2021. URL https://www.offshore-technology.com/features/turning-on-the-taps-inside-norways-new-oil-and-gas-taxes. (Accessed: 04.05.2021).

[79] OG21. The oil & gas for the 21st century: Strategy document. Online, 2016. URL https://www.og21.no/en/strategy-and-analyses/the-og21-strategy/.

[80] H. Olsson, K. J. Åstrøm, C. C. D. Wit, M. Gãfvert, and P. Lischinsky. Friction models and friction compensation. *European Journal of Control*, 4:176–195, 1998.

[81] E. Pennestrì, V. Rossi, P. Salvini, and P. P. Valentini. Review and comparison of dry friction force models. *Nonlinear Dynamics*, 83:1785–1801, 2016.

[82] T. Pink, W. Koederitz, A. Barrie, D. Bert, and D. Overgaard. Closed loop automation of downhole weight on bit improves sliding performance and reduces conservatism in unconventional horizontal well development. *Proceedings - SPE Annual Technical Conference and Exhibition*, 5:4092–4105, 2013.

[83] S. J. Qin and T. A. Badgwell. A survey of industrial model predictive control technology. *Control Engineering Practice*, 11:733–764, 2003.

[84] S. S. Rao. *Vibration of Continuous Systems*. John Wiley & Sons, 2007. ISBN 0471771716.

[85] F. F. Real, A. Batou, T. G. Ritto, C. Desceliers, and R. R. Aguiar. Hysteretic bit/rock interaction model to analyze the torsional dynamics of a drill string. *Mechanical Systems and Signal Processing*, 111:222–233, 2018.

[86] M. Reeves, J. D. MacPherson, R. Zaeper, D. R. Bert, J. Shursen, W. K. Armagost, D. S. Pixton, and M. Hernandez. High Speed Drill String Telemetry Network Enables New Real Time Drilling and Measurement Technologies. In *SPE/IADC Drilling Conference and Exhibition*, 02 2006. SPE-99134-MS.

[87] E. Reiten, M. Ognedal, M. Berdal, G. Brækken, K. Færøyvik, T. Holm, J. Jacobsen, J. Korsgaard, W. Nistad, B. Nyland, and D. Omre. Økt bore og brønnaktiviteter på norsk sokkel. Technical report, Olje- og Energidepartementet, 2012.

[88] T. Richard, C. Germay, and E. Detournay. A simplified model to explore the root cause of stick-slip vibrations in drilling systems with drag bits. *Journal of Sound and Vibration*, 305:432–456, 2007.

[89] T. G. Ritto, C. Soize, and R. Sampaio. Non-linear dynamics of a drill-string with uncertain model of the bit-rock interaction. *International Journal of Non-Linear Mechanics*, 44: 865–876, 2009.

[90] T. G. Ritto, R. R. Aguiar, and S. Hbaieb. Validation of a drill string dynamical model and torsional stability. *Meccanica*, 52:2959–2967, 2017.

[91] A. Rößler. Runge-kutta methods for itô stochastic differential equations with scalar noise. *BIT Numerical Mathematics*, 46:97–110, 2006.

[92] A. Rößler. Runge–kutta methods for the strong approximation of solutions of stochastic differential equations. *SIAM Journal on Numerical Analysis*, 48(3):922–952, 2010.

[93] B. Saldivar, S. Mondié, S. I. Niculescu, H. Mounier, and I. Boussaada. A control oriented guided tour in oilwell drilling vibration modeling. *Annual Reviews in Control*, 42:100–113, 2016.

[94] M. Sarker, D. G. Rideout, and S. D. Butt. Dynamic model for 3d motions of a horizontal oilwell bha with wellbore stick-slip whirl interaction. *Journal of Petroleum Science and Engineering*, 157:482–506, 2017.

[95] R. J. Shor, M. Pryor, and E. van Oort. Drillstring Vibration Observation, Modeling and Prevention in the Oil and Gas Industry. In *Dynamic Systems and Control Conference*, volume 3, 10 2014.

[96] R. Sipahi. *Mastering Frequency Domain Techniques for the Stability Analysis of LTI Time Delay Systems*. SIAM, 2019. ISBN 978-1-611975-71-0.

[97] P. Skalle. *Drilling Fluid Engineering*. Ventus Publishing ApS, 2011. ISBN 978-87-7681-929-3.

[98] T. Specker, M. Buchholz, and K. Dietmayer. A new approach of dynamic friction modelling for simulation and observation. *IFAC Proceedings Volumes (IFAC-PapersOnline)*, 47(3):4523–4528, 2014.

[99] S. Strøm, M. K. Balov, H. Kjørholt, R. Gaasø, E. Vefring, and R. Rommetveit. The future drilling scenario. *Offshore Technology Conference*, 2008.

[100] N. Tengesdal and C. Holden. Identification and optimal control for surge and swab pressure reduction while performing offshore drilling operations. *Modeling, Identification and Control*, 41(3):165–184, 2020.

[101] N. Tengesdal, T. T. Kristoffersen, and C. Holden. Applied nonlinear compressor control with gain scheduling and state estimation. *IFAC-PapersOnLine*, 51:151–157, 2018.

[102] N. Tengesdal, C. Holden, and E. Pedersen. Component-based modeling and simulation of nonlinear drill-string dynamics. In *ASME 2019 38th International Conference on Ocean, Offshore and Arctic Engineering*. American Society of Mechanical Engineers Digital Collection, 2019.

[103] N. K. Tengesdal, G. Fotland, C. Holden, and B. Haugen. Modeling of drill string dynamics in deviated wells for real-time simulation (submitted). *SIMULATION: Transactions of the Society for Modeling and Simulation International*, 2021.

[104] N. K. Tengesdal, C. Holden, and E. Pedersen. Component-based modeling and simulation of nonlinear drill-string dynamics (submitted). *Journal of Offshore Mechanics and Arctic Engineering*, 2021.

[105] N. K. Tengesdal, S. Hovda, and C. Holden. A discussion on the decoupling assumption of axial and torsional dynamics in bit-rock models. *Journal of Petroleum Science and Engineering*, 202, 2021.

[106] T. Vromen, C. hing Dai, N. V. D. Wouw, T. Oomen, P. Astrid, A. Doris, and H. Nijmeijer. Mitigation of torsional vibrations in drilling systems : A robust control approach. *IEEE Transactions on Control Systems Technology*, pages 1–17, 2017.

[107] C. Wang and R. Tucker. An integrated model for drill-string dynamics. *Journal of Sound and Vibration*, 224:123–165, 1999.

[108] B. M. L. William Lyons, Gary Plisga. *Standard Handbook of Petroleum and Natural Gas Engineering*. Gulf Professional Publishing, 3rd edition, 2015. ISBN 9780123838469.

[109] D. Zhao and S. Sangesland. Down hole pressure variation due to axial stick slip motion effect on drill string. *SPE Production and Operations Symposium, Proceedings*, 2015-Janua:396–407, 2015.

[110] D. Zhao, S. Hovda, and S. Sangesland. Abnormal down hole pressure variation by axial stick-slip of drillstring. *Journal of Petroleum Science and Engineering*, 145:194–204, 2016.

Papers

Paper I

Identification and Optimal Control for Surge and Swab Pressure Reduction While Performing Offshore Drilling Operations

N. K. Tengesdal and C. Holden.
Identification and Optimal Control for Surge and Swab Pressure Reduction While Performing Offshore Drilling Operations
2020, Modeling, Identification and Control (MIC), Vol. 41, No. 3, pp. 165-184

Errata

In Section 4.2, page 174, 4th paragraph: The applied integration method was mentioned to be the Runge-Kutta Maruyama order 4 from [91]. This was incorrect. The correct description of the method applied in the paper is a 3rd order Stochastic Runge Kutta (SRK) method *RI1W1*, with convergence of order 2, from [91].

Modeling, Identification and Control, Vol. 41, No. 3, 2020, pp. 165–184, ISSN 1890–1328

Identification and Optimal Control for Surge and Swab Pressure Reduction While Performing Offshore Drilling Operations

Njål K. Tengesdal [1] Christian Holden [1]

[1] *Department of Mechanical and Industrial Engineering, Norwegian University of Science and Technology, N-7491 Trondheim, Norway. E-mail:* {njaal.tengesdal,christian.holden}@ntnu.no

Abstract

In this paper, an unscented Kalman filter (UKF) coupled with a nonlinear model-predictive controller (NMPC) for a hydraulic wellbore model with multi-variable control and tracking is presented. In a wellbore, high drill string velocities in operational sequences such as tripping might result in surge and swab pressures in the annular section of the wellbore. To overcome these challenges, a controller incorporating safety and actuator limits should be used. A second-order model is used to predict axial drill string velocity downhole. With a NMPC specifying the block position trajectory, choke flow reference, desired back-pressure pump flowrate and stand-pipe pressure, we can automatically supervise and control the pressure in the wellbore. To compensate for unmeasured states, an estimator is designed to predict the frictional pressure forces in the wellbore and filter noisy measurements. A stochastic approach for the hydraulic model is taken, including variance of the average fluctuations for the flow and pressure states. Comparing three NMPC configurations, the result of using an integration of the tracking error in the prediction model gave best offset-free tracking of the bottom-hole pressure. The controller compensates for the unknown fluctuations, and is shown to be robust towards model mismatch. Including the mechanical system in the NMPC prediction model, we can effectively constrain the predicted axial drill string velocity to reduce the pressure oscillations and achieve tracking of bottom hole pressure and choke differential pressure. The outcome is shown through extensive simulations to be an effective control strategy, reducing the pressure spikes while tripping.

Keywords: Offshore-drilling, Nonlinear Estimation, MPC, Nonlinear Control, Offset-free control

1 Introduction

Drilling an offshore well is comprised of sequences to be executed in a safe and efficient manner to reduce pressure fluctuations in the wellbore. Tripping, either running-in or running-out sections of drill string (DS) pipe, are done to extend or shorten the DS assembly while drilling a well. In these operations, typically the cost due to time is larger than the production costs, requiring the highest rate-of-penetration possible. Furthermore, increasing tripping speed might lead to instability in the wellbore known as surge, and swab pressures occurring in the annular section (Rasmussen and Sangesland, 2007; Lyons et al., 2015). An offshore drilling process is illustrated in Figure 1.

Automatic pressure control is a measure of stabilizing the transient pressure in the wellbore. Implemented in the process control of the drilling-rig, the conventional Proportional-Integral-Derivative (PID) controller is used to control the subsea or top-side choke valve, creating a back-pressure in the well to effectively control the bottom hole pressure (BHP)

doi:10.4173/mic.2020.3.3

(Gravdal et al., 2018). However, as pointed out in Gravdal et al. (2018), changing conditions in the wellbore due to well geometry, open-hole sections, formation and fluid properties, along with changing temperature profile along the well can limit the PID controller in terms of required re-tuning during the operations. These quantities are in many cases dependent on the movement of the DS, and it is emphasized that the control law should oppose limitations on the mechanical side of the drilling operation (Cayeux et al., 2014). Application of automatic control to obtain reference tracking of the bottom-hole pressure (BHP) with tight pressure margins is commonly referred to as Managed Pressure Drilling (MPD). On the other hand, for wider margins the fluid density is typically adjusted to maintain desired well pressure (Nygaard et al., 2007b).

The challenges of maintaining a stable wellbore are connected to the reliability of the measurement data and the physical model used for real-time wellbore state prediction (Cayeux et al., 2014). Sensors used for well control are mud-pulse telemetry, wired drill-pipe transmitting pressure measurements to the surface, and the gyro in the bottom-hole assembly (BHA). Mud-pulse is restricted to cases where sufficient flow is maintained. Currently, drilling-rigs are equipped with higher fidelity sensor packages, such that more advanced control systems can be utilized (Cayeux et al., 2010). As such, a broad research field on soft sensors is available in terms of observer-based applications (e.g Stamnes et al. (2008)) and the use of Kalman filters (KF) (e.g. Nygaard et al. (2006); Gravdal et al. (2010)). Filtering techniques are methods to provide additional insight, parameter estimates of unobserved process variables with minimum variance and bring redundancy in the measurement data.

Control design in MPD applications traditionally restrict to the use of the choke valve (Meglio and Aarsnes, 2015). The choke valve is the variable restriction in the mud return flow from the annulus. A rotating circulation device is included at the top of the well to seal off the annulus between the DS and borehole wall (Downton, 2012). However, an advantage is to combine the choke with the mud circulation system and draw works to further increase the capabilities when tight pressure margins are present and longer reach wells are drilled (Godhavn, 2009). In terms of choke control, see for example Nygaard et al. (2007a); Stakvik et al. (2016); Zhou (2018).

In multi-variable control, a supervisory control system is included to set reference points to sub-level controllers (typically PID) directly actuating valves, pumps, etc. In MPD applications for controlling pressures at defined locations, model-based schemes are commonly applied. Typically, a first-order model comprised of ordinary differential equations is sufficient for capturing the transient pressure and flow effects (Kaasa et al., 2012; Gjerstad et al., 2013).

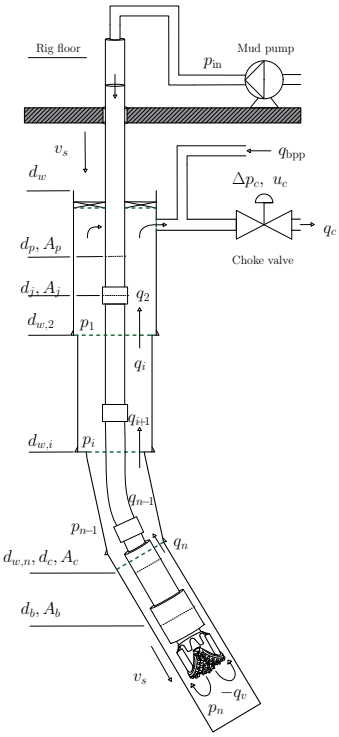

Figure 1: A sketch of an offshore drilling operation. The variable v_s denotes the tripping speed. Green dashed lines mark the boundary of each segment in the model.

Linear model-based control schemes have been studied extensively in Nygaard et al. (2007b); Breyholtz and Nygaard (2009); Breyholtz et al. (2010) and Møgster et al. (2013). The latter utilizes the WeMod high fidelity well simulator with Equinor's SEPTIC Model Predicitive Control (MPC) software. In these studies, the DS velocity is manipulated directly.

In terms of nonlinear multi-variable control, the nonlinear MPC is using a nonlinear model to calculate the process inputs. A comparsion between a PI controller and a NMPC using a low-order model is given in Breyholtz et al. (2009), were the control design was additionally tested on a high-fidelity dynamic model used in offshore drilling. In Pedersen et al. (2018), choke pressure, pump flow and the separator are controlled to achieve multi-objective control with no DS dynamics. The work considers underbalanced drilling

which is a variant of the MPD, allowing reservoir production during drilling. The work of Nandan and Imtiaz (2017) includes an NMPC for switching between tracking of BHP and kick-attenuation in the wellbore, showing promising results by using the choke valve for control when performing pipe connections.

In this paper, we combine both the mechanical and fluid domains by means of a hoisting model for the axial DS dynamics, along with a first-order lumped parameter model with first-principles mud flow dynamics from Gjerstad et al. (2013). The frictional pressure forces in the wellbore and inside DS are inherently coupled with the DS velocity in this model. To effectively compensate for pressure transients and achieving desired wellbore conditions, we develop a supervisory control system in terms of a NMPC, with state and parameter estimates supplied by an UKF. We assume sparse knowledge of the frictional pressure forces in the annulus, and show the performance of the suggested control strategy through extensive simulations.

The rest of the paper is organized as follows: Section 2 gives the preliminaries of the methods and theory used in this paper. Section 3 gives an overview of the hydraulic wellbore model which is extended with dynamics of the hoisting system. Section 4 includes a survey on the aspect of system identification for the wellbore when the flow is limited through the bit nozzle, the estimator design and a test case. Section 5 presents the control design, with nonlinear model-predictive control. Section 6 shows the result of the work through extensive simulation case studies with Section 6.3 giving a discussion on the results. Section 7 gives the concluding remarks on the work.

The nomenclature used in the paper is summarized in Table 1.

Table 1: Nomenclature

DS	Drill string
PID	Proportional-integral-derivative
BHP	Bottom-hole pressure
BHA	Bottom-hole assembly
MPD	Managed-pressure drilling
KF	Kalman filter
MPC	Model predictive control
NMPC	Nonlinear MPC
UKF	Unscented Kalman Filter
SDE	Stochastic Differential Equation
EKF	Extended Kalman Filter
SP	Sigma Points
RIH	Run-in-hole
POOH	Pull-out-of-hole
OCP	Optimal control problem
NLP	Nonlinear programming problem
RMSE	Root-mean-square-of-error

2 Preliminaries

In this section, we present the preliminaries on modelling of lumped fluid flow in a pipe, the general stochastic differential equation with continuous Wiener processes, and finally an overview of nonlinear estimation in terms of the unscented Kalman filter. This is intended to give the reader some familiarity with the topics presented and the developed material in this paper.

Conservation of mass in a control volume is defined by the continuity laws, which are given as (Egeland and Gravdahl, 2002)

$$\frac{V_c}{\beta}\dot{p} = -\dot{V}_c - q_1 + q_2 \tag{1}$$

where V_c is the volume, β is the bulk modulus, p is the pressure, q_2 is flow into the volume and q_1 is the flow out of the volume. Using $d\rho = \frac{\rho}{\beta}dp$, and assuming equal density at the inlet and outlet of V_c, we consider positive flow direction upwards in the vertically oriented control volume.

Equivalently, we can express the momentum balance in terms of the rate-of-change of flow rate as a function of the net fluid pressure in the control volume (assuming that pressure is uniform in the volume) (Kaasa et al., 2012)

$$M\dot{q} = p_f(q) + p_1 - p_2 \tag{2}$$

where M is a fluid constant, p_f is the frictional pressure losses, p_1 is the upstream pressure in the control volume and p_2 is the pressure downstream of the control volume.

2.1 Stochastic differential equations

In general, many systems express a stochastic nature and therefore need to be treated with a deterministic and a stochastic part. A stochastic differential equation (SDE) in general form is given as

$$\mathrm{d}\mathbf{x}(t) = \mathbf{f}(\mathbf{x}, \mathbf{u}, \boldsymbol{\theta}, t)\mathrm{d}t + \mathbf{g}(\mathbf{x}, \mathbf{u}, \boldsymbol{\theta}, t)\mathrm{d}\mathbf{v}(t) \tag{3}$$

where $\mathbf{f}$ is the deterministic part of the SDE, $\mathbf{g}$ is the diffusion term, $\boldsymbol{\theta}$ is a system parameter vector, $\mathbf{v}(t)$ is a standard Wiener process (Brownian motion) depending on the time interval $t \in [t_0, t_f]$. The difference $\mathbf{v}(t) - \mathbf{v}(s)$ is normally distributed with zero mean and variance $\boldsymbol{\sigma}^2 = \mathbf{I}(t-s)$. Then, defining h as the time step $h = (t_f - t_0)/N$ and N is the number of increments from t_0 to t_f, we have

$$v_{j,k} - v_{j,k-1} = \mathrm{d}v_{j,k},\ v_0 = 0,\ k = 1, \ldots, N \tag{4}$$

where j is the number of noise variables, $\mathrm{d}v_k \sim \mathcal{N}(0, \sqrt{h})$ and $t_k = k\,h$.[1] To integrate the second part, including the diffusion term, an approximation of the stochastic integral is used due to the nondifferentiable state of $\mathrm{d}v$ (the term is not related to any past or present values) commonly either the Itô or the Stratonovich form (Chirikjian, 2009).

The SDE in (3), is then approximated numerically by a Taylor series expansion of defined order (here order 1, Euler or Runge Kutta-Maruyama) to simulate the stochastic behaviour.

The discrete-time measurement is formulated as

$$\mathbf{y}_k = \mathbf{h}(\mathbf{x}_k) + \mathbf{w}_k \tag{5}$$

where $\mathbf{y}_k$ is the sampled measurement values, $\mathbf{h}$ is the observation model, $\mathbf{w}_k \sim \mathcal{N}(0, \mathbf{R})$ is the zero-mean discrete-time measurement noise and $\mathbf{R}$ is the noise covariance.

2.2 The unscented Kalman filter

Physical states are in many cases not observable directly from the measurements. The system identification tool to obtain the system states or parameters (or combined) are the estimator. Estimation schemes applicable to nonlinear dynamics include the Extended KF (EKF) and the UKF. The EKF involves linearization of the system and observation model, to propagate the state and error covariance in time. However, divergence of the filter estimates can occur if the linearized model poorly represents the actual model and when large steps out from the linearized point $(\mathbf{x}^*, \mathbf{u}^*)$ are taken (Brown and Hwang, 2012, Chapter 7). The linearization is performed as

$$\boldsymbol{\phi} = \left.\frac{\partial \mathbf{f}}{\partial \mathbf{x}^\top}\right|_{\hat{\mathbf{x}},\mathbf{u}}, \quad \mathbf{H} = \left.\frac{\partial \mathbf{h}}{\partial \mathbf{x}^\top}\right|_{\hat{\mathbf{x}},\mathbf{u}}$$

where $\boldsymbol{\phi}$ is the linearized system transition matrix, $\mathbf{H}$ is the linearized output mapping matrix. To overcome the challenges, the UKF was introduced in Julier and Uhlmann (1997).

Using a nonlinear transform, the UKF estimates the system probability density function through a deterministic, minimal set of sigma points (SP). The use of SPs enables better approximation of the true mean and covariance by using a 2nd-order approximation, unlike the 1st-order approximation of the extended KF.

In this section, we consider the discrete-time dynamics of $\mathbf{x}_k$ and additive noise in the system. The notation $\mathbf{x}_{k|k-1}$ denotes the current sample given last sample time information about the mean. The time-update starts with a new draw of estimator SPs, $\mathcal{X}_k$, calculated according to the initial estimated mean of $\hat{\mathbf{x}}_{k-1}$ from last sample-time t_k as

$$\begin{aligned} \mathcal{X}_k^0 &= \hat{\mathbf{x}}_{k-1}, \\ \mathcal{X}_k^i &= \hat{\mathbf{x}}_{k-1} + \sqrt{(n_x+\lambda)}\,\mathrm{col}_i(\mathbf{U}), \\ \mathcal{X}_k^{i+n_x} &= \hat{\mathbf{x}}_{k-1} - \sqrt{(n_x+\lambda)}\,\mathrm{col}_i(\mathbf{U}) \end{aligned} \tag{6}$$

where $\mathbf{U} = \mathrm{chol}(\hat{\mathbf{P}})^\top$ is the Cholesky factorization of the state covariance matrix[2], $\mathrm{col}_i(\mathbf{U})$ is the ith column and n_x is the number of system states. The weights, determining the impact of each SP state is given as

$$\begin{aligned} \omega_\mu^0 &= \frac{\lambda}{n_x+\lambda},\ \omega_P^0 = \omega_\mu^0 + 1 - \alpha^2 + \beta \\ \omega_\mu^i &= \omega_\mu^{i+n_x} = \omega_P^i = \omega_P^{i+n_x} = \frac{1}{2(n_x+\lambda)} \end{aligned}$$

where ω_μ^i is the mean weights, ω_P^i is the covariance weights, $\lambda = \alpha^2(n_x+\kappa) - n_x$, α determines the spread around the mean, $\beta = 2$ assuming Gaussian distribution of $\hat{\mathbf{x}}_k$, and $\kappa = 3 - n_x$ is the scaling factor (Brown and Hwang, 2012).

The predicted mean $\bar{\mathbf{x}}_k$ and covariance $\bar{\mathbf{P}}_k$ are computed based on the nonlinear transformed stochastic variable, expressed as

$$\bar{\mathbf{x}}_{k|k-1}^i = \tilde{\mathbf{f}}(\mathcal{X}_k^i, \mathbf{u}_k), \tag{7}$$

$$\bar{\mathbf{x}}_{k|k-1} = \sum_{i=0}^{p} \omega_\mu^i \bar{\mathbf{x}}_k^i \tag{8}$$

$$\bar{\mathbf{P}}_{k|k-1} = \sum_{i=0}^{p} \omega_P^i (\bar{\mathbf{x}}_k^i - \bar{\mathbf{x}}_k)(\bar{\mathbf{x}}_k^i - \bar{\mathbf{x}}_k)^\top + \mathbf{Q}_k \tag{9}$$

where $\tilde{\mathbf{f}}$ is the nonlinear discrete-time state transition function, $\mathbf{u}_k$ is the discrete input, $p = 2m_x + 1$ and $\mathbf{Q}$ is the UKF covariance matrix. Furthermore, the predicted observation and its covariance and the resulting cross-covariance are computed according to

$$\bar{\mathbf{y}}_{k|k-1}^i = \tilde{\mathbf{h}}(\mathcal{X}_k^i, \mathbf{u}_k), \tag{10}$$

$$\bar{\mathbf{y}}_{k|k-1} = \sum_{i=0}^{p} \omega_\mu^i \bar{\mathbf{y}}_k^i \tag{11}$$

$$\bar{\mathbf{P}}_{yy,k|k-1} = \sum_{i=0}^{p} \omega_P^i (\bar{\mathbf{y}}_k^i - \bar{\mathbf{y}}_k)(\bar{\mathbf{y}}_k^{[i]} - \bar{\mathbf{y}}_k)^\top + \mathbf{R} \tag{12}$$

$$\bar{\mathbf{P}}_{xy,k|k-1} = \sum_{i=0}^{p} \omega_P^i (\bar{\mathbf{x}}_k^i - \bar{\mathbf{x}}_k)(\bar{\mathbf{y}}_k^i - \bar{\mathbf{y}}_k)^\top \tag{13}$$

where $\tilde{\mathbf{h}}$ is the (nonlinear) discrete-time observation model, $\bar{\mathbf{y}}_k^i$ is the predicted sigma point measurement,

[1] The Wiener process has infinite variance when $t \to \infty$.

[2] $\mathbf{U} = \mathrm{Chol}(\mathbf{P})^\top \iff \mathbf{U}\mathbf{U}^\top = \mathbf{P}$

$\bar{\mathbf{y}}_k$ is the predicted, weighted measurement, $\overline{\mathbf{P}}_{yy,k}$ is the observation covariance, $\overline{\mathbf{P}}_{xy,k}$ is the cross-covariance and $\mathbf{R}$ is the UKF measurement covariance.

When a new measurement sampling from the process sensors is obtained, a filter measurement update is performed. The a posteriori estimates are given by the Kalman filter update equations (Haug, 2012)

$$\mathbf{K}_{k|k-1} = \overline{\mathbf{P}}_{xy,k}\overline{\mathbf{P}}_{yy,k}^{-1} \tag{14}$$

$$\hat{\mathbf{P}}_{k+1|k} = \overline{\mathbf{P}}_k - \mathbf{K}_k\overline{\mathbf{P}}_{yy,k}^{-1}\mathbf{K}_k^\top \tag{15}$$

$$\hat{\mathbf{x}}_{k+1|k} = \bar{\mathbf{x}}_k + \mathbf{K}_k(\mathbf{y}_k - \bar{\mathbf{y}}_k) \tag{16}$$

where $\mathbf{K}_k$ is the Kalman gain at time t_k, $\hat{\mathbf{P}}_{k+1}$ is the a posteriori covariance estimate of $\mathbf{x}_k$, $\hat{\mathbf{x}}_{k+1}$ is the a posteriori estimate of the system states, and $\mathbf{y}_k$ is the measurement obtained at t_k. During each measurement sample-time interval, the filter prediction is updated using the current input and last iteration predicted mean $\bar{\mathbf{x}}_{k-1}$.

3 System modelling

Referring to Figure 1, the wellbore is discretized into a $2n-1$ degrees of freedom fluid dynamic model. The boundaries are $q_1 = q_c$ and the injection flow rate from the bit nozzle. The segments are explained as follows:

- segments 1 to $n-1$ consist of drill pipes,
- the last wellbore segment is the BHA, consisting of drill collars, the cutter, and various logging tools,
- positive flow direction is defined upwards in the annulus,
- the lumped control volume pressure p_i is uniform in each segment.

The wellbore representation is drawn from (Gjerstad et al., 2013), which derived a discretized hydraulic model where the frame of reference is fixed to the wellbore formation, such that the movement of the DS is assumed to alter the volumetric flow rate for the two lowermost segments. These consist of the largest geometrical changes of the DS assembly, causing larger flow variations when movement occurs.

The model was also derived considering two different diameters in each wellbore segment. This corresponds to two different flow rates and pressure states at these points in the annulus, which was included to approximate the pressure loss in terms of both laminar and turbulent flow in the annulus and DS. To reduce the number of states in the model, being derived from (1) and (2), the pressure forces for the **main** and **secondary** sections are lumped together. The main section (index 1) is either the drill pipe or collar, and the secondary section (index 2) is either the tool-joint or BHA. For annular flow, the secondary flow rate is the difference between the main section flow rate and the portion following the moving wall, yielding

$$q_2 = q_1 - (A_{f1} - A_{f2})v_s \tag{17}$$

where A_{f1} and A_{f2} are the cross-sectional flow areas. The averaged flow velocity in each section of the annular segment is then given as

$$\bar{v}_1 = \frac{q_1}{A_{f1}},\ \bar{v}_2 = \frac{q_2}{A_{f2}} \tag{18}$$

The model in this paper includes the above-mentioned properties, and we extended it to include the choke flow rate and the dynamics for the DS. We consider the case of no influx from the reservoir and that the wellbore is closed down-hole, i.e., the last control volume is closed. The normal forces of the fluid is then assumed to cancel the gravitational forces (also in the case of inclination), for each control volume. The length of the wellbore is assumed to be fixed during the time instant of tripping, such that we do not consider the extension due to drilling (i.e., the number of segments is fixed during operations).

3.1 Conservation of mass and momentum in wellbore

From Figure 1, the mass and momentum balances for each segment can be expressed as

$$\begin{aligned}
\frac{\epsilon}{\gamma}\frac{V_1}{\beta_1}\dot{p}_1 &= q_2 + q_{\text{bpp}} - q_c,\\
\frac{\epsilon}{\gamma}\frac{V_1}{\beta_i}\dot{p}_i &= q_{i+1} - q_i,\\
\frac{\gamma}{\epsilon}M_i\dot{q}_i &= F_{f,i}\gamma + A_{\text{eq},i}(p_i - p_{i-1}),
\end{aligned} \tag{19}$$

$$\frac{\epsilon}{\gamma}\frac{V_{n-1}}{\beta_{n-1}}\dot{p}_{n-1} = -\dot{V}_{n-1}\epsilon + q_n - q_{n-1}, \tag{20}$$

$$\frac{\epsilon}{\gamma}\frac{V_n}{\beta_n}\dot{p}_n = -\dot{V}_n\epsilon - q_v(p_n, p_I, \Delta p_b) - q_n \tag{21}$$

where $i \in \{2, \dots, n\}$, γ and ϵ are conversion factors (Pa and $\text{m}^3\cdot\text{s}^{-1}$ to bar and $\text{l}\cdot\text{min}^{-1}$, $\bar{p} = \gamma p$, $\bar{q} = \epsilon q$)[3], V_i is the segment volume, β_i is the bulk modulus of the segment, p_i segment pressure, q_i is the flow rate out from the segment, $q_1 = q_c$ is the choke flow, q_{bpp} is the input flow rate from the back pressure pump unit topside, $\dot{V}_i$ is the volume change due to surge and swab effects of a moving DS, M_i is a fluid constant, $F_{f,i}$ are the frictional pressure forces, $A_{\text{eq},i}$ is the equivalent area for the acting pressure forces, and q_v is the flow

[3]The bar over the variables are from here on omitted for convenience.

out from bit nozzle valves into the annular segment n, which will be further explained in Section 3.2.

The flow rate out of segment 1 is equal to the choke flow through the valve and is then subject to the pressure downstream, i.e. the pressure in the mud tank (being atmospheric for open tanks). The valve flow is expressed as

$$q_c = u_c C_c \sqrt{|p_1 - p_0|}\text{sign}(p_1 - p_0) \tag{22}$$

where $u_c \in [0, 1]$ is the valve control signal and C_c is the lumped choke valve coefficient. The differential pressure over the choke is $p_1 - p_0$, where p_0 is the atmospheric pressure in the mud tank.

Drill string movement results in pressure fluctuations in the annulus. These pressure changes are largest in the region where the geometrical changes of the DS are largest, specifically when the DS geometry changes from pipe to collar and the BHA (Gjerstad et al., 2013). This is due to the fluid velocity being larger when the annulus volume in the collar/BHA section is small. To account for the increase/decrease in rate of change for the pressure in the control volume for the last two segments, the time derivative of V is expressed as

$$\dot{V}_{n-1} = (A_p - A_c)v_s, \tag{23}$$

$$\dot{V}_n = A_c v_s \tag{24}$$

where v_s is the axial DS velocity, A_c is the collar cross-sectional area and A_p is the pipe cross-sectional area.

The pressure forces in each segment are expressed with the equivalent flow area, defined as

$$A_{\text{eq},i} = \pi(d_{w,i}^2 - d_{k,i}^2)/4 \tag{25}$$

where $d_{w,i}$ is the wellbore diameter and $d_{k,i}, k \in \{p, j, c, b\}$ is the outer string diameter, at segment i. The constant M_i is expressed as

$$M_i = A_{\text{eq},i}\rho_m \left(\int_{l_i}^{l_{i+1}} \frac{1}{A_{f1,i}} \mathrm{d}x + \int_{l_i}^{l_{i+1}} \frac{1}{A_{f2,i}} \mathrm{d}x \right) \tag{26}$$

where $\rho_m \mathrm{d}x = \mathrm{d}m_{1,i}$ is the infinitesimal fluid density per length in each section of the segment integrated for the flow path $\mathrm{d}x$ in the well. Furthermore, we assume uniform density in the sections, and according to (Kaasa et al., 2012), the parameter M_i is approximated in lumped hydraulic systems. Hence, in (26) $M_i \approx m_{1,i}/A_{f1,i} + m_{2,i}/A_{f2,i}$.

In Gjerstad et al. (2013), the frictional pressure forces are derived with Herschel-Bulkley fluid properties. These type of fluids reflect closely the properties of mud flow, being an approximation with fluid yield point related to the Bingham plastic and the power law model (Whittaker and EXLOG Staff, 1985). We will not repeat the derivations of the wall-shear stresses, and hence, the reader is referred to the work in Gjerstad et al. (2013).

The frictional forces arise from the wall shear stress from the fluid and is given as

$$F_{f,i} = A_{u1,i}\tau_{w1,i}(v_{1e}, v_s) + A_{u2,i}\tau_{w2,i}(v_{2e}, v_s)$$

where $A_{u1,i}$ is the boundary surface between mud and the surrounding borehole wall and DS in the main section, $\tau_{w1,i}$ is the corresponding averaged shear stress value over the main section wall surface area, $A_{u2,i}$ is the boundary surface between the mud and the secondary section and $\tau_{w2,i}$ is the averaged wall shear stress value for the secondary section, v_e is the effective flow velocity in the annular segment being the sum of velocity for the moving component in the control volume and actual flow velocity. The two components $\tau_{w1,i}$ and $\tau_{w2,i}$ are approximated by the laminar and turbulent flow regime for the mud flow with moving wall. The transition between these to regimes is modelled as

$$\tau_{\text{ii}w,i} = \tau_{w,i,\text{lam}} f_{\text{tr}} + \tau_{w,i,\text{turb}}(1 - f_{\text{tr}})$$

where ii= $\{1, 2\}$, and f_{tr} is a transition function depending on the equivalent Reynolds number for Non-Newtonian fluid.

3.2 Conservation of mass and momentum in the drill string

The inner volume of the DS is presented in Figure 2.

The inner volume of the DS is lumped into a single control volume, assuming a uniform pressure inside the string (Kaasa et al., 2012). The averaged flow velocities relative to the moving DS are given as

$$\bar{v}_{r1} = \frac{q_I}{A_{f1}} - v_s, \; \bar{v}_{r2} = \frac{A_{f1}}{A_{f2}}\bar{v}_{r1}. \tag{27}$$

Similar to the dynamics of a control volume in the annulus, the inner volume of the DS is comprised of the flow rate and pressure state, given as

$$\frac{\epsilon}{\gamma}\frac{V_I}{\beta_I}\dot{p}_I = q_v - q_I + v_s A_{I1}\epsilon \tag{28}$$

$$\frac{\gamma}{\epsilon} M_I \dot{q}_I = F_{I,f}\gamma + A_{\text{eq},I}(p_I - p_{\text{in}}) \tag{29}$$

where subscript I is for inner, the change in pressure from of DS heave is modelled with $\dot{V}_I$, $M_I = m_{I1}/A_{I1} + m_{I2}/A_{I2}$, A_{I1} is the main inner cross-sectional area and $A_{\text{eq},I} = \pi d_{p,i}^2/4$ is the equivalent area for the inner section with $d_{p,i}$ being the drill-pipe outer diameter for segment i. The inner frictional forces are defined as

$$F_{f,I} = A_{u1,I}\tau_{w,I1} + A_{u2,I}\tau_{w,I2} \tag{30}$$

where $A_{u[1-2],I}$ are the boundary surfaces of the fluid flow for the main and secondary sections, and $\tau_{w,I1-2}$ are the averaged shear stress value. Furthermore, the transition functions defines the contribution for each wall shear stress section for the inner control volume, expressed as

$$\tau_{w,I[1,2]} = \tau_{w,I,\text{lam}} f_{\text{tr}} + \tau_{w,I,\text{turb}}(1 - f_{\text{tr}}). \tag{31}$$

In the case of running mud through the DS, $p_{\text{in}} = p_{\text{spp}}$, where p_{spp} is the stand-pipe pressure. When the stand pipe is disconnected, the pressure at the inlet of the DS is atmospheric.

The inner DS control volume is defined as a single section. The diameters for this segment are defined by $d_{I,k}, k \in \{j, c, b\}$ for the secondary section and $d_{I,p}$ is the main section diameter (1).

In rotary drilling for high deviation wells, mud-motor or BHA turbines are applied to achieve high rotation speeds at the BHA. This is done by high pressure pumps topside, forcing large amounts of drilling mud into the string, rotating the turbines in the BHA for increased bit rotation speed (Black et al., 1986). The total pressure drop over the BHA is defined by the pressure drop over the turbine in the BHA lumped with other restrictions. We can then express the pressure drop over the BHA as

$$\Delta p_{\text{b}} = K_b q_I(t) \tag{32}$$

where K_b is a constant. The nozzle contains check valves, such that the flow is directed only out from the DS to the wellbore. Thus, the pressure drop over the valve is then

$$\Delta p_v = p_I - \Delta p_b - p_n. \tag{33}$$

The flow out from the nozzles is then a conditional function, which can be expressed by the valve equation as

$$q_v = \begin{cases} -K_v \sqrt{\frac{2\Delta p_v}{\gamma \rho_I}} \epsilon, \Delta p_v > 0 \\ 0, \Delta p_v \leq 0 \end{cases} \tag{34}$$

where K_v is the lumped nozzle valve constant.

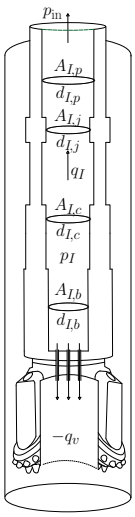

Figure 2: The inner DS control volume. The dynamics is lumped to one segment.

3.3 Rig travelling block dynamics

To account for the interaction between the DS and travelling block, we assume that we can represent the dynamics of v_s as a second-order mass spring damper model. The rig system is represented as a fixed element with an attached spring and mass, as seen in Figure 3.

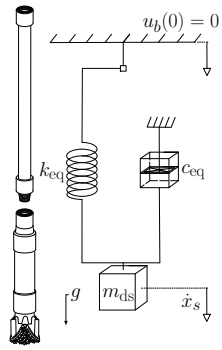

Figure 3: The rig and DS system.

The sum of forces for the point mass m_{ds} with sign convention equal to what is defined in the previous sections, the DS dynamics is derived as

$$-m_{\text{ds}}\ddot{x}_s - k_{\text{eq}}(x_s - u_b) - c_{\text{eq}}\dot{x}_s - m_{\text{ds}} g F_b = 0 \tag{35}$$

where x_s is the perturbation in DS position, $v_s = \dot{x}_s$, m_{ds} is the mass of the DS, k_{eq} is the equivalent DS stiffness, u_b is the position of the travelling block, c_{eq} is the equivalent damping to the surrounding fluid and formation, g is the gravitational constant and F_b is the buoyancy factor.

Using the transform $\xi = x_s - \frac{1}{k_{\text{eq}}} m_{\text{ds}} g F_b$ and dividing by m_{ds}, we can express (35) as

$$-\ddot{\xi} - \frac{k_{\text{eq}}}{m_{\text{ds}}}(\xi - u_b) - \frac{c_{\text{eq}}}{m_{\text{ds}}}\dot{\xi} = 0 \tag{36}$$

where ξ is the deviation from the suspended equilibrium point, in tension due to the gravitational forces acting on the DS. We proceed to define the system $s_1 = \xi$, $s_2 = \dot{\xi}$ and

$$\dot{\mathbf{s}} = \begin{bmatrix} s_2 \\ -\omega_n^2 s_1 - 2\omega_n \zeta s_2 + \omega_n^2 u_b \end{bmatrix} \tag{37}$$

where $\omega_n = \sqrt{k_{\text{eq}}/m_{\text{ds}}}$ is the natural frequency of the system, and $\zeta = c_{\text{eq}}/(2\sqrt{m_{\text{ds}} k_{\text{eq}}})$ is the relative damping factor. Increased damping due to increasing mud flow is not included in this analysis, as we assume a constant damping factor for the mechanical system.

The reference trajectory controller for the travelling block can be derived to fully complete the rig dynamics. With a linear system representation for the rig dynamics, we choose common methods to define u_b as

$$\begin{aligned} u_b &= -k_1(s_1 - u_r) - k_2 s_2 - k_3 \sigma \\ \dot{\sigma} &= s_1 - u_r \end{aligned} \tag{38}$$

where k_1, k_3 and k_2 is the proportional, integral and derivative gains respectively constituting a common PID control law (Khalil, 1996). The gains are chosen such that the system $\mathbf{P} = \mathcal{A} - \mathcal{B}\mathcal{K}$ is Hurwitz, and

$$\mathcal{A} = \begin{bmatrix} \mathbf{A}_z, \mathbf{0} \\ [1,0], 0 \end{bmatrix}, \; \mathcal{B} = [0,1,0]^\top, \; \mathcal{K} = [k_1, k_2, k_3]$$

where $\mathbf{A}_z = \partial \mathbf{f}(\mathbf{s})/\partial \mathbf{s}|_{s_{i,\text{ss}}, u_{b,\text{ss}}}$, and $\mathbf{f}(\mathbf{s})$ is given by (37).

Then, following the Routh-Hurwitz Criterion for a stable characteristic polynomial $\det(\mathbf{I}s - \mathbf{P}) = 0$ (Khalil, 1996, Chapter 12.4), the gains

$$k_1 > \frac{k_3}{\omega_n^2 k_2 + 2\omega_n \zeta}, \; k_2 > 0, \; k_3 > 0$$

ensures the Hurwitz condition.

Inserting (38) into (37), the DS and travelling block model constitutes then

$$\begin{aligned} \dot{z}_1 &= z_2 \\ \dot{z}_2 &= -\omega_n^2(1+k_1) z_1 + \omega_n^2 k_1 u_r - \omega_n(2\zeta + \omega_n k_2) z_2 - \omega_n^2 k_3 z_3 \\ \dot{z}_3 &= z_1 - u_r \end{aligned} \tag{39}$$

where $z_1 = s_1$, $z_2 = s_2$, $z_3 = \sigma$, and the supervisory control input is actuating the reference u_r.

3.4 State-space formulation

The wellbore and DS model from Section 3 can be formulated as a $2n + 1$ degrees of freedom state-space model, where the wellbore is modelled with n pressure states and $n - 1$ flow rate states, and the inner DS contains two states.

Let $n_x = 2n+1$, $\mathbf{x}_1 = [p_1, q_2, p_2, \ldots, q_n, p_n]^\top$, $\mathbf{x}_2 = [q_I, p_I]^\top$, $\mathbf{u} = [v_s, q_c, q_{\text{bpp}}, p_{\text{in}}]^\top$ be the state vectors and input vector, then the wellbore dynamics can be formulated in state-space form as

$$\dot{\mathbf{x}}_1 = \mathbf{A}_1 \mathbf{x}_1 + \mathbf{B}_1 \mathbf{u} + \mathbf{F}_1 \mathbf{f}_1(z_2, \mathbf{x}_1) + \mathbf{e}_1 q_v(\mathbf{x}_1, \mathbf{x}_2) \tag{40}$$

where the system matrices and vectors are derived as

$$\mathbf{A}_1 = \begin{bmatrix} 0 & B_1 & 0 & 0 \ldots & & & \\ -\tilde{M}_2 & 0 & \tilde{M}_2 & 0 \ldots & & & \\ 0 & -B_2 & 0 & B_2 \ldots & & & \\ \vdots & & \vdots & \ddots & \vdots & & \vdots \\ & & & \ldots & 0 & B_{n-1} & 0 \\ & & & \ldots & -\tilde{M}_n & 0 & \tilde{M}_n \\ & & & \ldots & 0 & -B_n & 0 \end{bmatrix},$$

$$\mathbf{B}_1 = \begin{bmatrix} 0 & & -B_1 & B_1 & 0 \\ \vdots & & & & \vdots \\ 0 & & 0 & 0 & 0 \\ -(A_p - A_c) B_{n-1} \epsilon & & 0 & 0 & 0 \\ 0 & & 0 & 0 & 0 \\ -A_c B_n \epsilon & & 0 & 0 & 0 \end{bmatrix},$$

$$\mathbf{F}_1 = \text{diag}([0, M_2^{-1}, 0, \ldots 0, M_n^{-1}]^\top)\epsilon$$

$$\mathbf{f}_1 = [0, F_{f,1}, 0, \ldots 0, F_{f,n}]^\top,$$

$$\mathbf{e}_1 = [0, \ldots, 0, -B_n]^\top.$$

Similarly, for the inner DS we have

$$\dot{\mathbf{x}}_2 = \mathbf{A}_2 \mathbf{x}_2 + \mathbf{B}_2 \mathbf{u} + \frac{\epsilon}{M_I} \mathbf{f}_2 + \mathbf{e}_2 q_v(\mathbf{x}_1, \mathbf{x}_2), \tag{41}$$

where the $\mathbf{x}_2$ system matrices are defined as

$$\mathbf{A}_2 = \begin{bmatrix} 0 & \tilde{M}_I \\ -B_I & 0 \end{bmatrix}, \; \mathbf{B}_2 = \begin{bmatrix} 0 & \mathbf{0} - \tilde{M}_I \\ A_{I1} B_I \epsilon & \mathbf{0} \quad 0 \end{bmatrix},$$

$$\mathbf{f}_2 = [F_{f,I}(z_2, q_I), 0]^\top, \; \mathbf{e}_2 = [0, B_I]^\top$$

where $B_k = \gamma \beta_k/(\epsilon V_k)$, $B_I = \gamma \beta_I/(\epsilon V_I)$, $\tilde{M}_k = A_{\text{eq},k}\epsilon/(\gamma M_k)$, $\tilde{M}_I = A_{I\text{eq}}\epsilon/(\gamma M_I)$, and $k \in \{1, \ldots, n\}$.

The rig dynamics is already in a state-space formulation, and the total system is then given by the vector $\tilde{\mathbf{x}} = [\mathbf{z}^\top, \mathbf{x}_1^\top, \mathbf{x}_2^\top]^\top$

4 System identification

In this section, we address the system identification for the offshore drilling operations with special attention to running connections. This is due to having no circulation of mud flow when performing this operation, which implies that the nozzle flow through the bit is reduced or zero. We wish to obtain estimates of the system states to monitor the pressures in the discretized wellbore along with the wellbore flow. To design a state controller, we require full-state knowledge of the system.

The measured outputs when circulating mud are assumed to be $y = \{z_1, \Delta p, p_n, q_I\}$, and $y = \{z_1, \Delta p, p_n\}$

otherwise, where $\Delta p = p_1 - p_0$ is the differential pressure over the choke. The observation model $\mathbf{h}$ during circulation is defined as

$$\mathbf{y}_k = \mathbf{h}(\tilde{\mathbf{x}}_k) = \begin{bmatrix} 1 & \mathbf{0} & 0 & \mathbf{0} & 0 & 0 & 0 \\ 0 & \mathbf{0} & 1 & \mathbf{0} & 0 & 0 & 0 \\ 0 & \mathbf{0} & 0 & \mathbf{0} & 1 & 0 & 0 \\ 0 & \mathbf{0} & 0 & \mathbf{0} & 0 & 1 & 0 \end{bmatrix} \tilde{\mathbf{x}} - \begin{bmatrix} 0 \\ p_0 \\ 0 \\ 0 \end{bmatrix}, \tag{42}$$

where k is the discrete time index, and in the case of no circulation, $p_{\text{in}} = p_0$ and $\mathbf{h}$ is reduced by removing the fourth row.

In terms of the proposed model for the drilling operations, linearization of (22) and (34) leads to a singularity. When the pressure difference is negative or zero in (34), the expression becomes invalid and requires special numerical treatment when evaluating the simulation model. Due to this, we design a state and parameter estimator with the UKF. The UKF uses the nonlinear model directly in time propagation of the mean at its covariance from (40) and (41).

4.1 Observability

We must ensure that the deterministic systems (39), (40) and (41) are observable with (42) at time t_k when sampling is performed. Observability is a measure of the system property to reconstruct the state x_k given an input-output map y_k, u_k. For a linear system, this implies that the observability matrix formed by the system and output matrices has full rank (see e.g., Chen (2013, Chapter 6.3)). For nonlinear systems this is not a straight forward procedure, and often reduces to the previously mentioned rank test for linear systems. The conditions for nonlinear observability is addressed in Hermann and Krener (1977); Kou et al. (1973)

According to Hermann and Krener (1977), we can show locally weak observability by calculating the Lie derivatives[4] up to $n_x - 1$, and check the rank of the resulting Jacobian.

The linear second-order system comprising the rig dynamics in (37) can be shown to be observable for the measurement z_1. The hydraulic system has a potential observability problem, with too few linearly independent measurements compared to the number of estimated states in the $\mathbf{x}_1, \mathbf{x}_2$ system. Therefore, before designing the estimator we need to ensure system observability with the limited measurements. Consider a wellbore DS system with $n = 2$ (two segments), annular frictional pressure force are assumed to be quadratic in flow rate $f_j = -k_{fj} x_j^2$, where $j = \{2, 4\}$ and k_f is a constant (Kaasa et al., 2012). Using $\mathbf{u} = [u_{z_2}, (q_c + q_{\text{bpp}}), p_{\text{in}}]$, we can arrange (40) and (41) as

$$\begin{aligned} \dot{\mathbf{x}} &= \begin{bmatrix} \mathbf{A}_1 & 0 \\ 0 & \mathbf{A}_2 \end{bmatrix} \mathbf{x} + \begin{bmatrix} \mathbf{F}_1 & 0 \\ 0 & \mathbf{F}_2 \end{bmatrix} \mathbf{f}(\mathbf{x}) + \begin{bmatrix} \mathbf{B}_1 \\ \mathbf{B}_2 \end{bmatrix} \mathbf{u} + \mathbf{e} q_v(\mathbf{x}) \\ \mathbf{y} &= \mathbf{h}(\mathbf{x}) = [x_1 - p_0, x_3]^\top \end{aligned} \tag{43}$$

where $\mathbf{x} = [\mathbf{x}_1^\top, \mathbf{x}_2^\top]^\top$, $\mathbf{F}_1 = \text{diag}([0, -k_{f,2}, 0])$, $\mathbf{F}_2 = \text{diag}([-k_{f,4}, 0])$, $\mathbf{f}(\mathbf{x}) = [0, x_2^2, 0, x_4^2, 0]^\top$, $\mathbf{B}_1$ and $\mathbf{B}_2$ are given as in (40) and (41) by removing the third column, $\mathbf{e} = [0, 0, -B_3, 0, -B_I]^\top$, and $q_v \in C^1$ from (34) being a nonlinear function in $\mathbf{x}$. The state x_3 then corresponds to p_n and x_5 is the inner drill string pressure, p_I.

The system in (43) is observable if the following input-output map exists

$$H(\mathbf{x}) = \begin{bmatrix} \mathbf{h}(\mathbf{x})^\top & L_f h & \dots & L_f^{n_x - 1} h \end{bmatrix}^\top \tag{44}$$

and the Jacobian of H has full rank, i.e $\text{rank}(\mathcal{O}) = n_x$, where $L_f^i h = ((\partial L_f^{i-1} h / \partial \mathbf{x})\, \dot{\mathbf{x}})^\top$ is the ith Lie derivative and $L_f^0 h = \mathbf{h}^\top$.

The system is nonlinear and due to this, the results only show local weak observability at the operating point $\mathbf{x}_{\text{ss}}$. Using the symbolic toolbox in `MATLAB` we see that the system in (43) is locally weakly observable for $q_v > 0$ and that $\mathcal{O}$ does not have full rank for $q_v = 0$.

In that case, the state $x_4 = q_I$, $x_5 = p_I$ are nonobservable from the output $\mathbf{y}$. This is reasonable, due to $q_v(\mathbf{x})$ connecting the inner DS system to the wellbore system. Hence, when circulation is off, the system is only locally weakly observable for cases $x_5 > K_b x_4 + x_3$.

4.2 State and parameter estimator design

The deterministic systems (39)–(41) can be used to formulate a continuous-discrete SDE state transition and observation model as in (3) and (5). This is done to include a diffusion term $\mathbf{g}$, representing the model errors and fluctuations in the state $\mathbf{x}$ capturing random effects of the wellbore system.

The frictional pressure drop in the annulus is commonly estimated by running tests, fitting an n-th order polynomial to the data and using this in the model (Kaasa et al., 2012; Landet et al., 2012). Due to the uncertain nature of the wellbore dynamics, we choose to represent the first-principles friction model in (40) by a quadratic estimate of the pressure forces arising from the friction in the annular volumes. The estima-

[4] For a more detailed description of Lie derivatives, see e.g., Slotine and Weiping (1991).

tion model is then given as

$$\begin{aligned}
\mathrm{d}\mathbf{z} &= \mathbf{f}_z(\mathbf{z}, u_r)\mathrm{d}t + \mathbf{g}(\mathbf{z}, t)\mathrm{d}\mathbf{v}_z \\
\mathrm{d}\mathbf{x}_1 &= (\mathbf{A}_1\mathbf{x}_1 + \mathbf{F}_1\hat{\mathbf{f}}_1 + \mathbf{B}_1\mathbf{u} + \mathbf{e}_1 q_v)\mathrm{d}t + \mathbf{g}(\mathbf{x}_1, t)\mathrm{d}\mathbf{v}_1 \qquad (45)\\
\mathrm{d}\mathbf{x}_2 &= (\mathbf{A}_2\mathbf{x}_2 + \frac{\epsilon}{M_I}\mathbf{f}_2 + \mathbf{B}_2\mathbf{u} + \mathbf{e}_2 q_v)\mathrm{d}t + \mathbf{g}(\mathbf{x}_2, t)\mathrm{d}\mathbf{v}_2 \\
\hat{\mathbf{f}}_1 &= [\hat{F}_{f,2}, \ldots, \hat{F}_{f,n}]^\top \\
\hat{F}_{f,i} &= \hat{\theta}_i|\bar{v}_i + K_c z_2|(\bar{v}_i + K_c z_2) \qquad (46)
\end{aligned}$$

where $\mathrm{d}\hat{\theta}_{i-1} = \mathrm{d}v_{\theta_{i-1}}$, $i = 2, 3, \ldots, n_x - 3$, $\mathbf{f}_z$ is the deterministic part from (39), $\mathbf{g}$ is the diffusion terms determining the average fluctuations in $\mathbf{x}$, $\mathbf{v}$ are Wiener processes satisfying $\mathbf{v}(t) - \mathbf{v}(s) \sim \mathcal{N}(0, \mathbf{I}\mathrm{d}t)$, $\hat{F}_{f,i}$ is the annular segment estimated pressure force set up by friction with $\hat{\theta}$ being the estimated coefficient for each annular wellbore section, $\bar{v}_i = q_i/A_{f1,i}$ and K_c is the clinging constant for the fluid attached to the moving DS. We assume to have prior knowledge of K_c, which can be calculated for laminar flow as

$$K_c = \frac{1}{2\ln\alpha_i} + \frac{\alpha_i^2}{(1-\alpha_i^2)} \qquad (47)$$

where $\alpha_i = d_{1,i}/d_w$ and d_w is the wellbore diameter, and $d_{1,i}$ is the main diameter for the segment. The term between the brackets in (46) is referred to as the effective velocity (Whittaker and EXLOG Staff, 1985). The number of parameters to be estimated should correlate with the number of measurements or be driven by a persistent excitation signal. Hence, we assume full knowledge of the fluid behavior in the DS volume. The parameters are assumed to be random walk processes with equal distribution as the Wiener process.

The measured outputs are given by the criteria for operation (from Section 4), given as

$$\mathbf{y}_k = \left[z_1,\, x_{1,1} - p_0,\, x_{1,2n-1},\, x_{2,1}\right]^\top + \mathbf{w}_k \qquad (48)$$

where $\mathbf{w} = [w_1, w_2, w_3, w_4]^\top, \sim \mathcal{N}(0, \boldsymbol{\sigma}_w^2)$, $\boldsymbol{\sigma}_w^2$ is the measurement noise variance.

The discrete-time estimation model in (45) is obtained by using the Runge-Kutta Maruyama order 4 integration method from Rößler (2006), with step length equal to the plant simulation model.

The estimator propagates the stochastic state vector $\mathcal{X}^i$ through the nonlinear process model. Following the notation defined in the preliminaries of Section 2.2, the filtering algorithm is summarized in Alg. 1. The UKF algorithm runs at the same frequency as the plant model. However, the UKF measurement update is in this work set at a different frequency. The measurement sampling time in the UKF is denoted t_m.

The algorithm assumes additive uncorrelated white noise ($E[\mathbf{w}\mathbf{v}^\top] = E[\mathbf{w}\mathbf{x}_0^\top] = 0$ and $E[\mathbf{v}\mathbf{x}_0^\top] = 0$). This allows us to simplify the computations by not calculating additional sigma points for $\mathbf{v}_k, \mathbf{w}_k$ to be projected through the nonlinear transform and observation model.

Algorithm 1 Unscented Kalman filter

```
Initialize: P̂_0, x̂_0, Q, R
while Run-time: do
    if mod(time, t_m) ≠ 0 then
        Time-update: x̂_{k-1}, P̂_{k-1}
        Compute a new set of sigma points X_k^i from (6)
        for i = 0 to p do
            Predict x̄_k^i in (7)
        end for
        Predict new weighted mean x̄_k (8)
        Compute the predicted covariance P̄_k (9)
        Return: x̄_k, P̄_k
    else
        Measurement-update: y_k is sampled
        Compute K_k, x̂_k and P̂_k from (14), (16) and (15)
        Return: x̂_k, P̂_k
    end if
end while
```

4.3 State estimation with no mud circulation

Consider a wellbore system with $n = 4$ number of pressure states (discretizing the wellbore into four segments). To confirm our predictions on observability, we sample the plant model in (45) at 100 Hz, running-in-hole (RIH) with circulation off. The wellbore and DS data are given in Table 2, based on Lyons et al. (2015, Ch. 4.6.4), and the scenario is similar to what is seen in Figure 5 and 6 in (Gjerstad et al., 2013).

The estimator data and initial conditions are given in Table 3. The measurement noise variance is calculated as $\sigma_{i,w}^2 = (W_i y_{i,\mathrm{nom}})^2$ where σ_w is the standard deviation, $y_{i,\mathrm{nom}}$ is a chosen nominal signal value for the individual measurement and W_i is corresponding signal noise amplitude.

The pressure at the top of the DS is set to atmospheric pressure, and the choke position is set to 50%. The imperfect model estimates resulting from driving the block 28 meters downwards, simulating run-in of the drill string in the wellbore.

The estimated pressure state and true values are seen in Figure 4. The pressure estimate $\hat{p}_I$ does converge, but is seen to have a constant bias. It is seen that the inner DS flow rate is excited by the DS velocity and is closer to its true value.

The back-pressure pump kept is ramped up at $t = 2$ min to 400 l/min. The DS velocity is negative when RIH is performed, and the velocity returns to zero as the new pipe section is put in place. The estimated states are seen to converge close to their true values.

Table 2: Wellbore and drill string data. TJ - Tool joint, DC - drill collar.

Number of segments n	4	[-]
Length, segment i	1092	[m]
Length, segment n	344.1	[m]
L_{TJ}, L_{DC}, L_{BHA}	0.25, 251.1, 60	[m]
L_{DS} total	3607.8	[m]
d_{p}, d_{j}	0.1270, 0.1684	[m]
d_{c}, d_{b}	0.1270, 0.1740	[m]
d_ws (uniform)	0.245	[m]
$d_{\text{I,p}}$, $d_{\text{I,j}}$	0.1087, 0.0825	[m]
$d_{\text{I,c}}$, $d_{\text{I,b}}$	0.0810, 0.0988	[m]
A_{eq}, $A_{\text{eq,I}}$	0.0343, 0.0449	[m]
K_v	$5.199{\cdot}10^{-4}$	[-]
C_c	0.0016	[-]
K_b	0.005	bar min L^{-1}
ρ_m, ρ_s	1800, 7850	[kg m^{-3}]
β_i	$6.5 \cdot 10^9$	[Pa]
Parameters modified from Fig. 2 in (Gjerstad et al., 2013):		
a, b	0.1, 0.2	[-,-]
a_I, b_I	0.024, 0.21	[-,-]
$\tau_{y,I}$	15	[Pa]
n_f, k	0.79, 0.15	[-,-]

Table 3: Noise and estimator parameters.

$\mathbf{g}_p, \mathbf{g}_q$	0.0025, 10	[-]
W_i	$[1\%, 5\%, 10\%]$	[-]
$y_{i,\text{nom}}$	$[1, 1, 1]$	[m, bar, bar]
$\mathbf{q}_\theta$	$[10^4, 10^4, 10^4]^\top$	[-]
$\mathbf{Q}$	$\text{blkdiag}([10^{-5}, 10^{-5}, 10^{-5}], \mathbf{g}, \mathbf{q}_\theta)$	[-]
$\mathbf{R}$	$\text{diag}(\boldsymbol{\sigma}_w^2)$	[-]
t_m, α_{ukf}	0.01, 1	[s,-]

The variance and measurement noise of the system generates a rapidly varying frictional pressure force for the inner-DS, as seen in Figure 5.

Constant deviations for the estimated frictional pressure forces from the true value are seen, in the rightmost of Figure 5 for $\hat{F}_{f,i}$. However, the estimates converge but with a significant bias.

From this study, some of the uncertainties in the process of RIH or making pipe connection to process disturbances are seen. To properly address the issue of a nonobservable $\mathbf{x}_2$ system, in the specific case of no mud-circulation, we will have to treat q_v as a disturbance in the control system when circulation is off.

5 Control design for drilling operations

This section presents the controller design for the tripping operations in offshore drilling. As discussed in Section 4, in the case of no circulation (such as running pipe connections), an estimator control design must be built around the assumption of a disturbance flow from the bit nozzle.

We assume that we have all the available measurements (mud circulation is on) and concern this work with maintaining BHP pressure at reference, while pulling out or running in the DS. The main focus is then to control the BHP, actuating the travelling block, z_1, back-pressure pump q_{bpp}, stand-pipe pressure p_{spp} and choke valve opening u_c, keeping the actuator and process constraints intact. The block position is used for pull-out-of-hole (POOH) or RIH, maintaining the

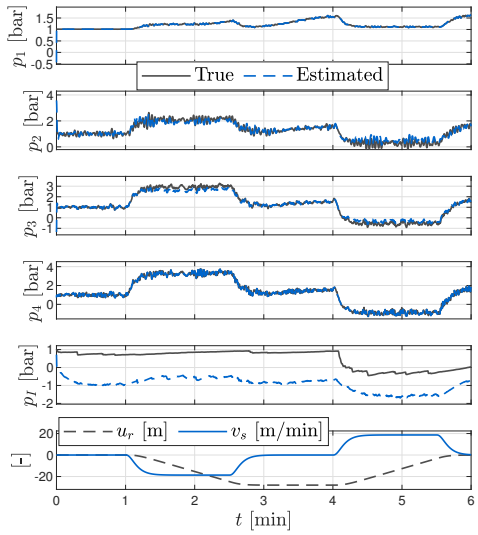

Figure 4: RIH estimated pressure states.

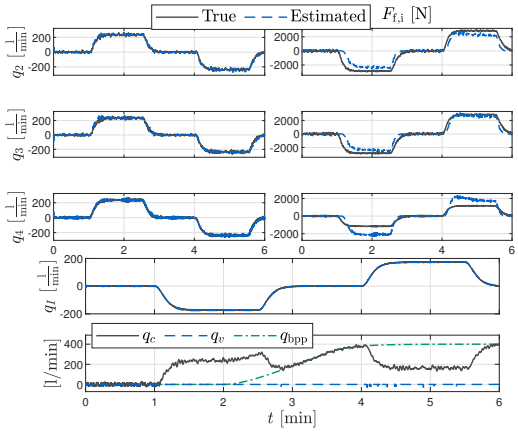

Figure 5: RIH flow rates, and wellbore friction force estimates.

constraints on DS velocity in the wellbore. Multivariable control, with both Δp and p_n is presented in the last simulation case study.

A natural choice of control law with the requirements discussed above is the MPC. The MPC is a widely applied process control law for both linear and nonlinear applications. It is an advanced method of optimal control with *receeding horizon control*, meaning that the measured output at sample-time t_s together with current and future constraints on x, y and u are taken into account. For a thorough discussion on the topic of nonlinear optimal control, see e.g., Findeisen and Allgoewer (2002); Grune and Pannek (2011).

The MPC has become an industry standard in process control, with special focus on advanced application where process constraints are important (Qin and Badgwell, 2003). The MPC control algorithm uses a form of the actual plant model (either true or estimated), to predict future behaviour of the process and optimal inputs. At each sampling instant, process states are obtained (given by a estimator/observer and sensors) and the MPC utilizes a state prediction to form the optimal control input $\bar{\mathbf{u}}$ on an extended process horizon (Findeisen and Allgoewer, 2002). A disadvantage is that the MPC can be influenced by modeling errors (Grune and Pannek, 2011). Vital ingredients in an MPC algorithm is process and actuator constraints, a cost function and a model.

5.1 Constrained BHP Control

To constrain the inputs and system, we choose to design the control law around the MPC framework. We can either linearize and use the conventional linear MPC, or use the nonlinear model in predicting future process behaviour. The latter seems to be the better choice due to the nonlinearity of the bit nozzle and choke valves. Also, a nonlinear version will be robust on a broader range of operating points than the linearized MPC. The disturbance from DS heave and eventually the flow through q_v is then included when predicting future optimal inputs for the process.

The NMPC is based on using a plant model to predict the future control inputs, leading the measurement values to their respective references. An optimal control problem (OCP) is defined, based on a nonlinear prediction model, system equality and inequality constraints. This involves either a continuous or discrete nonlinear programming problem (NLP), which the NMPC solves to obtain the optimal, constrained input. An important real-time criterion for the NLP is that the solution must be obtained before the next sampling time occurs. For each future sample-time, the input is open-loop applied in the prediction model $\tilde{\mathbf{x}}_{j+1} = \mathbf{f}(\tilde{\mathbf{x}}_j, \mathbf{u}_j, \boldsymbol{\theta}_k)$, in a finite prediction interval.

The NMPC uses the discretized augmented deterministic nonlinear model in (45) to predict future states and outputs. The discrete-time OCP for the NMPC is defined as (in the following, the tilde notation on $\mathbf{x}$ is removed for convenience)

$$\min_{\mathbf{u},\boldsymbol{\xi}} \sum_{j=0}^{N_p} \Big((\mathbf{y}_j - \mathbf{y}_j^{\text{ref}})^\top \mathbf{W}_c (\mathbf{y}_j - \mathbf{y}_j^{\text{ref}}) + \boldsymbol{\xi}_j^\top \mathbf{T} \boldsymbol{\xi}_j \Big) + \sum_{j=0}^{N_c} \Big(\Delta \mathbf{u}_j^\top \mathbf{R}_c \Delta \mathbf{u}_j + (\mathbf{u}_j - \mathbf{u}_j^{\text{ref}})^\top \mathbf{R}_r (\mathbf{u}_j - \mathbf{u}_j^{\text{ref}}) \Big) \quad (49)$$

where j is sample interval index, $N_p = T_p/t_s$ and $N_c = T_c/t_s$ is the discrete prediction and control intervals respectively, T_p is the prediction horizon, T_c is the control horizon, t_s is the MPC sampling time, $\mathbf{W}_c$ is the set-point weight matrix, $\boldsymbol{\xi}_j$ are the slack variables, $\mathbf{T}$ is the slack variable weight matrix, $\mathbf{R}_c$ is the weighting matrix for the slew in control input, $\mathbf{R}_r$ is the input reference trajectory weight matrix, and $\Delta \mathbf{u}_j = \mathbf{u}_j - \mathbf{u}_{j-1}$. The subscript c is used on the MPC to distinguish its variables from those of the UKF.

The state, output and input constraints are defined as

$$\begin{aligned} \text{s.t.,}\ \mathbf{x}_0 &= \mathbf{x}_k, \mathbf{u}_0 = \mathbf{u}_{k-1}, \\ \mathbf{x}_{j+1} &= \mathbf{f}(\mathbf{x}_j, \mathbf{u}_j, \boldsymbol{\theta}_k) \quad (50) \\ \mathbf{y}_j &= \mathbf{h}(\mathbf{x}_j),\ j = 0, \ldots, N_p \\ \mathbf{u}^- \le \mathbf{u}_j &\le \mathbf{u}^+,\ j = 0, \ldots, N_c \\ \Delta \mathbf{u}_j^- \le \Delta \mathbf{u}_j &\le \Delta \mathbf{u}_j^+\ j = 0, \ldots, N_c \quad (51) \\ \mathbf{u}_j - \mathbf{u}_{j-1} &= \mathbf{0},\ j \ge N_c. \end{aligned}$$

The hard constraints are in this case the upper and lower bound on the inputs. The rest are subject to slack variables. The prediction in $\mathbf{f}(\mathbf{x}_j, \mathbf{u}_j, \boldsymbol{\theta}_k)$ is given by (45). The NLP is then implemented as a *sequential approach*, using finite parametrization of the control inputs (Findeisen and Allgoewer, 2002).

The following additional constraints are defined:

$$z_{2,L} - \boldsymbol{\xi}_{1,j} \le z_{2,j} \le z_{2,H} + \boldsymbol{\xi}_{2,j} \quad (52a)$$
$$(p_n + k_b q_I) - \boldsymbol{\xi}_{4,j} \le p_{I,j} \quad (52b)$$
$$\Delta p_{n,L} - \boldsymbol{\xi}_{5,j} \le \Delta p_j \le \Delta p_H + \boldsymbol{\xi}_{6,j}, \quad (52c)$$
$$p_{n,L} - \boldsymbol{\xi}_{7,j} \le p_{n,j} \le p_{n,H} + \boldsymbol{\xi}_{8,j}, \quad (52d)$$
$$0 \le \boldsymbol{\xi}_j \le \boldsymbol{\xi}^{\max},\ j = 0, \ldots, N_p, \quad (52e)$$

where the subscripts, L, H are the low and high band control limits, respectively.

In addition to constraining the input change on the travelling block movement, the first constraint in (52a) denotes the maximum and minimum DS velocity, which is calculated from (39). Rapid changes in the travelling block might result in large pressure spikes. In

(52b) the requirement is to keep the pressure in the DS higher than the turbine loss and BHP pressure, such that flow spikes into the wellbore are avoided while circulating. The slack variables $\boldsymbol{\xi} > 0$ define soft constraints in (52a)-(52e). These are included to allow minor violation in short intervals of the constraints on $\mathbf{x}_j$, such that a feasible solution is found. However, it is important to enforce hard constraints on actuator limitations. The band control limits on the BHP and choke differential pressure can be set in (52d).

A PI-controller is used to adjust the choke valve opening. The NMPC sends the desired choke flow rate to the controller, adjusting the choke to comply with the requirement. To constrain the flow control algorithm, we implement a nonlinear constraint on the choke flow in the NMPC. The flow constraint given as

$$\begin{aligned} q_{c,j}^{\text{ref}} &\leq q_{c,j}^{\max} + \boldsymbol{\xi}_{3,j} \\ q_{c,j}^{\max} &= C_c \sqrt{|\Delta p_j|} \text{sign}(\Delta p_j) \end{aligned} \tag{53}$$

The discrete form of (49) and (50) are approximated by repeated forward Euler integration on the interval $[t_k, t_k + N_p]$. An intermediate step-length for integrating the differential equation in (45) is implemented, such that the sampling interval from start to end is divided into $\tau_s = t_s/M$. The scheme is formulated in Alg. 2. Similarly, a Runge Kutta method, or any other discretization scheme, can be used. Exact discretization is only applicable if linearization of (45) is done prior to discretization. The input $\mathbf{u}_j$ is held constant on the intermediate integration interval.

Algorithm 2 Euler-discretization of $\mathbf{f}$

1: Input: $\mathbf{x}_a$, $\mathbf{u}$, $\boldsymbol{\theta}$, t_k, t_s, M
2: Set step length $\tau_s = t_s/M$, M: Number of iterations
3: $\mathbf{x}_0^1 = \mathbf{x}_a$
4: **for** $k = 0$ to $M - 1$ **do**
5: $\quad t = t_k + kt_s$
6: $\quad \mathbf{x}_{a,k+1} = \begin{bmatrix} \mathbf{x}_k \\ \boldsymbol{\theta}_k \end{bmatrix} + \tau_s \begin{bmatrix} \mathbf{f}(t, \mathbf{x}_k, \mathbf{u}_k, \boldsymbol{\theta}_k) \\ \mathbf{0} \end{bmatrix}$
7: **end for**
8: Return $[\mathbf{x}_{a,k+1}]$

Solving (49) gives the optimal $\bar{\mathbf{u}}_k$ for the process, based on the initial guess. The initial guess is effectively drawn from the previous sample time control sequence. The NMPC is implemented in `MATLAB`, using `fmincon` with `SQP`. The NMPC algorithm can be summarized as in Alg. 3.

In (50), we utilize the forward Euler integration for the prediction model as described in Alg. 2. We choose to distinguish between the prediction and control intervals, and set $N_c = T_c/t_s$. This implies that we use the linear equality constraint, defined in (51).

The topography of the system is presented in Figure 6. The NMPC sends the calculated reference flow rate to the PI-flow control law, changing the choke valve opening. The auxiliary systems, being the mud circulation system (pumps), draw-works and choke valve, have been included as first-order transfer functions. The dynamics of these systems are not included in the NMPC prediction model.

Algorithm 3 NMPC

1: Initialization: $\bar{\mathbf{u}}_0, \hat{\mathbf{x}}_0, t_s, T_p, T_c$
2: **while** Run-time: **do**
3: $\quad$ Input: $\bar{\mathbf{u}}_{k-1}, \hat{\mathbf{x}}_k, \mathbf{y}_k$
4: $\quad$ **if** `mod`(time,t_s)$= 0$ **then**
5: $\quad\quad$ Solve the optimal control problem (49), with (45), and constraints from (50),(51), and (52a).
6: $\quad\quad$ **if** Convergence or max MPC iterations **then**
7: $\quad\quad\quad$ Apply first column of input vector: $\mathbf{u}_k = \bar{\mathbf{u}}_{k,1}$
8: $\quad\quad\quad$ Update $\bar{\mathbf{u}}_k$ by one time shift: $\bar{\mathbf{u}}_{k,[t_k+t_s, t_s N_p]}$ and pad last element with $\bar{\mathbf{u}}_{k,N_p-1}$ (Grune and Pannek, 2011)
9: $\quad\quad$ **else**
10: $\quad\quad\quad$ Try again with relaxed constraints: Reduce constraints to (52a) and (52d) and $\Delta \mathbf{u}_j$, $j = 0, \ldots, N_c$ from (51)
11: $\quad\quad$ **end if**
12: $\quad$ **else**
13: $\quad\quad$ Use previous sample-time input: $\bar{\mathbf{u}}_k = \bar{\mathbf{u}}_{k-1}$
14: $\quad$ **end if**
15: **end while**

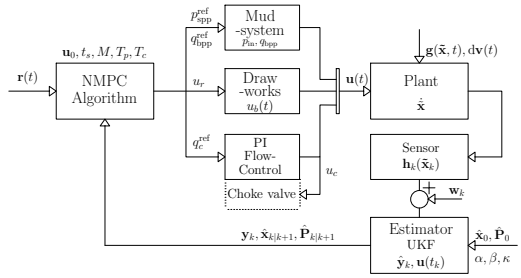

Figure 6: The simulation model. The NMPC prediction model comprises of the estimated plant model from (45), leaving the auxiliary system dynamics unknown.

6 Simulation study

The wellbore and DS system together with estimator and controller, were implemented in `MATLAB`. The primary goal of the study is to reduce surge and swab pressures while performing tripping, along with multi-target tracking of pressures in the annular wellbore. As seen in Figure 4, the surge pressures while RIH cause rapid fluctuations in the pressure states. The target is given as

$$p_{\text{n,L}} \leq p_{\text{n}}(t) \leq p_{\text{n,H}} \tag{54}$$

where the upper (H) and lower (L) bounds can represent the bottom-hole fracture and pore pressures, respectively.

As described in Gravdal et al. (2018), the system under consideration is limited in the sense of sensor measurements, time-delay, and under constant change due to geo-physical effects in the wellbore. We consider an ideal setting where measurements are not time-delayed and are aware that this effect may give a considerable performance decrease in the system identification and control of the pressure and flow in the wellbore.

The designed estimator and control configuration performance is tested in extensive simulation, with four case studies. The initial conditions in each case study are equal. The common system parameters are shown in Table 4, where the auxillary system time constants (see Section 5.1) are T_{dw}, T_{ch}, T_{bpp} and T_{spp}, denoting the draw-works, choke valve, stand-pipe pressure, and back-pressure pump, respectively.

Table 4: System parameters.

$\mathbf{g_z}$	$[0, 0, 0]^\top$	[-,-,-]
$\mathbf{g}_p, \mathbf{g}_q$	0.0025, 10	[-]
W_i	[1, 5, 10, 10]	[%]
$y_{i,\text{nom}}$	[1, 5, 10, 100]	[m, bar, bar, L min^{-1}]
$\mathcal{K}$	[0.0168, 1.2, 0.15]$^\top$	[-,-,-]
$c_{\text{eq}}, k_{\text{eq}}$	25.0, 563	[kN s m^{-1}, kN m^{-1}]
$k_{\text{ch},p}, k_{\text{ch},i}$	0.08, 2	[-, s]
$T_{\text{dw,ch,bpp,spp}}$	4, 2, 30, 5	[s]

All the case studies presented here are based on data from the test well in Table 2. The tuning for prediction, control horizon, sample-time and weighted set-point tracking $\mathbf{W}_c, \mathbf{R}_c$ are based on trial and error. However, we use scaling values, based on the nominal output values and the individual actuator range. Furthermore, tuning factors are used to adjust the weights given as

$$\mathbf{W}_{c,[i,i]} = \frac{\tilde{w}_{c,i}}{y^2_{i,\text{span}}}, \; \mathbf{R}_{c,[j,j]} = \frac{\tilde{r}_{c,j}}{u^2_{j,\text{span}}} \tag{55}$$

where $y_{i,\text{span}}$ is the span of the output set-point values, $u_{j,\text{span}}$ is the span of the input (actuator incremental change) and $\tilde{w}_{c,i}, \tilde{r}_{c,j}$ are tuning factors for the diagonal elements of $\mathbf{W}_c$ and $\mathbf{R}_c$, and $\mathbf{R}_r = \mathbf{R}_c$.

The simulation study is broken down in four case studies. The three first case studies compare the NMPC performance in three configurations, related to how model-errors and disturbances are handled. The first method is adopted from Kwakernaak and Sivan (1974, Chapter 3.7.2) for offset-free LQR, by augmenting the state vector with the tracking error given as

$$\tilde{\mathbf{x}} = \begin{bmatrix} \mathbf{z} \\ \mathbf{x}_1 \\ \mathbf{x}_2 \\ \mathbf{e} \end{bmatrix}, \; \mathbf{e} = \int_{t_0}^{t} \left(\begin{bmatrix} \mathbf{z} \\ \mathbf{x}_1 \\ \mathbf{x}_2 \end{bmatrix} - \begin{bmatrix} \mathbf{z}_{\text{ref}} \\ \mathbf{x}_{1,\text{ref}} \\ \mathbf{x}_{2,\text{ref}} \end{bmatrix} \right) \mathrm{d}\tau \tag{56}$$

where $\mathbf{e}$ is the integral error and $\mathbf{z}_{\text{ref}}, \mathbf{x}_{1,\text{ref}}, \mathbf{x}_{2,\text{ref}}$ are the desired state trajectory for the rig system, wellbore and drill-string states, respectively. The term $\mathbf{e}^\top \mathbf{Q}_c \mathbf{e}$ is included in (49), where $\mathbf{Q}_{c,[i,i]} = \tilde{q}_i \mathbf{W}_{c,[i,i]}$, with $\tilde{q}$ denoting the tuning factor.

The second method includes a disturbance state estimator as proposed in Pannocchia et al. (2015), yielding

$$\begin{aligned} \hat{\mathbf{x}}_k &= \mathbf{f}(\hat{\mathbf{x}}_{k-1}, \boldsymbol{\theta}_{k-1}, \mathbf{u}_{k-1}, \hat{\mathbf{d}}_{k-1}) + \mathbf{K}_x(\mathbf{y}_k - \hat{\mathbf{y}}_k) \\ \hat{\mathbf{d}}_k &= \hat{\mathbf{d}}_{k-1} + \mathbf{K}_d(\mathbf{y}_k - \hat{\mathbf{y}}_k) \end{aligned} \tag{57}$$

where $\mathbf{y}_k$ is the sampled measurement, $\hat{\mathbf{d}}_k$ is the estimated disturbance, and $\mathbf{K}_x$, $\mathbf{K}_d$ are the Kalman gains for the estimate error. The estimator design is chosen depending on the application. The advantage of including integration of the disturbance is to achieve integral control by capturing the model-mismatch between the real and estimated plant dynamics (Borrelli and Morari, 2007). The disturbance state is kept constant over the prediction horizon in the NMPC. The NMPC for Case 3 uses a linear disturbance model as

$$\begin{aligned} \mathbf{x}_{d,j+1} &= \mathbf{f}(\mathbf{x}_{d,j}, \mathbf{u}_j, \boldsymbol{\theta}_k) + \mathbf{A}_d \mathbf{d}_k \\ \mathbf{y}_{d,j} &= \mathbf{h}(\mathbf{x}_{d,j}) + \mathbf{C}_d \mathbf{d}_k \end{aligned} \tag{58}$$

where $\mathbf{A}_d$ and $\mathbf{C}_d$ are chosen such that the states are observable, which applies according to restricting the dimensions $\dim(n_d) \leq \dim(n_y)$, where n_d, n_y are the number of disturbance states and available measurements, respectively. As in Section 4, we utilize the UKF, and at NMPC sample-time an estimate of the $\mathbf{d}_k$ is given to the NMPC before solving the NLP. The NMPC-disturbance model setup is presented in Figure 7.

Furthermore, we implement a reference trajectory specified by the user to predict smooth changes over the horizon in the NMPC. The trajectory is given as

$$y^{\text{mpc,ref}}_{i,k+j} = \alpha^j_i y^{\text{mpc,ref}}_{i,k} + (1 - \alpha^j_i) y^{i,\text{sp}}_k \tag{59}$$

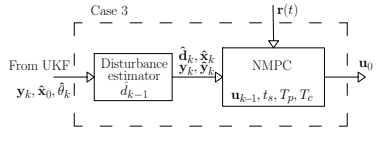

Figure 7: Case 3 NMPC with disturbance model.

where $y_{i,k}^{\text{mpc,ref}}$ is the reference trajectory value from the last sampling instant, $\alpha_i^j \in [0,1]$ is the smoothing coefficient, and $i \in [1,2,3]$. This allows for better model-mismatch compensation with a less aggressive controller (Qin and Badgwell, 2003).

A summary of the configurations are presented in Table 5.

Table 5: Simulation case studies.

Case	Description
1	NMPC0: No offset-free implementation
2	NMPC1: Integration of tracking error in prediction model, adding $\mathbf{e}_j^\top \mathbf{Q}_c \mathbf{e}_j$ to (49)
3	NMPC2: Including a disturbance model with, $(\mathbf{y}_{d,j} - \mathbf{y}_j^{\text{ref}})^\top \mathbf{W}_c (\mathbf{y}_{d,j} - \mathbf{y}_j^{\text{ref}})$.
4	NMPC1: Tracking of Δp and p_n

6.1 BHP and block position tracking in Case 1 to 3

The three first case studies comprise of BHP reference tracking and Δp band control while performing a POOH followed by a RIH sequence. Band control is initiated on Δp by setting the second diagonal element in $\mathbf{W}_c$ (and $\mathbf{Q}_c$, in Case 2) to zero. The NMPC and UKF parameters are presented in Table 6.

The choice of disturbance model for the NMPC is not obvious, and is left to the designer having knowledge over the process or measurement disturbances. The immediate disturbance for the hydraulic model is the fluctuations in $\mathbf{g}$, and model-mismatch in the NMPC. We use an input disturbance model for the configuration in NMPC2, were the fluctuations in x_{1,p_n}, i.e., the BHP state, is estimated. The choice is based on the disturbance from the DS heave on the BHP, which is counteracted by the flow rate from the drill-string in q_v.

In Table 6, the NMPC prediction model is discretized with intermediate step length of 0.1 s. A less strict constraint is enforced on Δp, which is allowed to vary between the lower bound of the BHP band, and Δp_L. The plots of Cases 2 and 3 are given in Figure 8.

For the simulations made in this paper, the biggest challenge of Case 1 was to compensate for the constant pressure change when tripping. From the top-most plot in Figure 8, NMPC1 is closer to achieve overall offset-free tracking of the BHP. The extra term included in minimizing the cost-function is tuned to achieve faster disturbance rejection. The NMPC1 is seen to deviate from the two others in how the choke flow and DS pressure is controlled. Since tripping out pipe reduces the pressure in the wellbore, the NMPC1 requires lower choke flow rate. To fulfill this, the PI flow controller reduces the choke opening in the first seconds of the sequence and the NMPC1 initiates an increase the stand-pipe pressure. The NMPC2 seems to require larger changes to the choke flow and DS pressure during tripping.

Table 6: Case 1–3 parameters. *[m,L/min,L/min,bar].

Cases 1–3		
$q_{\mathbf{z}}$	$[10^{-5}, 10^{-5}, 10^{-5}]$	[-]
$\mathbf{q}_{\mathbf{x}_1}$	$[g_{p_1}, g_{q_2}, \ldots, g_{q_n}, g_{p_n}]$	[-]
$\mathbf{q}_{\mathbf{x}_2}$	$[0.0025, 10]$	[-]
$\mathbf{q}_\theta$	$[10^4, 10^4, 10^4]^\top$	[-]
$\mathbf{Q}$	$\text{diag}([\mathbf{q}_{\mathbf{x}_1}, \mathbf{q}_{\mathbf{x}_2}, \mathbf{q}_\theta])$	[-]
$\mathbf{R}$	$\text{diag}(\boldsymbol{\sigma}_w^2)$	[-]
t_m, α_{ukf}	0.1, 1	[s,-]
t_s, M	1, 10	[s, -]
T_p, T_c	15, 3	[s,s]
α_i	[0.8 0.8 0.8]	[-]
$\tilde{r}_{c,j}$	[10, 1, 1, 10]	[-]
$\tilde{w}_{c,i}$	[10, 0, 50]	[-]
$\text{diag}(\mathbf{T})$	$[100, \ldots, 100, 500, 500]$	[-]
$y_{i,\text{span}}$	[14, 15, 20]	[m,bar,bar]
$u_{j,\text{span}}$	[18.5, 1500, 750, 32.5]	[]*
$\mathbf{u}_L$	$[-5, 0, 0, 5]^\top$	[]*
$\mathbf{u}_H$	$[32, 3000, 1500, 60]^\top$	[]*
$\Delta\mathbf{u}$	$[\pm 0.5, \pm 100, \pm 50, \pm 1]^\top$	[]*
$\Delta p_H, \Delta p_L$	$p_{n,L}, \Delta p^{\text{ref}} - 5$	[bar]
$p_{n,H}$,$p_{n,L}$	$p_n^{\text{ref}} \pm 2$	[bar]
$z_{2,L}, z_{2,H}$	± 0.5	[m s^{-1}]
Case 2: $\mathbf{Q}_c$	$\mathbf{W}_c \cdot 0.1$	[-]
Case 3:		
$\mathbf{Q}_{x,\text{ukf}}$	$\mathbf{Q}$	[-]
$\mathbf{Q}_{d,\text{ukf}}$	1	[-]
$\mathbf{R}_{\text{ukf}}$	$\mathbf{R}$	[-]
$\mathbf{A}_{d,x_{1,p_n}}$	1	[-]

All configurations are able to create a trajectory for the travelling block and meet the set-point. No noticeable requirements in flow rate were made to the back-pressure pump, by the NMPC0–2, seen in the fifth plot.

NMPC1 including the integrated tracking error is quicker in the response to changes in set-points. A disadvantage of this can be larger BHP spikes. This is also seen from NMPC2 configuration. However, further tuning of $\mathbf{Q}_c$ in the cost function can reduce this.

The estimated frictional pressure forces are presented in Figure 9. The estimated frictional pressure forces for the wellbore converges during steady-state and follows the trend of the true friction, seen for all the case studies. However, a noticeable bias is seen when rapid changes in the BHP is occuring.

Recall from (46) that we only assume to know the laminar klinging factor, and base the frictional law on a quadratic function. The true friction model is based on predicting the mud laminar and turbulent flow, with a transition rate. Hence, properties such as fluid yield stress is not accounted for in the estimated model. A

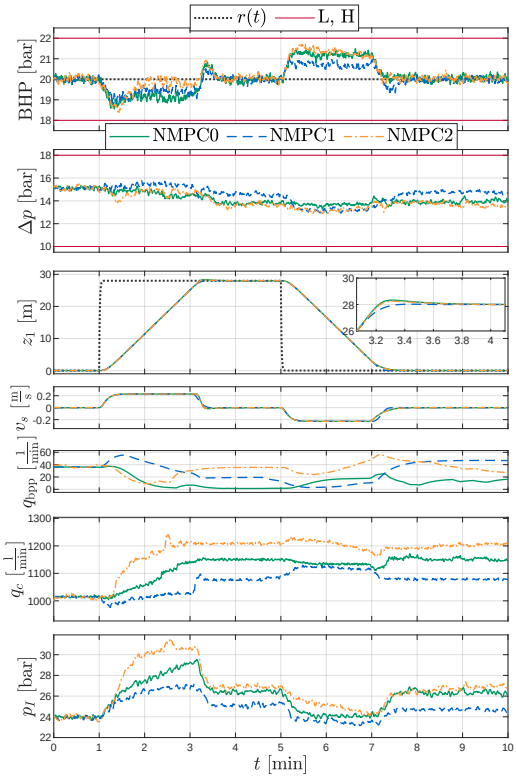

Figure 8: Tracking constant BHP and reference tajectory for travelling block.

result of that is that we get a bias, since we can get the correct magnitude and direction of the fluid effective velocity but must use θ_i with large variance to achieve a value in acceptable range for allowing pressure increase in the NMPC prediction model.

The root-mean-square values of the tracking error $e = \tilde{x} - x^{\text{ref}}$ (RMSE) for z_1 and p_n, summarizes the closed-loop performance of the three NMPC configurations. The values are given in Table 7 for comparison.

A general observation from the values in Table 7, is that NMPC1 configuration performs better than the two others with the smallest overall tracking error.

Table 7: Case 1–3, mean-of-error and RMSE values for e_{y_1}, e_{y_3}.

	E[e]		RMSE(e)	
C. 1	[-0.0459	0.0822]	[11.370	0.689]
C. 2	[-0.00438	-0.00538]	[11.377	0.464]
C. 3	[-0.03805	0.212]	[11.389	0.677]

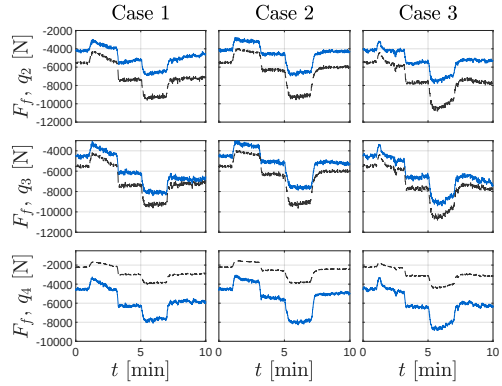

Figure 9: Case 1–3 frictional pressure forces. Solid blue lines denote the estimates and dashed black lines denote the true values.

However, the RMSE error is based on how quickly the controller meets the reference values, which disregards violation of critical constraints, overshoot limits, etc.

6.2 Multi-variable tracking in Case 4

The last case study comprises keeping both BHP and Δp in their band and at their respective set-points through a sequence of set-point adjustments, with the block reference at zero during the entire time. We choose the NMPC1 configuration, which showed the best results in terms of RMSE. The parameters for the NMPC in Case 4 are summarized in Table 8. The noise parameters are the same as in Table 3.

We set a steady-state input goal for the back pressure pump at 0 l/min, which is implemented by setting the third diagonal element of $\mathbf{R}_r$ nonzero in the cost function. This allows the NMPC to focus more on using the

Table 8: Case 4 parameters. *[m, L/min, L/min, bar].

t_s, M	1, 10	[s, -]
T_p, T_c	10, 5	[s,s]
α_i	[0.8 0.8 0.8]	[-]
$\tilde{r}_{c,i}$	[10, 1, 1, 10]	[-]
$\tilde{w}_{c,i}$	[1, 5, 10]	[-]
$y_{i,\text{span}}$	[14, 15, 20]	[m,bar,bar]
$u_{j,\text{span}}$	[18.5, 1500, 1000, 32.5]	[]*
diag($\mathbf{T}$)	$[100, \ldots, 100, 400, 400, 500, 500]$	[-]
$\mathbf{u}_L$	$[-5, 0, 0, 5]^\top$	[]*
$\mathbf{u}_H$	$[5, 3000, 2000, 80]^\top$	[]*
$\Delta\mathbf{u}$	$[\pm 0.5, \pm 100, \pm 50, \pm 1]^\top$	[]*
$\Delta p_H, \Delta p_L$	$\Delta p^{\text{ref}} \pm 3$	[bar]
$p_{n,H}, p_{n,L}$	$p_n^{\text{ref}} \pm 2$	[bar]
$z_{2,L}, z_{2,H}$	± 0.5	[m s^{-1}]
$\mathbf{Q}_c$	$\mathbf{W}_c \cdot 0.1$	[-]

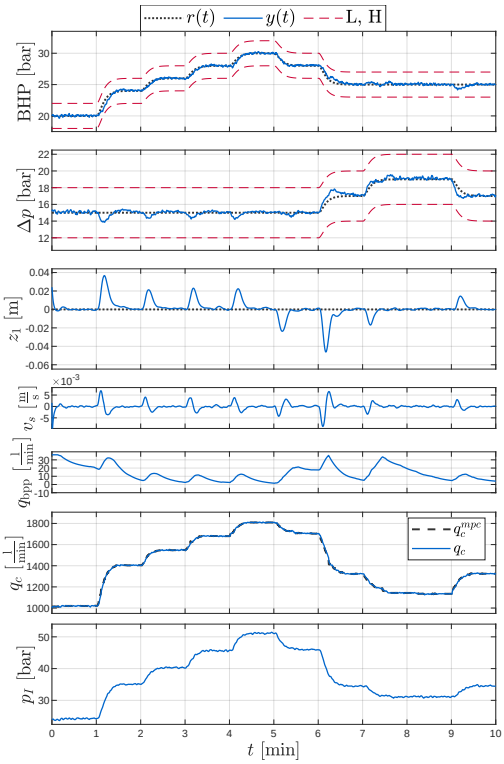

Figure 10: System response to tracking multiple setpoints.

main mud pump and choke to control the down hole pressures. The tracking result in Case 4 is presented in Figure 10.

Seen in plot 1–3 in Figure 10, the NMPC1 manages tracking of the three controlled variables, retrieving the block at zero position after using it for manipulating the BHP and Δp. The velocity of the DS is well below the constraint margins, seen in the fourth plot of Figure 10.

The estimated frictional pressure forces and the θ_i parameter are presented in Figure 11. The same covariance properties are used in the UKF for Cases 1–3.

Stepping through both the desired BHP and choke differential pressure values, NMPC1 manages to keep both in their respective bands by manipulating the stand-pipe pressure and choke flow. The RMSE of the tracking error in Case 4 is RMSE $= [0.00881, 0.322, 0.70039]$, which for e_3 is similar to the results in Case 1–3 (Table 7).

Since increasing the BHP has a lag effect on the upper volumes in the wellbore, the pressure wave must

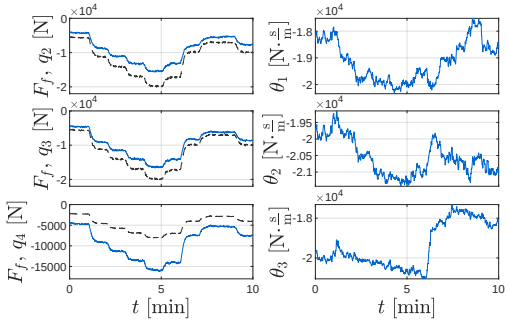

Figure 11: Case 4 frictional pressure forces and estimated parameter θ_i. Solid blue lines denote the estimates and dashed black lines denote the true values.

be compensated for in the choke while meeting the setpoint. As also shown in Møgster et al. (2013), control of multiple locations in the wellbore is an important feature of efficient MPD.

6.3 Discussion

6.3.1 Estimator performance

The variance of the estimated parameter θ_i and variance of the error for the calculated frictional pressure forces $e_i = F_{f,i} - \hat{F}_{f,i}$ are given in Table 9.

Table 9: Cases 1 to 4, mean and variance-of-error for estimator for $\hat{\theta}_i$, $\hat{f}_{1,i}, i = [2, 3, 4]$.

	$\mathrm{E}[(\theta_i - \bar{\theta}_i)^2]\cdot 10^6$	$\sigma^2 = \mathrm{E}[(e - \bar{e})^2]\cdot 10^5$
1:	[2.34 1.038 1.54]	[2.99 0.9035 3.64]
2:	[2.81 2.25 2.66]	[2.24 0.876 5.45]
3:	[1.32 0.385 0.4013]	[3.24 0.50305 4.42]
4:	[0.554 0.287 1.27]	[1.088 8.69 3.79]

From column two to four, the differences in magnitude of the variances for the estimated parameters are not large, indicating that the UKF is producing consistent estimates in the case studies. The UKF and NMPC use the same model, where the annular frictional pressure forces are treated as an unknown quadratic function. The bias in the UKF estimates can be explained by comparing the estimator model in (46) to the true first-principle fluid model from Gjerstad et al. (2013) relying on q_i and v_s. If the friction force bias becomes too large, the Kalman gain might not be sufficient to correct the predicted output and produce reliable estimates of the flow rates and pressures in the UKF.

6.3.2 NMPC tuning and constraints

For the NMPC configurations shown in this paper, the initial tuning has been based on trial and error with process span variables. The estimator bias due to predicted frictional pressure forces is a challenge in terms of increased prediction error over the horizon, and must be accounted for when performing the tuning of T_p and M. A more accurate prediction model would allow for a longer NMPC horizon.

Comparing the three different designs, NMPC0–2, the nominal design in NMPC0 yields less tuning variables, and tracking gives acceptable results in our case studies. However, with knowledge of disturbances in the system (such as sudden inflow from formation) we can achieve a better design with NMPC1 and NMPC2 by the advantage of the integrated error states or estimation of the disturbance state.

A measure of improving trajectory control is to include a full reference path for the hoisting (which can be a smooth 2nd-order polynomial for example) such that the NMPC follows this precisely. Then, the velocity constraint can be removed and the controller only requires three degrees of freedom for keeping BHP at its reference. The implementation in this work used position control for the travelling block. In practice, the driller adjusts the block velocity, and the block travelling limits are set by the operator in advance (Lyons et al., 2015).

6.3.3 Controller implementation robustness

Robustness measures in terms of the implementation has been done, such as iterating over a fixed horizon until either a limit is met or the MPC converges. This is done in an ad-hoc way, to at least ensure that more than one iteration is performed by the optimization algorithm.

6.3.4 Simulation performance

An averaged of 16.4 s for each NMPC NLP iteration was logged during the simulation study (Case 1 NMPC0). The sampling time was 1 s, as such, the goal of convergence in that time is not met. The corresponding real-time factor (RTF), given as $\text{RTF} = t_{\text{actual}}/t_{\text{sim}}$, was 17.44 for a total of 10 minutes simulation time.

Optimal conditions for real-time applications is when $\text{RTF} < 1$. The NMPC does not achieve real-time performance for the presented algorithm. We are aware of better methods of solving the optimization problem, but as a first implementation MATLABs `fmincon` gives an easy way for organizing the NMPC algorithm.

7 Conclusion

In this work, we have presented a multi-purpose control system used to minimize surge and swab pressures while tripping in an offshore well, along with tracking of choke differential pressure and BHP. The wellbore fluid frictional pressure forces was parametrized by a quadratic function in flow-rate and DS velocity. The unknown parameters in this function were estimated using an UKF, which also estimated the system states used by a NMPC. The NMPC manipulated the inputs to the back-pressure flow and stand pipe pressure directly, set the reference trajectory for a linear state-integrator controlling the block positioning system, and supplied a PI choke flow controller with desired reference flow. The actuator dynamics for the block, choke, back-pressure flow, and mud pump pressure were represented by first-order linear low-pass filters.

We have presented the results from comparing three NMPC configurations where two of these included measures to improve offset-free tracking. The best result in terms of RMSE values was achieved by NMPC1, with integrated tracking error implemented in the cost function. All three NMPC configurations showed good results in terms of constraining the BHP inside the desired envelope and at the set-point, while tripping.

For multi-target tracking, the NMPC was configured with a shorter prediction horizon and longer control horizon with a steady-state input goal for the back-pressure pump. NMPC1 was used in this case study. Controlling both BHP and choke differential pressure was accomplished by the controller.

Since we used an SDE with RK4 Maruyama in time integration, average fluctuations were included. For the configurations and case-studies presented here, the NMPC has shown to be robust towards model-mismatch and variations in the states due to the nature of the SDE.

Including the dynamics of a hoisting system we can predict and constrain the estimated DS velocity to both manipulate the BHP and prevent excessive surge and swab pressures. The system presented in this paper is then automated such that the driller is only required to supply the desired reference points for BHP, choke differential pressure and travelling block position.

Acknowledgments

We would like to thank Dr. Kristian Gjerstad for helpful comments regarding the hydraulic model. The research presented in this paper has received funding from the Norwegian Research Council, SFI Offshore Mechatronics, project number 237896.

References

Black, A. D., Walker, B. H., Tibbitts, G. A., and Sandstrom, J. L. PDC Bit Performance for Rotary, Mud Motor, and Turbine Drilling Applications. *SPE Drilling Engineering*, 1986. 1(06):409–416. doi:10.2118/13258-PA.

Borrelli, F. and Morari, M. Offset free model predictive control. *Proceedings of the IEEE Conference on Decision and Control*, 2007. pages 1245–1250. doi:10.1109/CDC.2007.4434770.

Breyholtz, O., Nygaard, G., Godhavn, J.-M., and Vefring, E. H. Evaluating control designs for co-ordinating pump rates and choke valve during managed pressure drilling operations. In *2009 IEEE Control Applications,(CCA) & Intelligent Control,(ISIC)*. IEEE, pages 731–738, 2009. doi:10.1109/CCA.2009.5281013.

Breyholtz, Ø., Nygaard, G., Siahaan, H., and Nikolaou, M. SPE 128151 Managed Pressure Drilling : A Multi-Level Control Approach. *SPE Intelligent Energy Conference and Exhibition*, 2010. doi:10.2118/128151-MS.

Breyholtz, Ø. and Nygaard, O. G. H. Deep Water Drilling: Full Pressure Profile Control in Open Hole Section Utilizing Model Predictive Control. *International Petroleum Technology Conference*, 2009. doi:10.2523/13256-MS.

Brown, R. G. and Hwang, P. Y. C. *Introduction to Random signals and Applied Kalman Filtering with MATLAB exercises*. Wiley, 4th edition, 2012.

Cayeux, E., Daireaux, B., and Dvergsnes, E. W. Automation of Drawworks and Topdrive Management To Minimize Swab/Surge and Poor-Downhole-Condition Effects. *IADC/SPE Drilling Conference and Exhibition*, 2010. 26(4):557–568. doi:10.2118/128286-MS.

Cayeux, E., Daireaux, B., Dvergsnes, E. W., Florence, F., and Varco, N. O. Toward Drilling Automation : On the Necessity of Using Sensors That Relate to Physical Models. *SPE Drilling & Completion*, 2014. (March 2013):5–7. doi:10.2118/163440-PA.

Chen, C.-T. *Linear System Theory and Design*. Oxford University Press, Inc., 2013.

Chirikjian, G. S. *Stochastic Models Information Theory and Lie Groups, Volume 1: Classical Results and Geometric Methods*. Springer Science & Business Media, 2009.

Downton, G. C. Challenges of modeling drilling systems for the purposes of automation and control. *IFAC Proceedings Volumes (IFAC-PapersOnline)*, 2012. 1(PART 1):201–210. doi:10.3182/20120531-2-NO-4020.00054.

Egeland, O. and Gravdahl, J. T. *Modeling and Simulation for Automatic Control*, volume 76. Marine Cybernetics Trondheim, Norway, 2002.

Findeisen, R. and Allgoewer, F. An Introduction to Nonlinear Model Predictive Control. *Control, 21st Benelux Meeting on Systems and Control*, 2002. (January 2002):1–23. doi:10.1167/iovs.06-0923.

Gjerstad, K., Time, R. W., and Bjorkevoll, K. S. A Medium-Order Flow Model for Dynamic Pressure Surges in Tripping Operations. *SPE/IADC Drilling Conference*, 2013. doi:10.2118/163465-MS.

Godhavn, J.-M. Control Requirements for High-End Automatic MPD Operations. *SPE/IADC Drilling Conference and Exhibition*, 2009. 25(March):336–345. doi:10.2118/119442-MS.

Gravdal, J., Lorentzen, R., Fjelde, K., and Vefring EH. Tuning of computer model parameters in managed pressure drilling applications using an unscented kalman filter technique. *SPE Journal*, 2010. 15(03):856–866. doi:10.2118/97028-MS.

Gravdal, J. E., Siahaan, H., and Bjørkevoll, K. S. Limiting Factors for the Ability to Achieve Accurate Pressure Control in Long Wells. *Modeling, Identification and Control: A Norwegian Research Bulletin*, 2018. 39(2):115–129. doi:10.4173/mic.2018.2.6.

Grune, L. and Pannek, J. *Nonlinear Model Predictive Control: Theory and Algorithms*. Springer, 2011.

Haug, A. J. *Bayesian estimation and tracking: a practical guide*. John Wiley & Sons, 2012.

Hermann, R. and Krener, A. J. Nonlinear Controllability and Observability. *IEEE Transactions on Automatic Control*, 1977. 22(5):728–740. doi:10.1109/TAC.1977.1101601.

Julier, S. J. and Uhlmann, J. K. New Extension of the Kalman Filter to Nonlinear Systems. In *Proc. SPIE 3068, Signal Processing, Sensor Fusion, and Target Recognition VI*, volume 3. Orlando, FL, pages 182–193, 1997. doi:10.1117/12.280797.

Kaasa, G.-o., Stamnes, Ø. N., Aamo, O. M., and Imsland, L. Simplified hydraulics model used for intelligent estimation of downhole pressure for a managed-pressure-drilling control system. *SPE Drilling & Completion*, 2012. 27(01). doi:10.2118/143097-PA.

Khalil, H. K. Nonlinear Systems. *Prentice-Hall, New Jersey*, 1996. 2(5):1–5.

Kou, R. S., Elliott, L. D., and Tarn, J. T. Observability of Nonlinear System. *Information and Control*, 1973. 99:89–99.

Kwakernaak, H. and Sivan, R. Linear Optimal Control Systems. *IEEE Transactions on Automatic Control*, 1974. 19(5):631–632. doi:10.1109/TAC.1974.1100628.

Landet, I. S., Mahdianfar, H., Aarsnes, U. J. F., Pavlov, A., and Aamo, O. M. Modeling for MPD Operations with Experimental Validation. *IADC/SPE Drilling Conference and Exhibition*, 2012. doi:10.2118/150461-MS.

Lyons, W., BS Plisga J, G., and Lorenz, M. *Standard Handbook of Petroleum and Natural Gas Engineering*. Gulf Professional Publishing, 3rd edition, 2015.

Meglio, F. D. and Aarsnes, U. J. F. A distributed parameter systems view of control problems in drilling. *IFAC-PapersOnLine*, 2015. 48(6):272–278. doi:10.1016/j.ifacol.2015.08.043.

Møgster, J., Godhavn, J. M., and Imsland, L. Using MPC for managed pressure drilling. *Modeling, Identification and Control*, 2013. 34(3):131–138. doi:10.4173/mic.2013.3.3.

Nandan, A. and Imtiaz, S. Nonlinear model predictive control of managed pressure drilling. *ISA Transactions*, 2017. 69:307–314. doi:10.1016/j.isatra.2017.03.013.

Nygaard, G., Nævdal, G., and Mylvaganam, S. Evaluating nonlinear kalman filters for parameter estimation in reservoirs during petroleum well drilling. *Proceedings of the IEEE International Conference on Control Applications*, 2006. pages 1777–1782. doi:10.1109/CACSD-CCA-ISIC.2006.4776910.

Nygaard, G. H., Imsland, L. S., and Johannessen, E. A. Using NMPC based on a low-order model for controlling pressure during oil well drilling. *IFAC Proceedings Volumes (IFAC-PapersOnline)*, 2007a. 40(5):159–164. doi:10.3182/20070606-3-MX-2915.00025.

Nygaard, O. G. H., Johannessen, E. A., Gravdal, J. E., and Iversen, F. Automatic Coordinated Control of Pump Rates and Choke Valve for Compensating Pressure Fluctuations During Surge-and-Swab Operations. *IADC/SPE Managed Pressure Drilling and Underbalanced Operations Conference & Exhibition*, 2007b. doi:10.2118/108344-MS.

Pannocchia, G., Gabiccini, M., and Artoni, A. Offset-free MPC explained: Novelties, subtleties, and applications. *IFAC-PapersOnLine*, 2015. 48(23):342–351. doi:10.1016/j.ifacol.2015.11.304.

Pedersen, T., Aarsnes, U. J. F., and Godhavn, J.-m. Flow and pressure control of underbalanced drilling operations using NMPC. *Journal of Process Control*, 2018. 68:73–85. doi:10.1016/j.jprocont.2018.05.001.

Qin, S. J. and Badgwell, T. A. A survey of industrial model predictive control technology. *Control Engineering Practice*, 2003. 11(7):733–764. doi:10.1016/S0967-0661(02)00186-7.

Rasmussen, O. and Sangesland, S. Evaluation of MPD Methods for Compensation of Surge-and-Swab Pressures inFloating Drilling Operations. 2007. doi:10.2523/108346-ms.

Rößler, A. Runge-Kutta methods for Itô stochastic differential equations with scalar noise. *BIT Numerical Mathematics*, 2006. 46(1):97–110. doi:10.1007/s10543-005-0039-7.

Slotine, J.-J. E. and Weiping, L. *Applied Nonlinear Control*. Prentice Hall International Inc., New Jersey, 1991.

Stakvik, J. Å., Berg, C., Kaasa, G.-O., Aamo, O. M., and Lehner, U. Adaptive Model Based Choke Control System for MPD Operations. *SPE/IADC Managed Pressure Drilling and Underbalanced Operations Conference and Exhibition*, 2016. pages 1–11. doi:10.2118/179714-MS.

Stamnes, Ø. N., Zhou, J., Kaasa, G. O., and Aamo, O. M. Adaptive Observer Design for the Bottomhole Pressure of a Managed Pressure Drilling System. *Proceedings of the IEEE Conference on Decision and Control*, 2008. pages 2961–2966. doi:10.1109/CDC.2008.4738845.

Whittaker, A. and EXLOG Staff. *Theory and Application of Drilling Fluid Hydraulics*. D. Reidel Publishing Company, 1985.

Zhou, J. Control of of Bottom Bottom Hole Control of Pressure during Oil Well Drilling. *IFAC-PapersOnLine*, 2018. 51(4):166–171. doi:10.1016/j.ifacol.2018.06.060.

Paper II

Component-based Modeling and Simulation of Nonlinear Drill-String Dynamics

N. K. Tengesdal, C. Holden, and E. Pedersen.
Component-based Modeling and Simulation of Nonlinear Drill-String Dynamics
2021, 2nd revision submitted to Journal of Offshore Mechanics and Arctic Engineering (JOMAE).

This journal article is a revised and extended version of the previously published paper in [102].

This paper is awaiting publication and is not included in NTNU Open.

Paper III

Modeling of Drill String Dynamics in Deviated Wells for Real-Time Simulation

N. K. Tengesdal, G. Fotland, C. Holden, and B. Haugen.
Modeling of Drill String Dynamics in Deviated Wells for Real-Time Simulation
2021, Submitted to *SIMULATION: Transactions of The Society for Modeling and Simulation International*.

Paper IV

A Discussion on the Decoupling Assumption of Axial and Torsional Dynamics in Bit-rock Models

N. K. Tengesdal, S. Hovda, and C. Holden.
A Discussion on the Decoupling Assumption of Axial and Torsional Dynamics in Bit-rock Models
2021, Journal of Petroleum Science and Engineering, Vol. 202.

Errata

Note that in (45), the third term of the Taylor expansion is expressed incorrectly. The correct equation is given as

$$\theta_n(\tau-\tau_n) \approx \theta_n(\tau)-\tau_n\dot{\theta}_n(\tau)+\frac{1}{2}\tau_n^2\ddot{\theta}_n(\tau)+\text{H.O.T.} \tag{IV.1}$$

where H.O.T. denotes the higher order terms in the series expansion.

Journal of Petroleum Science and Engineering 202 (2021) 108070

Contents lists available at ScienceDirect

Journal of Petroleum Science and Engineering

journal homepage: http://www.elsevier.com/locate/petrol

A discussion on the decoupling assumption of axial and torsional dynamics in bit-rock models

Njål Kjærnes Tengesdal [a,1,*], Sigve Hovda [b], Christian Holden [a]

[a] Department of Mechanical and Industrial Engineering, Norwegian University of Science and Technology, Richard Birkelandsvei 2b, 7491, Trondheim, Norway
[b] Department of Geoscience and Petroleum, Norwegian University of Science and Technology, S. P. Andersen veg 15a, 7031, Trondheim, Norway

ARTICLE INFO

Keywords:
Drill string dynamics
Vibrations
Bit-rock models
Delay-differential equations
Stability

ABSTRACT

A common strategy for analyzing the stability of coupled axial and torsional dynamics in drilling is by using a two-degree-of-freedom mass-spring-damper model derived as a second-order ordinary differential equation. This implies using a single point mass to represent the inertia of the bottom-hole assembly and thus the characteristics of an otherwise distributed system. For the bit-rock model developed in Richard et al. (2007), the stability characteristics of the drilling system are in many previous works derived by assuming that the axial dynamics can be decoupled from the slower torsional dynamics. Using this bit-rock model, the friction forces and torques in the system are dependent on a time-delay term, dictating the stability of the system. Consequently, a set of critical drilling parameters, i.e., rotation speed, drill string stiffness, and fluid damping, can be investigated to identify the properties of the equilibrium for the nominal solution.

In this paper, we have generalized the drill string dynamics by modeling the drill string as a series of alternating springs and point masses. By making the same assumptions as in previous works, the dynamics are derived as a lumped-multi-element second-order model including a time-delay dependent on the system states. The model is then defined as a state-dependent delay differential equation. The stability analysis of the decoupled generalized system indicates that the stable region for the chosen drilling parameters reduces and is trending towards zero when the number of model elements increases. The implication of this is that the nonlinearity of the coupled axial and torsional dynamics is required for a thorough understanding of the stability of the drilling system. Furthermore, we have performed a numerical analysis of the coupled dynamics by simulating relevant drilling scenarios.

1. Introduction

Major limitations in oil & gas drilling are due to mechanical vibrations of the drill string. The axial, torsional and lateral vibration can, in combination or alone, result in extensive wear or failure of the drill string components (Ghasemloonia et al., 2015).

The axial vibration domain has received special attention in previous work, due to drag bits being equipped with fixed blades are prone to self-excited axial vibrations. This phenomenon is being explained to originate from the regenerative cutting process at the bit (Dareing et al., 1990). Self-excited vibrations result from an unstable equilibrium point of the system, and might eventually result in axial bit bouncing and torsional stick-slip cycles (Saldivar et al., 2016). The understanding is that the axial dynamics are coupled with the angular displacement of the bit, interacting with the formation during the process of removing rock (Ghasemloonia et al., 2015).

Mathematical modeling has proven useful for predicting steady-state and transient response of drill string dynamics, and relates well to field measurement (Ghasemloonia et al., 2015; Jogi et al., 2002). To address the causes of instability such as self-excited vibrations and stick-slip while drilling vertical wellbores, the dynamics of the drill string is commonly described by a two degree-of-freedom model for the axial and torsional vibrations (Bakhtiari-Nejad and Hosseinzadeh, 2017; Besselink et al., 2011; Depouhon and Detournay, 2014; Gupta and Wahi, 2016; Richard et al., 2004). The dynamic coupling between the rock and the drill string model is then confined to the drill bit.

Bit-rock models have been derived to investigate the nature of the contact between the drill bit and the formation being drilled. Typical bit-

* Corresponding author.
E-mail addresses: njaal.tengesdal@ntnu.no (N.K. Tengesdal), sigve.hovda@ntnu.no (S. Hovda), christian.holden@ntnu.no (C. Holden).
[1] All correspondence is directed to this author.

https://doi.org/10.1016/j.petrol.2020.108070
Received 26 June 2020; Received in revised form 17 October 2020; Accepted 20 October 2020
Available online 3 November 2020

rock models for drilling systems are static plus Coulomb friction where the friction coefficient is dependent on the relative velocities of the surfaces in contact, e.g., modelled by the Stribeck effect (Navarro-Lopez and Suarez, 2004; Canudas-de Wit et al., 2008). The torque and weight on bit (WOB) are then given by the instantaneous angular and axial velocity of the bit (Christoforou and Yigit, 2003).

On the basis of the work done in (Detournay and Defourny, 1992) along with relating rock cutting to metal machine cutting processes (Faassen et al., 2003; Insperger et al., 2005), a state-dependent time--delay to describe the bit-rock interaction with drag bits was first introduced in Richard et al. (2004) and extensively analysed in Richard et al. (2007). Furthermore, the axial and torsional dynamics were then coupled by a delayed rotational cutting motion of the bit. A motivation for introducing this bit-rock model was that the forces and moments generated at the bit was argued to be a function of the characteristics of the entire drilling system, described by rate-independent bit-rock laws (Detournay et al., 2008). The dynamic model describing the drilling system is then defined as state-dependent delay differential equation (SDDE), being a sub-category of retarded functional differential equation (RDE) systems (Agarwal et al., 2014; Richard, 2003).

Stability analysis of SDDE systems is critical to investigate the system limitations. The explicit nature of the time-delay yields an infinite-dimensional solution space, and requires definition of the past time-history (Richard, 2003). The feedback of the delay can in some cases both stabilize and destabilize the system. Methods of characterizing stability in linear time-invariant delay systems are well known (Walton and Marshall, 1987; Wang and Hu, 2000).

Modeling of drill strings are divided into full distributed descriptions and lumped element models in terms of second-order ordinary differential equations (ODE) for approximating the continuum dynamics. Lumped models, where the distributed effects are lumped to massless springs and point masses, are preferred due to simplified representations, capability of real-time performance, and development of control laws.

Lumped single-element models are used in previous work for characterizing the stability of a drilling system governed by axial and torsional dynamics. Due to the evidently faster axial vibrations as compared to the slow torsional vibrations, a common approach is to decouple the two vibration domains and analyze the faster axial stability independently. Pioneering work on the topic of stability for single-element models are found in Germay et al., 2005, 2009b, Richard et al., 2004, 2007 (without axial compliance), and Besselink et al., 2011, 2016 (both including the axial compliance). From these models, it is found that the axial vibrations is the driving factor for generating torsional vibrations. In these models, the continuum properties are thus approximated by a single mass point. Furthermore, viscous damping for the torsional system was not accounted for in these models.

More recent approaches involving lumped single element SDDE models for analysing the coupled stability are found in (Depouhon and Detournay, 2014; Gupta and Wahi, 2016; Nandakumar and Wiercigroch, 2013). In (Nandakumar and Wiercigroch, 2013), practically achievable operating points are discussed and compared to the analysis done in (Besselink et al., 2011). The model derived in (Gupta and Wahi, 2016) is a coupled single element ODE with partial differential equations (PDE) describing the cutting surface, included to properly address the situation of axial bit-bounce.

In terms of modeling the distributed drill string dynamics including the bit-rock model from (Richard et al., 2007), a numerical analysis of a finite-element-model is given in Germay et al. (2009a), and Bakhtiari-Nejad and Hosseinzadeh (2017) and Aarsnes and van deWouw (Aarsnes and van de Wouw, 2018) conducted a comprehensive stability analysis for the axial and torsional dynamics. In the latter, a Laplace transformation was performed to obtain a transmission line model to describe the distributed properties. Furthermore, in (Aarsnes and van de Wouw, 2018) it was stressed that higher-order models are necessary for conducting stability analysis.

For lumped parameter systems used for estimating mechanical vibrations, the natural frequencies tend towards the continuum properties when the number of lumped elements increase. The approximation of the continuum properties are thus limited by the number of included elements, as compared to directly working with the partial differential equations describing the distributed properties. Due to the complex geometry of the drill string, several different waves will travel in the assembly, having an impact on the stability regions. In machine milling, experiments show that higher-order models are necessary for accurate prediction of the cutting motion (Faassen et al., 2003).

In this paper, we extend the analysis of axial stability with a second-order lumped-multi-element model and investigate the coupled transient response for the axial and torsional dynamics. With increasing demand on simple yet reliable drill string models for estimating vibrations implemented in real-time drilling optimization applications, the use of lumped-multi-element models become important (see e.g. (Cayeux, 2018), in torque and drag analysis) (Florence and Iversen, 2010).

The dynamic drill string model developed in this work is similar to the axial and torsional multi-element models in (Hovda, 2018a, 2018b) used for off-bottom vibration analysis. As such, we extend these works to on-bottom analysis using the bit-rock model from (Richard et al., 2007). Hence, viscous damping is included considering skin-friction arising from the mud-flow in the annulus.

The analysis on the model in this paper shows that the decoupled axial stability region are significantly reduced when higher order models are used. This implies that when approaching the continuum properties with lumped-multi-element models, the decoupled stability region tends towards zero. The nonlinear coupled effects are then required when discussing the stability of the axial and torsional drilling system. Furthermore, drilling parameters such as critical rotation speed and axial velocity linked to system stability can be identified and tuned in drilling optimization (Florence and Iversen, 2010).

The model derivation is presented in Section 2. A decoupled stability analysis of the axial dynamics is performed in Section 3, with the results given for six drill string configurations being presented in Section 4. These results are investigated in a simulation study in Section 5. A discussion is given in Section 6, before the paper is concluded in Section 7.

2. Modeling

The wellbore is assumed to be vertical, simplifying the dynamics of the drill string model. The model for a lumped-element drill string is shown in Fig. 1, with individual mass points (blocks) separated by massless springs. The top boundary conditions are the travelling block position $U(t)$ where $U(0) = 0$ is assumed, and the angular displacement at the top of the drill string, $\Phi(t)$ where $\Phi(0) = 0$, given by the top drive. Positive top drive rotation is assumed to be clockwise.

Using a one-dimensional coordinate system, with z-axis defined positive downwards, we define each block with the generalized coordinate $u_i(t)$ and $\phi_i(t)$, representing axial and angular displacement of a model block. Each of the model blocks represent either drill pipe (DP) or the bottom-hole assembly (BHA) of the drill string. The BHA contains drill collars (DC)–being thick-walled, heavy and much stiffer pipes – bit and other tools facilitating the drilling process. The model representation is drawn from (Hovda, 2018b).

2.1. Axial drill string dynamics

Using a Newtonian framework, the equation of motion for the axial dynamics are given as

$$\begin{aligned} 0 &= -m_1\ddot{u}_1 - k_1(u_1 - U) + k_2(u_2 - u_1) - d_1\dot{u}_1 + gm_1F_{b,1} \\ 0 &= -m_i\ddot{u}_i - k_i(u_i - u_{i-1}) + k_{i+1}(u_{i+1} - u_i) - d_i\dot{u}_i + gm_iF_{b,i} \\ &\vdots = \vdots \\ 0 &= -m_n\ddot{u}_n - k_n(u_n - u_{n-1}) - d_n\dot{u}_n + gm_nF_{b,n} - W_c - W_f \end{aligned} \tag{1}$$

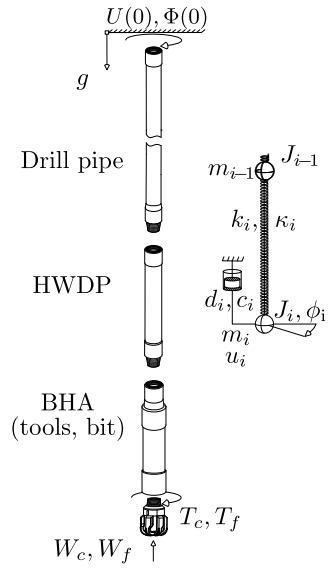

Fig. 1. Model representation of a drill string assembly, where BHA – bottom-hole assembly, and HWDP – heavy-weight drill pipe.

where $m_i = \rho_s A_i h$ is the mass of the block, ρ_s is the material density, A_i is the block cross-sectional area, $h = L/n$, is the height between the block sections, L is the unstretched drill string length, n is the number of included blocks (lumped elements), u_i is the position of the ith block, $U(t)$ is the position of the travelling block, $k_i = EA_i/h$ is the stiffness of the drill pipe for each section, E is the Young's modulus, d_i is the viscous drag force coefficients from the drilling mud in the annulus, g is the acceleration of gravity and $F_{b,n}$ is the buoyancy factor for each block, W_c is the weight on bit from the cuttings acting on the bit in the borehole, and W_f is the frictional forces from the bit wear flats in contact with the rock bottom.

Using vector notation, the axial dynamics are rearranged, yielding

$$\mathbf{M}\ddot{\boldsymbol{u}}(t) + \mathbf{D}\dot{\boldsymbol{u}}(t) + \mathbf{K}\boldsymbol{u}(t) - \boldsymbol{g} = \boldsymbol{t}_1 F(t) - \boldsymbol{t}_2 f_{\text{bit}}(t) \tag{2}$$

where $F(t) = k_1 U(t), f_{\text{bit}} = W_c + W_f$. The vectors and matrices of (2) are defined as

$$\mathbf{M} = \text{diag}(m_1, \dots, m_n),\ \mathbf{D} = \text{diag}(d_1, \dots, d_n)$$

$$\mathbf{K} = \begin{bmatrix} (k_1+k_2) & -k_2 & 0 & \dots & 0 & 0 \\ -k_2 & (k_2+k_3) & -k_3 & \dots & 0 & 0 \\ \vdots & \vdots & \ddots & & \vdots & \vdots \\ 0 & \dots & 0 & -k_{n-1} & (k_{n-1}+k_n) & -k_n \\ 0 & \dots & 0 & & -k_n & k_n \end{bmatrix}$$

$$\boldsymbol{g} = \begin{bmatrix} g m_1 F_{b,1} \\ \vdots \\ g m_n F_{b,n} \end{bmatrix},\ \boldsymbol{t}_1 = \begin{bmatrix} 1 \\ 0_{n-1,1} \end{bmatrix},\ \boldsymbol{t}_2 = \begin{bmatrix} 0_{n-1,1} \\ 1 \end{bmatrix}$$

where $\boldsymbol{u} = [u_1, u_2, \dots, u_n]^\top$, and $\mathbf{K}$ is defined as a *tridiagonal* matrix (Hovda, 2018b). The vectors $\boldsymbol{t}_1$ and $\boldsymbol{t}_2$ are by definition considered as projection vectors for the external forces and torques.

The drag forces due to mud flow in the annulus is derived in (Hovda, 2018b), accounting for the skin friction from the pipe, and assuming a laminar flow profile around the pipe through Newtonian annular Couette-Poiseuille flow. The d_i coefficients are given as

$$d_i = 2\pi h\mu \left(\frac{1+\alpha_i^2}{1-\alpha_i^2} \ln \alpha_i^{-1} - 1 \right)^{-1} \tag{3}$$

where μ is the viscosity of the fluid and $\alpha_i = r_{\text{o},i}/r_{\text{bh}}$ is the outer pipe diameter-to-holesize fraction with $r_{\text{o},i}$ being the outer pipe radius, and r_{bh} is the radius of the borehole.

2.2. Torsional drill string dynamics

The equations of motion for the torsional dynamics are given as

$$\begin{aligned} 0 &= -J_1\ddot{\phi}_1 - \kappa_1(\phi_1 - \Phi) + k_2(\phi_2 - \phi_1) - c_1\dot{\phi}_1 \\ 0 &= -J_i\ddot{\phi}_i - \kappa_i(\phi_i - \phi_{i-1}) + \kappa_{i+1}(\phi_{i+1} - \phi_i) - c_i\dot{\phi}_i \\ &\vdots = \vdots \\ 0 &= -J_n\ddot{u}_n - \kappa_n(\phi_n - \phi_{n-1}) - c_n\dot{\phi}_n - T_c - T_f \end{aligned} \tag{4}$$

where $J_i = \rho_s h I_{z,i}$ is the ith block moment of inertia, $I_{z,i} = \pi(r_{\text{o},i}^4 - r_{\text{i},i}^4)/2$ is the second moment of area, $r_{\text{i},i}$ is the inner radius of the block, ϕ_i is the angular position of the block, $\Phi(t)$ is the top-of-string angular displacement given by the top drive, $\kappa_i = GI_{z,i}/h$ is the torsional stiffness of the pipe or collar, c_i is the drag forces coefficient from drilling mud, T_c is the torque on bit due to cutting effect from the interaction between the cutter blade and the formation, and T_f is the frictional torque on bit from the underside of the cutter blades.

Similarly as in Section 2.1, we rearrange and represent the torsional dynamics in vector format, given as

$$\mathbf{J}\ddot{\boldsymbol{\phi}}(t) + \mathbf{C}\dot{\boldsymbol{\phi}}(t) + \boldsymbol{\mathcal{K}}\boldsymbol{\phi}(t) = \boldsymbol{t}_1 T(t) - \boldsymbol{t}_2 t_{\text{bit}}(t) \tag{5}$$

where $T(t) = \kappa_1\Phi(t)$, $t_{\text{bit}} = T^c + T^f$, and the matrices are defined as

$$\mathbf{J} = \text{diag}(J_1, \dots, J_n),\ \mathbf{C} = \text{diag}(c_1, \dots, c_n)$$

$$\boldsymbol{\mathcal{K}} = \begin{bmatrix} (\kappa_1+\kappa_2) & -\kappa_2 & 0 & \dots & 0 & 0 \\ -\kappa_2 & (\kappa_2+\kappa_3) & -\kappa_3 & \dots & 0 & 0 \\ \vdots & \vdots & \ddots & & \vdots & \vdots \\ 0 & \dots & 0 & -\kappa_{n-1} & (\kappa_{n-1}+\kappa_n) & -\kappa_n \\ 0 & \dots & 0 & & -\kappa_n & \kappa_n \end{bmatrix}$$

From the shear stresses in the fluid, c_i represent the coefficient for viscous damping in the model, being expressed as

$$c_i = 2\pi r_{\text{bh}}^2 h\mu \left(\frac{\alpha_i^4 + \alpha_i^2}{1-\alpha_i^2} \right). \tag{6}$$

2.3. Coupling to downhole friction

The bit at the end of the drill string ensures efficient cutting of the rock by manipulation of the applied weight on bit and top-side rotational speed. Typically, two configurations are found; the tri-cone bit and the drag bit (poly diamond crystal (PDC) cutters, etc.). The latter is used for medium to hard rock, capable of keeping higher penetration rates, and generally is of lower cost than the tri-cone (Dareing et al., 1990). The drag bit is of interest in this work as the friction modeling is based on the blade arrangement on this bit (Detournay et al., 2008). The arrangement defining the bottom hole profile is seen in Fig. 2.

In (Detournay et al., 2008), the physical modeling of the rock cutting process is developed from a drag bit configuration, with n_b consecutive blades. The quantity $d(t)$ is the depth of cut, defining the volume of rock (marked area) being scraped off the rock bottom. In Detournay et al. (2008), the depth of cut is given by $d = 2\pi V_0/\Omega_0$, where V_0 and Ω_0 are the nominal axial velocity and angular velocity of the drill string, respectively.

Processes related to cutting of materials give rise to natural time-delays (Gu et al., 2003). The volume being cut by the tool, is typically dependent on rotational speed of the work-piece. Transferring this to the process of cutting rock while drilling, the representation of the forces and torques due to a time-delay occurring at the drill bit was introduced recently for a two-degree-of-freedom model in (Richard et al., 2004) and

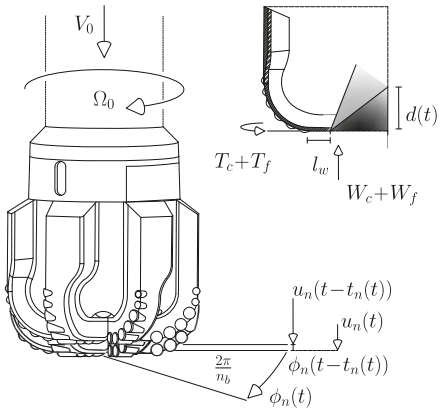

Fig. 2. The blade configuration on a drag bit. V_0 and Ω_0 denotes the nominal axial velocity and angular velocity of the drill string, respectively.

extended in the work by Richard et al. (2007). As such, this model will be the basis of the friction model used here.

As sketched in Fig. 2, the axial displacement of the bit is delayed by the time $t_n(t)$ of one blade in the drag-bit being rotated by $2\pi/n_b$. Hence, the angular displacement profile, could in case of torsional stiction, lag significantly. Further on, $d(t)$ is defined in terms of the current and past axial displacement, yielding

$$d(t) = u_n(t) - u_n(t - t_n(t)) \tag{7}$$

where $t_n(t)$ is the state-dependent delay.

The dynamics of the friction model comprise of the interaction with the bit. The forces are the cutting force and torque on the bit W_c, T_c and the wear flat forces and torques W_f, T_f respectively (subscript c for cutting and f for wear flat). These contribute in different ways depending on the motion of the drill string. In Richard et al. (2007), the forces and torques are defined as

$$W_c = n_b r_b \zeta \varepsilon d(t),\ W_f = n_b r_b l_w \bar{\sigma} h_f(\dot{u}_n(t)) \tag{8}$$

$$T_c = \frac{1}{2} n_b r_b^2 \varepsilon d(t),\ T_f = \frac{1}{2} r_b \mu_f \gamma W_f \tag{9}$$

where n is the number of blades on the bit, r_b is the bit radius, ζ is the orientation of the cutting face for the blade, ε is the intrinsic specific energy required to cut a volume of rock, l_w is the wear flat length of the blade, in contact with the rock, γ is the spatial distribution of wear flats, $\bar{\sigma}$ is the mean contact stress at the wear flats, μ_f is the friction coefficient relating W_f to T_f, and $h_f(\dot{u}_n(t))$ represent whether or not the wear flat forces are active (Besselink et al., 2011). The latter is defined as a Heaviside-function, given as

$$h_f(x) \triangleq \begin{cases} 0, & x < 0 \\ 1, & x \geq 0 \end{cases} \tag{10}$$

which will give $T_f = W_f = 0$ for $\dot{u}_n < 0$, i.e., the bit is moving upwards (off-bottom), and the wear flat forces vanish. The special case of $\dot{u}_n = 0$ will be described in Section 5.

The dependency between the axial and torsional dynamics at the bit is included in the dynamics of the depth of cut $d(t)$. The time-delay, which states the delay from previous position of the cutting blade to the current, is given as a function of the bit rotation angle, $\phi_n(t)$. The constraint is defined as

$$\phi_n(t) - \phi_n(t - t_n(t)) = \frac{2\pi}{n_b} \tag{11}$$

which needs to be solved for $t_n(t)$ numerically at each time-step.

We perform a system transform by changing the equilibrium of the axial dynamics, and analyze the drill string in suspended mode. The new equilibrium is defined as

$$\boldsymbol{u} = \boldsymbol{y} + \mathbf{K}^{-1}\boldsymbol{g} \tag{12}$$

which is done to simplify the dynamical equations in the analysis by recognizing that the term $\boldsymbol{g}$ is constant.

With the definitions of the bit rock forces and torques, we rearrange and express (2) by using (12), and (5) as

$$\mathbf{M}\ddot{\boldsymbol{y}} + \mathbf{D}\dot{\boldsymbol{y}} + \mathbf{K}\boldsymbol{y} = \boldsymbol{t}_1 F(t) - \boldsymbol{t}_2(k_c d(t, t_n) + k_f h_f(\dot{u}_n)) \tag{13}$$

$$\mathbf{J}\ddot{\boldsymbol{\phi}} + \mathbf{C}\dot{\boldsymbol{\phi}} + \boldsymbol{\mathcal{K}}\boldsymbol{\phi} = \boldsymbol{t}_1 T(t) - \boldsymbol{t}_2(t_c d(t, t_n) + t_f h_f(\dot{u}_n)) \tag{14}$$

where $k_c = n_b r_b \zeta \varepsilon$, $t_c = n_b r_b^2 \varepsilon/2$, $k_f = n_b r_b l_w \bar{\sigma}$, and $t_f = r_b \mu_f \gamma k_f/2$. The dynamics of $\boldsymbol{y}(t)$ is then representing the suspended drill string, subjected to gravity.

Note that the nonlinear dynamics then arise from the coupling through $\boldsymbol{t}_2$ with the bit-rock interaction. The equations of motion (7), (11), (13), and (14) comprise of a set of SDDEs due to the bit-rock interaction (Richard, 2003).

2.4. Steady-state behaviour

We want to study the impact of the bit-rock interaction in the system. A steady-state solution is considered in the absence of any vibrations, with the nominal block speed (equal to rate-of-penetration) V_0, top-of-string angular velocity Ω_0 and depth of cut d_0. Hence, we assume $\ddot{\boldsymbol{y}}(t) = 0$, and $\dot{\boldsymbol{y}}(t) = V_0$ in steady-state, being substituted into (13). Furthermore, solving for $\boldsymbol{y}(t)$ in (13) yields the steady-state axial response, denoted with subscript ss, given as

$$\boldsymbol{y}_{\text{ss}}(t) = \mathbf{K}^{-1}\left(\boldsymbol{t}_1 k_1 V_0 t - \boldsymbol{d} V_0 - \boldsymbol{t}_2\left(k_c d_0 + k_f\right)\right) \tag{15}$$

where $\mathbf{D} = \text{diag}(\boldsymbol{d})$, and $\dot{\boldsymbol{y}}_{ss}(t) = V_0$, i.e., assuming constant axial velocity. Noting that $\mathbf{K}^{-1}\boldsymbol{t}_1 = [1/k_1, 1/k_1, \ldots, 1/k_1]^\top$, which is derived analytically in (Hovda, 2016), and expressing the ith axial component, the steady-state is derived as

$$y_{i,\text{ss}}(t) = V_0 t + y^\star_{i,\text{ss}} \tag{16}$$

where $y^\star_{i,\text{ss}}$ is the ith total static axial drilling response, and $V_0 t$ is then the rigid-body displacement of the drill string assembly.

The depth of cut in (16) is then derived, yielding

$$d_0 = \frac{1}{k_c}\left(W_0 - k_f\right) = \frac{2\pi V_0}{n_b \Omega_0} \tag{17}$$

where the constant delay is $t_{n0} = 2\pi/(n_b\Omega_0)$, given constant topside rotation, $W_0 = k_n(y_{ss,n-1} - y_{ss,n})$, k_f is then considered the threshold wear-flat force, and t_{n0} is the steady-state time-delay. The term W_0 is the steady state weight on bit when subject to gravitational forces.

Similarly for the torsional dynamics, the steady-state solution is given by

$$\boldsymbol{\phi}_{\text{ss}}(t) = \boldsymbol{\mathcal{K}}^{-1}\boldsymbol{t}_1 \kappa_1 \Omega_0 t - \boldsymbol{\mathcal{K}}^{-1}\left(\boldsymbol{t}_2(t_c d_0 + t_f) - c\Omega_0\right) \tag{18}$$

$$\phi_{i,\text{ss}}(t) = \Omega_0 t + \phi^\star_{i,\text{ss}} \tag{19}$$

where $\phi^\star_{i,\text{ss}}$ is the static torsional drilling response. From (19) we can derive the threshold torsional wear-flat forces as

$$T_{fs} = \kappa_n\left(\phi_{ss,n-1} - \phi_{ss,n}\right) - c_n\Omega_0 - r_b\frac{W_0 - k_f}{\zeta}.$$

In terms of the transient response of the equations of motion, note that the axial and torsional time scales are not equal. The former time scale is shorter resulting in shorter time-period oscillations. This can be characterized by the speed of sound travelling through the material of the drill string. For steel ($\rho_s = 7850\ \mathrm{kg/m^3}$) these speeds are $c_s = \sqrt{E/\rho_s} \approx 5050\ \mathrm{m/s}$, and $c_t = \sqrt{G/\rho_s} \approx 3180\ \mathrm{m/s}$ for the axial and torsional systems, respectively. An axial wave will travel considerably faster through the medium as compared to a torsional wave.

2.5. Scaling and perturbation coordinates

To reduce the number of system parameters, and analyze the dynamics on a common scale defined by the drill string configuration, we define a common time scale for the systems. The new time unit $\tau = t/\ t^\star$ where $t^\star = L/c_t$ is based on that the torsional speed of sound is considerably lower than the axial speed of sound. The scaled system is then characterized by $c_s/c_t = \bar{c}$. As such, the $t^\star$ corresponds to the time a torsional wave travels the distance L. In addition, we analyze the system from the equilibrium solutions in (16) and (19), where the drill string axial and torsional dynamics are defined by the nominal velocities V_0 and Ω_0.

The perturbations from the nominal solution of (13) and (14) are given as

$$z(\tau) = \boldsymbol{y}(t) - \boldsymbol{y}_{ss}(t),\ \boldsymbol{\theta}(\tau) = \boldsymbol{\phi}(t) - \boldsymbol{\phi}_{ss}(t) \tag{20}$$

The nominal velocities are scaled as $\omega_0 = \Omega_0 t^\star$ and $v_0 = V_0 t^\star$ being the steady-state rate of penetration. The depth of cut is derived from (7), (16) and (20) as

$$\delta = z_n(\tau) - z_n(\tau - \tau_n) + v_0\tau_n \tag{21}$$

where $v_0\tau_n$ is the nominal depth of cut following the time-delay, when perturbations are zero. Hence, $\tau_n = t_n/t^\star$. Additionally, the delay constraint given the angular displacement at the bit is deduced from (11), (19) and (20) as

$$\theta_n(\tau) - \theta_n(\tau - \tau_n) + \omega_0\tau_n = \frac{2\pi}{n_b} \tag{22}$$

which is solved numerically for the time-delay $\tau_n(\tau)$.

Characterizing the axial system by the geometric mean of the cross-sections, and noting that the nominal forces cancel, we can rewrite the equations of motion (13) with the new time-scale as

$$\begin{aligned}\mathbf{A}_1\ddot{z}(\tau) + \frac{c_i n}{G\widehat{a}}\mathbf{D}\dot{z}(\tau) + n^2\bar{c}^2\mathbf{A}_2 z(\tau) &= n^2\bar{c}^2 a_1 \boldsymbol{t}_1 U(\tau)\\ +n_b\alpha\boldsymbol{t}_2\left(v_0\tau_{n0} - \delta + \lambda h_f\left(-\left(v_0 + \dot{z}_n\right)\right)\right)&\end{aligned} \tag{23}$$

where $\mathbf{A}_1 = \mathrm{diag}(\boldsymbol{a}_1)$, $\boldsymbol{a}_1 = [a_1, \ldots, a_n]^\top$, $a_i = A_i/\widehat{a}$, where $\widehat{a}$ is the geometric mean of the cross-sections for the block i drill-pipe/collar segments, $\mathbf{A}_2$ has the same form as $\mathcal{K}$, with a_i s replacing the k_is, $U(\tau)$ is the perturbation in block position, $\alpha = nLr_b\varepsilon\zeta/(G\widehat{a})$, and $\lambda = l_w\bar{\sigma}/\ \zeta\varepsilon$. Furthermore, we have used $k_i = Ea_i\widehat{a}/h$, $m_i = \rho_s a_i\widehat{a}h$. The term $h_f(-x)$ states that the perturbed wear flat forces are constant when the drill bit is moving with the nominal axial velocity v_0.

Considering mass-proportional Raleigh damping (Rao, 2007), we can derive an approximate of the axial and torsional system damping with $\mathbf{D} = d_d\mathbf{A}_1$, where $d_d = d_1/a_1$ is used with the assumption that larger damping occurs around the drill collar mass points in the lumped model than in reality. However, since the drill-pipe section is longer than the BHA, the assumption can be justified (Hovda, 2018b). Then, the axial dynamics can be expressed as

$$\begin{aligned}\mathbf{A}_1\ddot{z}(\tau) + \widehat{d}\mathbf{A}_1\dot{z}(\tau) + n^2\bar{c}^2\mathbf{A}_2 z(\tau) &= n^2\bar{c}^2 a_1\boldsymbol{t}_1 U(\tau)\\ +n_b\alpha\boldsymbol{t}_2\left(v_0\tau_{n0} - \delta + \lambda h_f\left(-\left(v_0 + \dot{z}_n\right)\right)\right)&\end{aligned} \tag{24}$$

where

$$\widehat{d} = \frac{2\pi\mu L c_t}{G a_1\widehat{a}}\left(\frac{1+\alpha_1^2}{1-\alpha_1^2}\ln\alpha_1^{-1} - 1\right)^{-1}. \tag{25}$$

Similarly, using the geometric mean of the second moment of area, proportional damping, and the new time scale for the torsional dynamics in (14), we get

$$\begin{aligned}\mathbf{L}_1\ddot{\boldsymbol{\theta}}(\tau) + \widehat{c}\mathbf{L}_1\dot{\boldsymbol{\theta}}(\tau) + n^2\mathbf{L}_2\boldsymbol{\theta}(\tau) &= n^2 I_1\boldsymbol{t}_1\Phi(\tau)\\ +\boldsymbol{t}_2 n_b\frac{\widehat{a}r_b\alpha}{2\widehat{l}\zeta}(v_0\tau_{n0} - \delta + \beta\lambda h_f(-(v_0 + \dot{z}_n)))&\end{aligned} \tag{26}$$

where $\mathbf{L}_1 = \mathrm{diag}(\mathbf{L}_1)$, $\mathbf{L}_1 = [l_1, \ldots, l_n]^\top$, $l_n = I_{z,i}/\widehat{l}$, where $\widehat{l}$ the geometric mean of the second moment of area for block i drill pipe or collar segments, $\mathbf{L}_2$ has the same form as $\mathcal{K}$ with l_is replacing the κ_i, $\Phi(\tau)$ is the perturbation in top-of-string angular displacement, $\widehat{c} = (2\pi r_{\mathrm{bh}}^2\mu L c_t/(Gl_1\widehat{l}))\cdot((\alpha_i^4 + \alpha_i^2)/(1 - \alpha^2))$, and $\beta = \mu_f\gamma\zeta$. Furthermore, we have used $\kappa_i = Gl_i\widehat{l}/h$, $J_i = \rho_s h l_i\widehat{l}$.

The three constants α, λ and β in (24) and (26) characterizes the drill string design and interaction with the cutting forces and wear flat forces, respectively.

3. Parameter analysis of axial dynamics

In normal drilling operations, the travelling block is moving with constant speed v_0 and $\delta > 0$. Next, we assume the following conditions:

1. Torsional vibrations are constant, i.e., the delay τ_n originating from the lag in bit blade rotation due to sticking is constant, $\tau_n = \tau_{n0}$. During the axial vibrations the angular velocity of the bit is slowly varying, so that during these cycles higher-frequency vibrations for the axial dynamics can occur.
2. The wear flat forces are constant due to assuming a positive bit velocity, i.e., $\dot{z}_n > -v_0$.

The first assumption implies that we decouple the axial system from the torsional system, and can analyze the stability regime individually. We now direct our analysis to the axial motion of the drill string. To understand the time delay impact on the axial dynamics, we will in this section derive a representation of the stability for the downhole conditions.

Both $\mathbf{A}_1$ and $\mathbf{L}_1$ are positive definite and diagonal. However, the form of $\mathbf{A}_2$ and $\mathbf{L}_2$ are not diagonal. Since $\boldsymbol{x}^\top\mathbf{Q}\boldsymbol{x} > 0, \forall \boldsymbol{x} \in \mathbb{R}^n\backslash\{0\}$, $\mathbf{Q} = \mathbf{Q}^\top \in \{\mathbf{A}_1, \mathbf{A}_2, \mathbf{L}_1, \mathbf{L}_2\}$, and the eigenvalues of $\mathbf{Q}$ are real, all leading principle minors of $\mathbf{Q}, 1 \le k \le n$ are positive, then the set of matrices represented by $\mathbf{Q}$ are real symmetric positive definite (Golub and Loan, 2013).

With these definitions, we can rewrite the equations of the axial dynamics and investigate the modal decoupling when subject to the bit-rock interaction. This motivates derivation of the dynamics with the *eigendecomposition* of the matrix pair $(\mathbf{A}_1, \mathbf{A}_2)$.

For the symmetric positive definite matrix pair $(\mathbf{A}_1, \mathbf{A}_2)$ we have that (Golub and Loan, 2013)

$$\mathbf{A}_1\boldsymbol{v} = \lambda_i\mathbf{A}_2\boldsymbol{v} \tag{27}$$

where $\boldsymbol{v}$ is the generalized eigenvector associated with the λ_i eigenvalue, $\mathbf{V}^\top\mathbf{A}_1\mathbf{V} = \mathbf{I}$, $\mathbf{V}^\top\mathbf{A}_2\mathbf{V} = \boldsymbol{\Lambda}$, where $\mathbf{V} = [\boldsymbol{v}_1, \ldots, \boldsymbol{v}_n]$ is the real nonsingular eigenvector matrix, and $\boldsymbol{\Lambda}$ is the diagonal eigenvalue matrix. This also applies for the pair $(\mathbf{L}_1, \mathbf{L}_2)$.

Assuming zero perturbation for the block position, $U(\tau) = 0$, and using the linear system transform $z(\tau) = \mathbf{V}\boldsymbol{x}(\tau)$ for the left-hand side of

the axial dynamics in (24), yields

$$\ddot{\boldsymbol{x}} + \widehat{d}\dot{\boldsymbol{x}} + n^2\bar{c}^2\boldsymbol{\Lambda}\boldsymbol{x} = -n_b\alpha\mathbf{V}^\top \boldsymbol{t}_2(z_n(\tau) - z_n(\tau - \tau_n)) \tag{28}$$

where we have premultiplied with $\mathbf{V}^\top$, $\boldsymbol{x}$ is the modal coordinate vector corresponding to the generalized coordinates, and $z_n(\tau)$ is the nth element of $\boldsymbol{z}(\tau)$.

Taking the Laplace transform of (28), and defining $\boldsymbol{x}(0) = \dot{\boldsymbol{x}}(0) = 0$, $z_n(0) = \dot{z}_n(0) = 0$ yielding zero perturbation from the nominal solution, we get

$$\left(\mathbf{I}s^2 + \widehat{d}\mathbf{I}s + n^2\bar{c}^2\boldsymbol{\Lambda}\right)\mathbf{X}(s) = -n_b\alpha\mathbf{V}^\top\boldsymbol{t}_2(1 - e^{-\tau_n s})Z_n(s) \tag{29}$$

where $\mathbf{I}$ is the identity matrix, $\mathscr{L}\{\boldsymbol{x}(\tau)\} = \mathbf{X}(s)$, and $\mathscr{L}\{z_n(\tau)\} = Z_n(s)$.

3.1. Stability of axial dynamics

To analyze the stability of the downhole conditions while drilling ($\tau_n \geq 0$), we must derive the characteristic polynomial of (28) for $z_n(\tau)$, being the nth element of $\boldsymbol{z}(\tau)$.

The response of the last block of the drill string (the BHA) is given as a sum of the assembly modal coordinates, yielding

$$Z_n(s) = \sum_{j=1}^{n} V_{nj}X_j(s) \tag{30}$$

where $Z_n(s)$ is the nth block coordinate, and $X_j(s)$ is the jth modal coordinate. The jth component of (29) is given as

$$\left(s^2 + \widehat{d}s + \omega_j^2\right)X_j(s) = -n_b\alpha V_{nj}(1 - e^{-\tau_n s})Z_n(s) \tag{31}$$

where $\omega_j^2 = n^2\bar{c}^2\lambda_j$, i.e., the eigenfrequency of the jth mode. Equation (31) can be solved for $X_j(s)$ and inserted into (30), yielding

$$\left(1 + n_b\alpha\sum_{j=1}^{n}\frac{V_{nj}^2}{s^2 + \widehat{d}s + \omega_j^2}(1 - e^{-\tau_n s})\right)Z_n(s) = 0 \tag{32}$$

being the response of the last block of the drill string assembly.

Expanding (32) and rewriting yields

$$\begin{aligned}&(A(s) - B(s)e^{-\tau_n s})\\ &B(s) = n_b\alpha\sum_{j=1}^{n}V_{nj}^2\prod_{i\neq j}p_i(s),\ A(s) = \prod_{i=1}^{n}p_i(s) + B(s)\end{aligned} \tag{33}$$

where $p_i(s) = (s^2 + \widehat{d}s + \omega_i^2)$. Note also that $\deg(A(s)) = 2n$ and $\deg(B(s)) = 2n - 2$.

In the case of $\tau_n = 0$, (33) reduces to $\prod_{i=1}^{n}p_i = 0$ being a power of $2n$ polynomial in s. The roots of the reduced system yields the roots of the uncoupled characteristic polynomial, from the left-hand side of (29). In component form, the latter polynomial can be defined as

$$s^2 + \widehat{d}s + \omega_i^2 = 0 \tag{34}$$

which is equal to $p_i(s)$ from (33), and constitute two roots s_1, s_2 for each mode $x_i(s)$. These are given by

$$s_{1,2} = \frac{1}{2}\left(-\widehat{d} \pm \sqrt{\widehat{d}^2 - 4\omega_i^2}\right) \tag{35}$$

such that the downhole bit motion is dependent on the stability of the modes for the entire drill string, naturally.

From the magnitudes in Table 2 found in Section 5, we conclude that the roots in (35) are located in the left-half plane for $\tau_n = 0$. Since $4\omega_i^2 > \widehat{d}^2$ with $\widehat{d}, n, \bar{c}, \lambda_i > 0$, and the root is a complex conjugate pair. Then, the nominal solution is considered stable independent of the delay. Note that for $\widehat{d} = 0$ the system is marginally stable with roots located at zero on the imaginary axis, and non-decaying oscillations can occur.

The quasi-characteristic polynomial in (33) generates infinite number of roots due to the exponential function (Sipahi, 2019). In order to investigate the response for $Z_n(s)$, with $\tau_n > 0$, we analyze the critical roots and subsequent time-delays generating crossings at the imaginary axis for $s = j\omega$, where j is the imaginary unit. The quasi-characteristic polynomial is defined as

$$P(s, \tau_n) = A(s) - B(s)e^{-s\tau_n} \tag{36}$$

being expressed in similar form as in (Walton and Marshall, 1987). Hence, $\deg(A(s)) > \deg(B(s))$. The goal is to obtain the critical values of τ_n generating crossing frequencies on the imaginary axis, and investigate the stability limits. Keeping the exposition, we add additional details from the procedure in (Walton and Marshall, 1987). The following sub-goals are defined to derive the system stability:

1. Obtain a polynomial $F(\omega)$ given the scalars $A(s)$, $B(s)$ in order to calculate the critical crossing frequencies. The roots of $F(\omega)$ yields the critical crossing frequencies.
2. If no roots exists for $F(\omega)$ (no critical crossing frequencies):
   (a) Compute the system stability from (34).
   (b) Identify if stable for all τ_n or unstable for all τ_n.
3. Calculate the critical time-delay switches from the crossing frequencies.
4. Identify the direction of each crossing, to indicate if the crossing is stabilizing or destabilizing.
5. Define the *delay-margin*, i.e., the final stability border.

We start by defining (Walton and Marshall, 1987; Wang and Hu, 2000)

$$F(\omega) = \left|A(j\omega)\right|^2 - \left|B(j\omega)\right|^2 \tag{37}$$

where $F(\omega)$ is a real-valued polynomial where the critical crossing frequencies can be obtained independent of τ_n. Note that $\deg(F(\omega)) = 4n$.

The conjugate symmetry of the complex root s is used to state that $P(s, \tau_n) = 0 \Rightarrow P(-s, \tau_n) = 0$ for the same purely imaginary root s. From this, we insert $s = \pm j\omega$ into (36) and get

$$\begin{aligned}&A(j\omega) - B(j\omega)e^{-\tau_n j\omega} = 0\\ &A(-j\omega) - B(-j\omega)e^{\tau_n j\omega} = 0\end{aligned}$$

for roots of the quasi-characteristic polynomial. We can then eliminate the exponential term (by exploiting that $A(s), B(s)$ are scalars) and obtain

$$\left|A(j\omega)\right|^2 - \left|B(j\omega)\right|^2 = F(\omega) = 0. \tag{38}$$

which is the polynomial in (37). Since $F(\omega)\to\infty$ for $\omega = \pm\infty$ (since $A(s)$ is higher order than $B(s)$), we consider the positive frequencies $\omega\to\infty$. The interpretation of $F(\omega)$ is the ability to decouple the critical crossing frequencies $\omega^\star$ from the time-delay values $\tau_n^\star$.

Solving for the roots of (37) yields the critical zero crossing frequencies $\omega^\star$ of the system. If no roots are generated from solving (37), i.e., no crossing points exist, the system stability is characterized from the previous criteria of $\tau_n = 0$. If (36) is declared stable independent of the delay, the overall system is stable (and vice versa for unstable (36)).

In the case of (37) generating roots, the crossing frequencies are associated with a series of delay switches and constitute pairs $(\omega_k^\star, \tau_{n,k}^\star)$, where $\omega_1^\star > \omega_2^\star > \ldots \omega_N^\star > 0$, and N is the total number of crossing frequencies of $F(\omega)$. It is noted that $e^{-\tau_n j\omega} = \cos(\omega\tau_n) - j\sin(\omega\tau_n)$, which can be used to obtain the argument of the exponential term defined as the phase angle θ_k

$$\theta_k = \angle\frac{B(j\omega_k^\star)}{A(j\omega_k^\star)} = \angle B(j\omega_k^\star) - \angle A(j\omega_k^\star) \tag{39}$$

defined so that $\theta_k \in [0, 2\pi)$, and $\angle$ is the phase angle between the imaginary and real part of a complex number.

Due to the periodicity of the phase angle, the critical delays can be calculated from a given crossing frequency ω_k as (Walton and Marshall, 1987)

$$\tau_{n,k,r} = \frac{\theta_k}{\omega_k^\star} + \frac{2\pi r}{\omega_k^\star}, r = 0, 1, 2, \ldots, m_r \tag{40}$$

where each $\tau_{n,k,r}$ represents a critical time-delay in the system connected to a pair of roots in (36) passing from right to left or left to right in the complex s-plane.

The direction of each crossing can be found by the sign value of $\text{Re}(\text{d}s/\text{d}\tau)_{(s=j\omega_k^\star, \tau=\tau_{n,k,r})}$, which can be derived by differentiating (36) w.r.t. τ_n.

However, as shown in (Walton and Marshall, 1987), the direction of the zero crossings at a particular root is independent of the critical delays at this point. The reader is referred to [36, Section 2] for this proof. The direction is shown to be given by $F'(\omega_k^\star)$ where the prime denotes differentiation w.r.t. $\omega_k^\star$.

The critical delays $\tau_{n,k,r}$ associated with the zero crossing direction given by the root ω_k defines the system stability in a given interval. Note that each root is arranged from largest to smallest, where $\omega_{k=1}$ is the largest root. The time-delay $\tau_{n,k,r}$ corresponding to the largest root, is connected to a new pair of conjugate roots for (36) with positive real part since $F'(\omega_k) > 0$, which is compensated for by the following root with $F'(\omega_{k+1}) < 0$ for $\tau_{n,k+1,r}$ where $k \geq 0$. Ultimately a delay-margin will be found, and the subsequent delays denotes an unstable system (see e.g. (Gu et al., 2003; Sipahi, 2019),).

4. Stability switches for a decoupled system

The dynamics of the drill string are modelled assuming a vertical wellbore. To analyze the stability boundaries and transient response from different boundary conditions, six realistic drill string configurations are used, being drawn from (Hovda, 2018b). The characteristic values for each section are defined in Table 1. Common casing installation applies for the 36″ to the 12 ¼″ section. The two last wellbores are liners, threaded on the previous casing shoe. The last liner, being suspended from the last casing shoe, runs into the open hole section. The bit used for drilling each section corresponds to the hole size row.

We assume the following bit-rock values: $\overline{\sigma} = \varepsilon = 45$ MPa, $l_w = 0.001$ m, $\mu_f = 0.3$, $\zeta = 0.65$, and $\gamma = 1$.

4.1. Special case for $n = 1$

In the case of $n = 1$, the model simplifies to a two-degree-of-freedom model, such as the case in (Besselink et al., 2011; Nandakumar and Wiercigroch, 2013; Depouhon and Detournay, 2014). The equation of motion for the axial dynamics in (24) assuming constant torsional vibrations reduces to

$$\ddot{z}(\tau) + \widehat{d}\dot{z}(\tau) + \overline{c}^2 z = \frac{n_b L r_b \varepsilon \zeta}{GA}(z(\tau - \tau_n) - z(\tau)) \tag{41}$$

since $a_i = A_i/\widehat{a}$ for $i = n = 1$, and A is the drill string element area, being either pipe or collar. Hence, the characteristic polynomial is given from the Laplace transform as shown in Section 3 as

$$P(s, \tau_n) = s^2 + \widehat{d}s + \omega_1^2 + \frac{n_b L r_b \varepsilon \zeta}{GA}(1 - e^{-\tau_n s}) \tag{42}$$

where $\omega_1 = \overline{c}$, and using the steps in Section 3.1, (42) can be utilised to characterize $P(s, \tau_n) = 0$. Hence, the critical time-delays and crossing frequencies can be calculated and compared to previous work with similar values for $\widehat{d}$, and the drilling parameter $n_b L r_b \varepsilon \zeta/(GA)$.

4.2. Critical speed margins

The number of computed time-delays per crossing frequency $\omega_k^\star$ is set by $m_r = 10$ in (40). Considering the case of $\mathbf{A}_1 = \mathbf{I}$, i.e., a uniform drill string assembly, we compute the critical crossing values and corresponding time-delays. The damping for each of the drill string configuration are given by (25).

To analyze the critical rpm values required to keep the axial motion of the system stable, the nominal angular velocity ω_0 can be computed from $\tau_n = 2\pi/(n_b\omega_0)$. By increasing the number of lumped elements, we investigate the coupled behaviour of the model to critical rpm values from the configurations in Table 1. Furthermore, in this analysis we restrict $n = 40$. Expanding the analysis to $n > 40$ and beyond is restricted by the magnitude of $F(\omega)$ and consequently the evaluation of $F'(\omega)$.

The calculated delay margins of the axial system given in terms unscaled nominal angular velocity Ω_0 for each section, and n, are presented in Fig. 3. The case of $n = 1$ is computed with (42). Recall that $\Omega_0 = \omega_0 c_t/L$, being scaled for each section.

From the computations, one distinct delay margin is found from assuming an uniform drill string made up of drill pipes. This can be explained by looking at the crossing frequencies obtained from $F(\omega)$ and the drill string eigenfrequencies ω_j. For a 36″ section with $n = 2$, $\widehat{d} \approx 1.55{\cdot}10^{-5}$, $\omega_j = [5.1392, 1.9630]$ and the crossing frequencies are $\omega_k^\star = [15.7675, 5.1392, 4.442, 1.9630]$. Recall that the first, largest crossing frequency is associated with $F'(\omega_k^\star) > 0$. In the case of the 36″, it is three times larger than the second frequency. Evaluating the range of time-delays, it is found that $\omega_1^\star$ is repeated several times before a switch associated with stabilizing crossing is generated. For all the sections, similar results were found.

Secondly, what is seen in Fig. 3 is that the critical rpm values are almost linearly increasing after $n = 20$ requiring high rpm values to avoid self-excited axial vibrations. It is noticed that only modeling with a single element yields similar delay margin as the higher order configurations.

Adding a BHA to the drill string will, in some cases, generate more than one stability switch, where the frequency spectrum becomes more complex ($\mathbf{A}_1 \neq \mathbf{I}$). To compare the boundaries with the uniform drill string assembly, we select the lower most stability switch for the six configurations. The result is seen in Fig. 4.

The general observation of adding a BHA is that the overall required rpm values decreases for drilling the four last sections. However, comparing the rpm curves to Fig. 3, similar prediction can be made on a stable linear increase required for increasing number of lumped elements in the model. The consequence of this observation is that for the assumptions made to decouple the axial-torsional dynamics, the dynamic behaviour of the drill string for sufficiently large n might never be

Table 1
Well data. DP – Drill pipe, DC – drill collar, DSL – Drill string length, OD – outer diameter, ID – inner diameter.

Section num.	1	2	3	4	5	6
Section type	Casing	Casing	Casing	Casing	Liner	Liner
Hole size [in]	36	26	$17^{1/2}$	$12^{1/4}$	$8^{1/2}$	6
DSL [m]	200	650	1350	2275	3700	4370
DP OD [in]	5	5	5	5	5	5
DP ID [in]	4.276	4.276	4.276	4.276	4.276	4.276
DP area [m]	0.0034	0.0034	0.0034	0.0034	0.0034	0.0034
DC OD [in]	$11^{1/4}$	$11^{1/4}$	$11^{1/4}$	10	$6^{1/2}$	$3^{3/4}$
DC ID [in]	$3^{1/4}$	$3^{1/4}$	$3^{3/4}$	3	$2^{1/4}$	$1^{1/2}$
DC area [m]	0.0406	0.0406	0.0406	0.0375	0.0344	0.0188
l_{dc} [m]	24	45	53	100	170	170
μ [Pa s^{-1}]	0.0011	0.0011	0.03	0.03	0.03	0.03
ρ_m [kg m^{-3}]	1025	1025	1400	1600	1800	1100

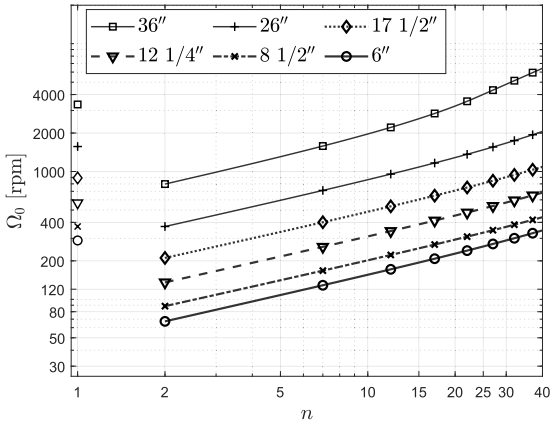

Fig. 3. Log-scale plot of Ω_0, n, the critical rotation speeds for increasing n considering a uniform drill pipe assembly.

stable.

Drag bits are capable of drilling with high rotation speeds. However, investigating the critical speed margins in Figs. 3 and 4, we notice that only the longer sections where sufficiently high weight from the drill string is achieved, are the rpm values in the range reported in (Aadnoy et al., 2003; Lai et al., 2016).

The findings are similar to the analysis in (Dareing et al., 1990), where it is found that the bit-radius has a direct impact in how fast the drill string can be rotated to avoid self-excited axial vibrations. The required rotary speed is dependent on application (reaming, hole-cleaning, friction testing, etc.), and limitations on the top drive itself for allowable supplied torque.

The response of the axial system from (24) subject to constant wear flat forces and no torsional vibrations is given by

$$\mathbf{A}_1\ddot{\boldsymbol{z}} + \widehat{d}\mathbf{A}_1\dot{\boldsymbol{z}} + n^2\bar{c}^2\mathbf{A}_2\boldsymbol{z} = n_b\alpha\boldsymbol{t}_2(z_n(\tau-\tau_n) - z_n). \tag{43}$$

Equation (43) is linear for a constant delay τ_n, and is completely decoupled from v_0. Disturbances from the nominal solution will, according to the defined stability boundaries, imply growing oscillatory behaviour if the drilling rpm is below the required limit. The wear flat forces was assumed constant, with the bit being on bottom at all times.

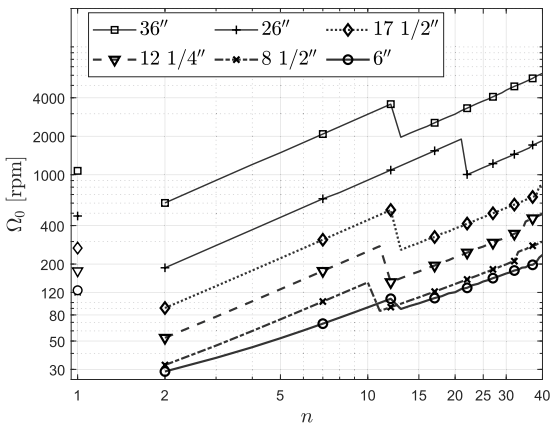

Fig. 4. Log-scale plot of Ω_0, n, the critical rotation speeds for increasing n considering a drill string with BHA.

Ultimately, the drilling coordinator will manipulate both v_0 and ω_0 to achieve stable drill string behaviour.

5. Simulation study

The necessity to analyze the system coupled leads to studying the response from simulating the equation of motions of (21), the algebraic relation (22), (24), and (26). To investigate the behaviour of the system, we need to address $h_f(0)$ and δ, i.e., the coupling between (24) and (26).

Note that the simulations presented in this section are done using open-loop control to investigate the axial-torsional cyclic behaviour, with constant parameters (v_0,ω_0). In a realistic scenario, a controller will be implemented such as to avoid developing sustained oscillations by manipulating the top drive and travelling block parameters.

5.1. Wellbore contact scenarios

In Detournay et al. (2008), three distinctive phases (Phase I–III) of drilling are described. The first phase, Phase I, is dominated by the contact forces at the bit, since δ is larger than zero (bit is always on-bottom), and axial velocity being v_0. In Phase II, a critical value of the depth of cut is reached and indicates that the wear flat forces (contact forces due to friction), W_f, T_f, do not increase beyond the normal contact stresses, defined by $\bar{\sigma}$. However, the necessary increase in bit normal forces is directed through the cutting component. Phase III is defined by the external forces due to hole cleaning, increased wear flat length of the bit due to build up of rock cuttings around the BHA. The latter phase is not considered in this paper.

We need to translate the behaviour of the drilling regime to the model derived up until this point. The conditions for axial and torsional stick need to be treated, which relates to the distinctive phases of drilling.

5.1.1. Nominal drilling conditions

The drill bit follows the nominal axial and angular velocities v_0 and ω_0, respectively. Furthermore, the bit is constantly moving downwards being on-bottom, and δ is larger than zero. As such, the wear flat forces is constant since the bit velocity is positive. The cutting forces are active in this phase.

5.1.2. Axial bit stick-slip

When the longitudinal motion of the bit is stopped and the position of the bit is constant for a short time period, the forces at the bit in the axial direction compensate for the weight of the drill string. In this case, while rotation is ongoing, the forces situated at the bit can become periodic due to the effect of delayed cutting. The effect of the periodicity can then result in the axial stick-cycles (Dareing et al., 1990).

From the model, we can express this as a situation where the nth state axial velocity becomes zero ($\dot{z}_n = -v_0$), and that a wear flat force ensures axial equilibrium of the bit in the moment of axial stick. From (24) we can derive the axial equilibrium $\ddot{z}_n = 0,\ \dot{z}_n = -v_0$ of the nth block as

$$\begin{aligned}&-\widehat{d}A_{1,[n,n]}v_0 + n^2\bar{c}^2A_{2,[n,n]}(z_n - z_{n-1})\\ &\quad -n_b\alpha(v_0\tau_{n0} - \delta) + F_{fa} = 0\end{aligned}$$

where the axial equilibrium force F_{fa}, is then given as

$$F_{fa} = n_b\alpha(v_0\tau_{n0} - \delta) - n^2\bar{c}^2a_{2,n}(z_n - z_{n-1}) + \widehat{d}a_{1,n}v_0 \tag{44}$$

such that in the time-period of axial stick the force oppose the motion of the bit, until the weight of the drill string assembly overcomes the wear flat forces.

In the case of bit bounce, the depth of cut becomes negative ($\delta < 0$) and the bit loses contact with the rock. Thus, the cutting and wear flat forces is zero until the weight of the drill string forces the bit down onto the rock again.

Table 2
Model parameters with $n = 2$ for 36″ ($t^\star = 0.0629$) and 12 1/4″ section ($t^\star = 0.716$), $\mu_f = 0.3$.

	$\widehat{d}$	$\widehat{c}$	$n_b{\cdot}\alpha$	λ	β	$n^2{\cdot}\bar{c}^2$	$\frac{\widehat{a}r_b\alpha}{2\widehat{l}\zeta}$
1	$1.549{\cdot}10^{-5}$	$1.954{\cdot}10^{-5}$	119.0	0.001538	0.1950	10.09	1996
4	0.01987	0.008163	460.7	0.001538	0.1950	10.09	2629

5.1.3. Torsional stick-slip

Torsional stick occurs when the wear flat and cutting forces become too large, resulting in the bit coming to a complete stop in the formation. Hence, the condition $\dot{\phi} = -\omega_0$ is fulfilled for the time instance. Furthermore, we assume that the wear flat forces are large enough to keep the bit from rotating backwards. During a torsional stick phase the torque on bit due to the interaction with the formation is larger than the applied torque from the drill string.

Considering the cutting process from Fig. 2, if the bit comes to a complete stop in torsional motion this means that it is not cutting rock any more. Consequently, this leads to a stop in axial motion of the bit, such that we can assume that the bit will not move further downwards.

The externally applied torque at the bit builds up in the drilling assembly, eventually leading to the bit accelerating, as $\ddot{\theta}_n > 0$, and breaking free from the formation. The bit starts to accelerate again whenever the sum of torques at the bit is larger than zero, given as

$$\widehat{c}l_{1n}\omega_0 - n^2 l_{2n}(\theta_n - \theta_{n-1}) + n_b\frac{\widehat{a}r_b\alpha}{2\widehat{l}\zeta}(v_0\tau_{n0} - \delta + \beta\lambda h_f(-(v_0 + \dot{z}_n)) > 0.$$

5.2. Drilling with uniform assembly

Suppose that the assembly consists of drill pipes, such that $A_1 = I_1 = I$ in (24) and (26). We want to predict the axial and torsional motion of drilling with nominal axial and angular velocities, v_0 and ω_0.

To give an insight in the scale of the parameters for the model, we compare the magnitude for the 36″ and 12 ¼″ section, dividing the drill string into two elements. The values are given in Table 2.

The general observation for the order of magnitude of the model parameters is that the shorter section has less damping, and the stiffness parameter $n^2{\cdot}\bar{c}^2$ is the same in both configurations. This yields a stiffer drill string assembly per mass point for the shorter section, thus higher rotational speeds are required to overcome the down-hole friction. The cutting and wearflat forces characterized with α increase for longer wellbore sections (in this work, λ and β are independent on the drill string assembly) corresponding to potential higher weight on bit and torque on bit from the drill string.

A simulation experiment is now considered with $\Delta\tau = 5{\cdot}10^{-4}$, numerically integrating the model with the Newmark regime ($\beta = 1/4$, $\gamma = 1/2$). We set a nominal axial velocity of $V_0 = 0.05$ m/s and angular velocities to $\Omega_0 = 5\pi$ rad·s^{-1} (150 rpm, $v_0 \approx 0.0031$, $\omega_0 \approx 0.98$ for the 36″ well), to investigate the coupled effect of the axial and torsional motion. Perturbation inputs are set as $U(\tau) = \Phi(\tau) = 0$. We assume that $z(0) = \boldsymbol{\theta}(0) = 0$ for $t \leq 0$. Note that 150 rpm is considered a stable rotation speed for 12 ¼″, in the decoupled configuration as seen in Fig. 3.

The response of drilling the two wellbores from Table 2 is presented in Figs. 5 and 6 respectively.

The response for the 36″ section (Fig. 5) is seen to be highly irregular, due to the stiffness of the drill string and low rpm. The torque at the bit builds up, and a sudden increase in bit speed is seen at $\tau \approx 25$. The depth of cut is gradually increasing after $\tau \approx 40$ as the bit velocity is kept positive.

From $\tau = 0$ to $\tau \approx 5$ in the top-most plot of Fig. 6 the difference in timescale are seen from the response of the faster axial vibrations. It is noticed that the drill string immediately experience bit-bounce for the 12 ¼" section. As the drill string is moving with a constant velocity, the axial and torsional stick-slip cycle develops. In some periods of the time series, the axial vibrations are seen to have higher frequency. The axial stick cycles lowers the drilling performance, as seen by comparing the two depth of cut profiles for 36″ and 12 ¼″ sections.

Increasing the length of the well being drilled is seen to increase the time-period of the vibrations. The stiffness of the 12 ¼″ drill string is lower, but the external torque generated at the bit is larger such that stick-slip cycles occurring, at the bit are more periodic. Furthermore, axial stick slip is occurring and with the increased length, the amplitude is larger and with higher frequency.

Comparing these two case studies, we can distinguish the drilling performance of the two wells. In this survey, the shorter wells is seen to require larger topside rotational speed to be efficiently drilled without the bit sticking to the rock, due to less build-up of rotational energy transmitted to the far end at the bit.

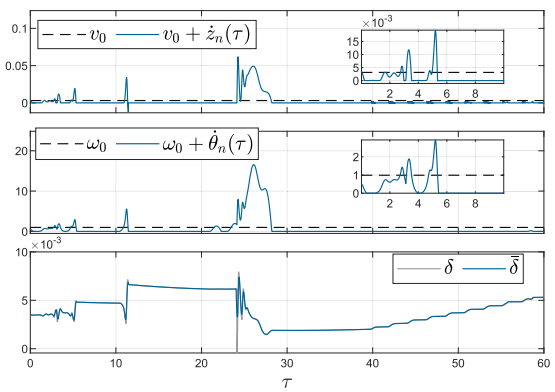

Fig. 5. System response with $n = 2$ when drilling a 36″ well. Initial conditions are: $\dot{\theta}_i(0) = -0.5\omega_0$ and $\boldsymbol{\theta}(t) = z(t) = 0, \forall t \leq 0$. $\bar{\delta}$ is the moving mean of δ calculated in a window of 20 sampling points.

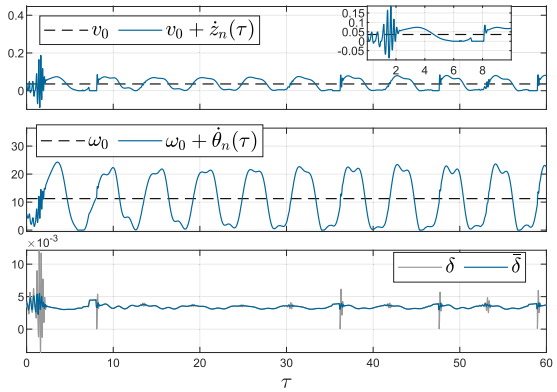

Fig. 6. System response with $n = 2$ when drilling a 12 1/4″ well. Initial conditions are: $\dot{\theta}_i(0) = -0.5\omega_0$ and $\boldsymbol{\theta}(t) = z(t) = 0, \forall t \leq 0$. $\bar{\delta}$ is the moving mean of δ calculated in a window of 20 sampling points.

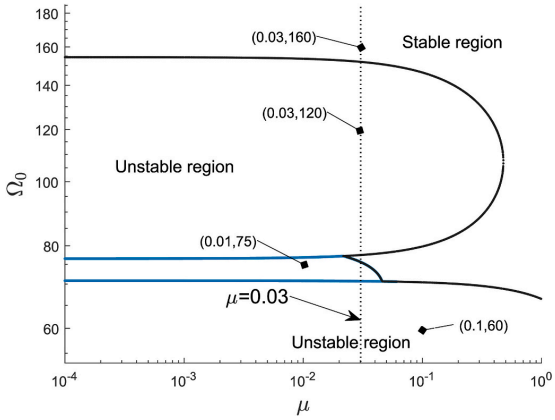

Fig. 7. Log-plot of the stability zones for 12 1/4″ $n = 6$ with BHA. The black line corresponds to the found critical switches, and the combined black and blue line marks the true stability zone by $\omega_k^\star$. (For interpretation of the references to colour in this figure legend, the reader is referred to the Web version of this article.)

5.3. Drilling with BHA

Suppose a BHA is added to the assembly. From the stability analysis done in Section 3, a sketch of the stability zones governing a $n = 6$, 12 ¼″ BHA drill string configuration is given in Fig. 7 for the critical rpm values versus the mud viscosity. The latter scales $\widehat{d}$, $\widehat{c}$, i.e., the axial and torsional drag force coefficients. Furthermore, the shown stability map is only valid for (43), which is the decoupled axial dynamics. The four operating points (OP) correspond to stable or unstable equilibria. Simulating (43), the transient responses are presented in Fig. 8 for each OP to an initial condition on the lower-most block element.

In Fig. 7, the black line mark the computed critical stability switches, and the blue line is an extension given by $\omega_k^\star$. The latter then connects with the critical switches at the points which tends towards infinity for each axis. As such, three separate zones appear from adjusting the viscosity from 0.0001 to 1. The area between the blue lines are defined as a stable region.

As expected, the stability zones dictate the dynamic behaviour of the axial system, where the unstable parameters yields growing oscillatory behaviour seen in Fig. 8.

We simulate the coupled axial-torsional motion of a 12 ¼″ section again with $n = 6$ for the two OPs, $\text{OP}_1 = (0.03, 120\ \text{rpm})$ and $\text{OP}_2 = (0.03, 160\ \text{rpm})$ from Fig. 7. Perturbation inputs are set as $U(\tau) = \Phi(\tau) = 0$. The OPs correspond to $(0.03, 8.995)$ and $(0.03, 11.99)$, scaled for the current drill string configuration. The nominal axial velocity is $V_0 = 0.05$ m/s corresponding to $v_0 = 0.0358$. The system parameters are presented in Table 3. The simulation step size is equal to the one in the previous section. The transient responses for the two operating points are presented in Fig. 9.

A consequence of the initial condition is that the axial vibrations develop before going into cyclic behaviour, from the top-most plot of Fig. 9. Before $\tau \approx 65$, slowly varying torsional oscillations are seen in the middle plot. Beyond $\tau = 65$ the drill string develops sustained stick-slip cycles, both in the axial and torsional domain for OP_1 with $V_0 = 0.05$ m/s. The OP_2 configuration (dashed blue line) is due to the higher rpm, avoiding axial-torsional stick cycles. However, the growing oscillatory pattern develops during the model simulation. The longest torsional stick period for OP_1 at $\tau = 80$ is approx. $\tau \approx 3$, corresponding to a torsional wave travelling three times in the drill string before the bit breaks free. Since rotation is stopped during torsional stick, the axial velocity comes to a halt.

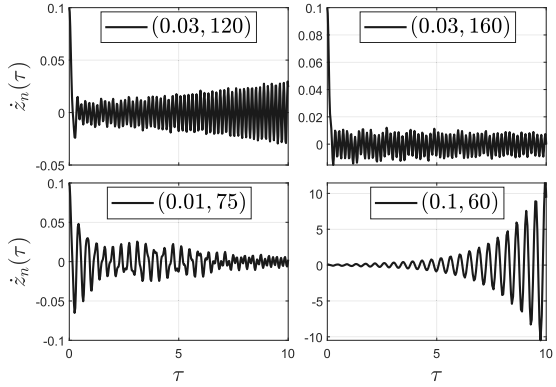

Fig. 8. Axial dynamics response to initial conditions $z(0) = 0.1$, for the operating points in Fig. 7.

Table 3
Model parameters for a 12 1/4″ section with $n = 6$. Here, $\mu = 0.03$.

$\widehat{d}$	$\widehat{c}$	$n_b \cdot \alpha$	λ	β	$n^2 \cdot \widehat{c}^2$	$\frac{\widehat{a} r_b \alpha}{2\widehat{\zeta}}$
0.01987	0.008163	926.5	0.001538	0.1950	90.79	4380

The inertia due to a larger end element reduces the frequency of these vibrations, and an effect of reduced formation sticking is seen. It is noticed that the axial and torsional stick cycles have lower frequency, and the amplitude is reduced compared to Fig. 6. However, the vibrations directly translate to how smooth the depth of cut profile is, seen in the lower-most plot.

6. Discussion

The findings presented are based on assuming a vertical wellbore, and the decoupled axial and torsional system. The dynamics of drill strings, both in vertical and deviated wellbores, are complex with the motion in all axes being coupled. As such, the work presented here is a simplified case study in characterising the dynamic stability, and we leave the analysis of fully coupled stability to future work.

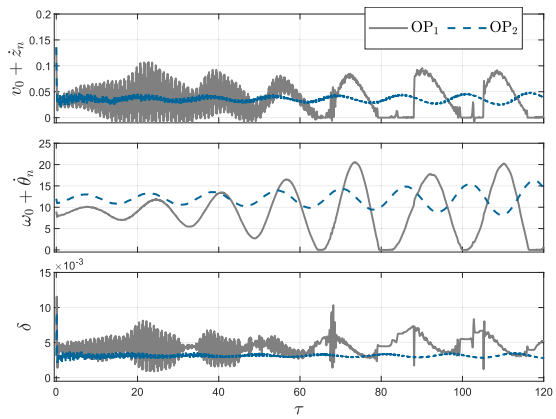

Fig. 9. Drilling with BHA and $n = 6$ for an 12 1/4″ well. Initial conditions are: $\dot{z}_n(0) = 0.1$ and $\boldsymbol{\theta}(t), z(t) = 0, \forall t \leq 0$.

6.1. System scaling and similarities to previous models

Systems exhibiting vibratory motion are commonly scaled to reduce the amount of variables and symbols of the system (See e.g., in Richard et al. (2007) for $n = 1$ with time-scale $t^\star = \sqrt{J/\kappa} = 1/\omega_n$ interpreted as the torsional resonance frequency, and Germay et al. (2009a) with $t^\star = 2\pi/\omega_1$, where ω_1 is the fundamental torsional frequency).

An additional scaling of the axial coordinates is commonly done (see e.g. (Besselink et al., 2011; Depouhon and Detournay, 2014; Germay et al., 2009a; Nandakumar and Wiercigroch, 2013; Richard et al., 2007),) with the length $L_\star = 2GI_z/(\varepsilon r_b^2 L)$. This length represents the total depth of cut with a perfectly sharp bit (i.e., l_w close to zero), subjected to a torque which induces a twist of one radian in the drill string. A normalization of the bit-rock forces and torques is then computed with $L_\star$.

The motivation for utilizing the different scales is to clearly distinguish the axial from the torsional dynamics, and to reduce the number of parameters. Discussed in previous work is also that the torsional stick-slip cycles are closely related to the torsional resonance frequency (Lai et al., 2016). Moreover, by post-multiplicating (24) and (26) with these scaling units, the system can be brought on a similar scale. The results shown in Section 5 are thus qualitatively similar as for the models in the previous papers.

6.2. Validity and use of findings

The parameter α in (24) defines the feedback of the delayed state into the axial system. This parameter is computed according to drill string configuration and the chosen rock properties. It is important to point out that the assumed values for the rock properties and bit configurations affects α, and the stability lines are by no means generalized.

The stability switches found in Section 4 and presented in Figs. 3 and 4 are based on assuming a possibility for decoupling the two systems. The effects of increasing n on stability margin are hence only valid for the stated assumptions.

The stability analysis conducted with (36) is dependent on the model order, and evaluation of the stability switches are dependent on the numerical computation of the polynomial coefficients for increasing n. Further analysis of the stability region dependence on n with (36) is a next step in providing additional proof to the conclusions made. Furthermore, experimental data isolating the axial and torsional measurements might be necessary to compare with the results given. Due to space limitation and availability of measurement data, these topics are left for future work.

The findings in regards to axial stability for the lumped-multi-element model are considered important in model selection due to knowledge of system limitations. Hence, more robust implementations of drilling optimization systems with the lumped parameter models can be achieved.

6.3. Real-time applicability

Even though nondimensionalization of the model helps speed up computer simulation, the general limitation of making the model suitable for real-time purposes is the solution procedure for obtaining the time-delay. At each time-step this must be done numerically and might, in worst case for the simulations done in this work, take seconds.

A Taylor expansion around $\tau_n = 0$ of the delayed bit angular displacement $\theta_n(\tau - \tau_n)$ can be found as

$$\theta_n(\tau - \tau_n) \approx \theta_n(\tau) - \tau_n \dot{\theta}_n(\tau) + \frac{1}{2^{\tau_n}} \ddot{\theta}_n(\tau) + \text{H.O.T.} \tag{45}$$

where H.O.T. denotes the higher order terms in the series expansion. This can then be used to solve for τ_n in (11).

By using (45), we can bring the model into real-time characteristics, if the time-delay is sufficiently small. However, the torsional stick-slip cycles can delay the bit rotation substantially. As pointed out in Insperger et al. (2005), a Taylor expansion of $\theta_n(\tau - \tau_n)$ included in the system when the delay becomes large, cannot be compared to the true stability characteristics of (24) and consequently (26). Moreover, the stability requirements derived in Section 3 are no longer valid if the model is implemented with (45).

7. Conclusions

We have presented a generalization of the drill string models introduced in previous works with a lumped-multi-element model. The axial and torsional dynamics are coupled through a bit-rock interaction law considering drag bits, and the system is defined as an state-dependent delay differential equation. The analysis presented in this work are in terms of nominal drilling velocities. Furthermore, the model can be efficient in terms of further development of control system strategies to mitigate vibrations. Hence, parameters such as optimal hook load and top-side rotation can be analysed.

A stability analysis is performed for the decoupled axial dynamics for six realistic drill string configurations. For a uniform drill string assembly, one distinct delay margin was found to be associated with a crossing frequency with magnitude multiple times larger than the configuration's largest eigenfrequency. Both in the case of a uniform drill string, and including a BHA, a high rpm setting is required to ensure stability of the drilling process, specifically for the shorter wells. This is consistent with the results in Dareing et al. (1990), where instability was related to larger bit diameter size combined with low rotational speed, and few drag bit blades.

Increasing the number of model elements is seen to increase the critical rpm margin and reduce the stable regions for the system. Moreover, this indicate that for n arbitrarily large, the stability regions moves towards zero and the decoupled axial system might always be unstable. From this analysis, it is seen to be necessary to include the nonlinear effect of the coupled dynamics addressing both v_0 and ω_0, when performing stability analysis of a lumped-multi-element axial and torsional drill string system.

The coupled dynamics is analysed through simulation studies for two and six elements, for the 36″ and 12 ¼″ configuration. High stiffness governs the shorter wells, and as such requires higher rotational speeds to avoid drill string formation stick. Increasing the length of the well being drilled with a small number of model elements lowers the overall stiffness of the drill string. This might underestimate the physical stiffness of the drill string due to too low stiffness factor. By including a BHA, the torsional stick cycles becomes more periodic and the time-period of stick can evolve in several torsional waves travelling back and forth in the drill string.

Credit author statement

Njål Kjærnes Tengesdal: Conceptualization, Methodology, Software, Investigation, Visualization, Writing-Original Draft, Writing-Review & Editing. **Sigve Hovda**: Supervision, Conceptualization, Methodology, Writing-Original Draft, Writing - Review & Editing. **Christian Holden**: Supervision, Writing-Original Draft, Writing - Review & Editing.

Declaration of competing interest

The authors declare that they have no known competing financial interests or personal relationships that could have appeared to influence the work reported in this paper.

Acknowledgements

The research presented in this paper has received funding from the

Norwegian Research Council, SFI Offshore Mechatronics, project number 237896.

Appendix A. Supplementary data

Supplementary data to this article can be found online at https://doi.org/10.1016/j.petrol.2020.108070.

References

Aadnoy, B.S., Larsen, K., Berg, P.C., 2003. Analysis of stuck pipe in deviated boreholes. J. Petrol. Sci. Eng. 37, 195–212. https://doi.org/10.1016/S0920-4105(02)00353-4.

Aarsnes, U.J.F., van de Wouw, N., 2018. Dynamics of a distributed drill string system : characteristic parameters and stability maps. J. Sound Vib. 417, 376–412. https://doi.org/10.1016/j.jsv.2017.12.002.

Agarwal, R.P., Berezansky, L., Braverman, E., Domoshnitsky, A., 2014. Nonoscillation Theory of Functional Differential Equations with Applications, vol. 9781461434559. Springer, New York. https://doi.org/10.1007/978-1-4614-3455-9.

Bakhtiari-Nejad, F., Hosseinzadeh, A., 2017. Nonlinear dynamic stability analysis of the coupled axial-torsional motion of the rotary drilling considering the effect of axial rigid-body dynamics. Int. J. Non Lin. Mech. 88, 85–96. https://doi.org/10.1016/j.ijnonlinmec.2016.10.011.

Besselink, B., van de Wouw, N., Nijmeijer, H., 2011. A semi-analytical study of stick-slip oscillations in drilling systems. J. Comput. Nonlinear Dynam. 6, 021006 https://doi.org/10.1115/1.4002386.

Besselink, B., Vromen, T., Kremers, N., van de Wouw, N., 2016. Analysis and control of stick-slip oscillations in drilling systems. IEEE Trans. Contr. Syst. Technol. 24, 1582–1593. https://doi.org/10.1109/TCST.2015.2502898.

Canudas-de Wit, C., Rubio, F.R., Corchero, M.A., 2008. D-OSKIL: a new mechanism for controlling stick-slip oscillations in oil well drillstrings. IEEE Trans. Contr. Syst. Technol. 16, 1177–1191. https://doi.org/10.1109/TCST.2008.917873.

Cayeux, E., 2018. On the importance of boundary conditions for real-time transient drillstring mechanical estimations. In: IADC/SPE Drilling Conference and Exhibition. https://doi.org/10.2118/189642-MS.

Christoforou, A.P., Yigit, A.S., 2003. Fully coupled vibrations of actively controlled drillstrings. J. Sound Vib. 267, 1029–1045. https://doi.org/10.1016/S0022-460X(03)00359-6.

Dareing, D., Tlusty, J., Zamudio, C., 1990. Self-excited vibrations induced by drag bits. J. Energy Resour. Technol. Trans. ASME 112, 54–61. https://doi.org/10.1115/1.2905713.

Depouhon, A., Detournay, E., 2014. Instability regimes and self-excited vibrations in deep drilling systems. J. Sound Vib. 333, 2019–2039. https://doi.org/10.1016/j.jsv.2013.10.005.

Detournay, E., Defourny, P., 1992. A phenomenological model for the drilling action of drag bits. Int. J. Rock Mech. Min. Sci. GeoMech. 29, 13–23. https://doi.org/10.1016/0148-9062(92)91041-3.

Detournay, E., Richard, T., Shepherd, M., 2008. Drilling response of drag bits: theory and experiment. Int. J. Rock Mech. Min. Sci. 45, 1347–1360. https://doi.org/10.1016/j.ijrmms.2008.01.010.

Faassen, R.P., van de Wouw, N., Oosterling, J.A., Nijmeijer, H., 2003. Prediction of regenerative chatter by modelling and analysis of high-speed milling. Int. J. Mach. Tool Manufact. 43, 1437–1446. https://doi.org/10.1016/S0890-6955(03)00171-8.

Florence, F., Iversen, F., 2010. Real-time models for drilling process automation: equations and applications. In: SPE/IADC Drilling Conference, Proceedings, vol. 2, pp. 1218–1233. https://doi.org/10.2118/128958-ms.

Germay, C., van de Wouw, N., Sepulchre, R., Nijmeijer, H., 2005. Axial Stick-Slip Limit Cycling in Drill-String Dynamics with Delay. ENOC-2005.

Germay, C., Denoël, V., Detournay, E., 2009a. Multiple mode analysis of the self-excited vibrations of rotary drilling systems. J. Sound Vib. 325, 362–381. https://doi.org/10.1016/j.jsv.2009.03.017.

Germay, C., van de Wouw, N., Nijmeijer, H., Sepulchre, R., 2009b. Nonlinear drillstring dynamics analysis. SIAM J. Appl. Dyn. Syst. 8, 527–553. https://doi.org/10.1137/060675848.

Ghasemloonia, A., Geoff Rideout, D., Butt, S.D., 2015. A review of drillstring vibration modeling and suppression methods. J. Petrol. Sci. Eng. 131, 150–164. https://doi.org/10.1016/j.petrol.2015.04.030.

Golub, H.G., Loan, V.F.C., 2013. Matrix Computations, fourth ed. The Johns Hopkins University Press.

Gu, K., Kharitonov, L.V., Chen, J., 2003. Stability of Time-Delay Systems. Springer Science & Business Media.

Gupta, S.K., Wahi, P., 2016. Global axial-torsional dynamics during rotary drilling. J. Sound Vib. 375, 332–352. https://doi.org/10.1016/j.jsv.2016.04.021.

Hovda, S., 2016. Closed-form expression for the inverse of a class of tridiagonal matrices. Numer. Algebra Contr. Optim. 6, 437.

Hovda, S., 2018a. Automatic detection of abnormal torque while reaming. J. Petrol. Sci. Eng. 166, 13–24. https://doi.org/10.1016/j.petrol.2018.02.050.

Hovda, S., 2018b. Semi-analytical model of the axial movements of an oil-well drillstring in vertical wellbores. J. Sound Vib. 433, 287–298. https://doi.org/10.1016/j.jsv.2018.07.016.

Insperger, T., Stépán, G., Turi, J., 2005. State-dependent delay model for regenerative cutting processes. In: Fifth EUROMECH Nonlinear Dynamics Conference, pp. 1124–1129. https://www.tib.eu/de/suchen/id/BLCP.

Jogi, P.N., Macpherson, J.D., Neubert, M., 2002. Field verification of model-derived natural frequencies of a drill string. J. Energy Resour. Technol. 124, 154. https://doi.org/10.1115/1.1486018.

Lai, S.W., Bloom, M.R., Wood, M.J., Eddy, A., Holt, T.L., 2016. Stick/Slip detection and friction-factor testing with surface-based torque and tension measurements. SPE Drill. Complet. 31, 119–133. https://doi.org/10.2118/170624-PA.

Nandakumar, K., Wiercigroch, M., 2013. Stability analysis of a state dependent delayed, coupled two DOF model of drill-stringvibration. J. Sound Vib. 332, 2575–2592. https://doi.org/10.1016/j.jsv.2012.12.020.

Navarro-Lopez, E., Suarez, R., 2004. Practical approach to modelling and controlling stick-slip oscillations in oilwell drillstrings. In: Proceedings of the 2004 IEEE International Conference on Control Applications, vol. 2004, pp. 1454–1460. https://doi.org/10.1109/CCA.2004.1387580, 2.

Rao, S.S., 2007. Vibration of Continuous Systems. John Wiley & Sons. https://doi.org/10.1002/9780470117866.

Richard, J.P., 2003. Time-delay systems: an overview of some recent advances and open problems. Automatica 39, 1667–1694. https://doi.org/10.1016/S0005-1098(03)00167-5.

Richard, T., Germay, C., Detournay, E., 2004. Self-excited stick-slip oscillations of drill bits. Compt. Rendus Mec. 332, 619–626. https://doi.org/10.1016/j.crme.2004.01.016.

Richard, T., Germay, C., Detournay, E., 2007. A simplified model to explore the root cause of stick-slip vibrations in drilling systems with drag bits. J. Sound Vib. 305, 432–456. https://doi.org/10.1016/j.jsv.2007.04.015.

Saldivar, B., Mondié, S., Niculescu, S.I., Mounier, H., Boussaada, I., 2016. A control oriented guided tour in oilwell drilling vibration modeling. Annu. Rev. Contr. 42, 100–113. https://doi.org/10.1016/j.arcontrol.2016.09.002.

Sipahi, R., 2019. Mastering Frequency Domain Techniques for the Stability Analysis of LTI Time Delay Systems. SIAM.

Walton, K., Marshall, J.E., 1987. Direct method for tds stability analysis. IEE Proc. D: Control Theory & Appl. 134, 101–107. https://doi.org/10.1049/ip-d.1987.0018.

Wang, Z.H., Hu, H.Y., 2000. Stability switches of time-delayed dynamic systems with unknown parameters. J. Sound Vib. 233, 215–233. https://doi.org/10.1006/jsvi.1999.2817.

ISBN 978-82-326-6900-4 (printed ver.)
ISBN 978-82-326-5593-9 (electronic ver.)
ISSN 1503-8181 (printed ver.)
ISSN 2703-8084 (online ver.)

NTNU
Norwegian University of
Science and Technology